1-1-2017

Commissioning And Validation Of Analytical And Monte Carlo Based Dose Calculation Algorithms For Proton Spot Scanning

Jatinder Saini
Wayne State University,

COMMISSIONING AND VALIDATION OF ANALYTICAL AND MONTE CARLO BASED DOSE CALCULATION ALGORITHMS FOR PROTON SPOT SCANNING

by

JATINDER SAINI

DISSERTATION

Submitted to the Graduate School

of Wayne State University,

Detroit, Michigan

in partial fulfillment of the requirements

for the degree of

DOCTOR OF PHILOSOPHY

2017

MAJOR: MEDICAL PHYSICS

Approved By:

_____

Advisor Date

_____

_____

_____

_____

ACKNOWLEDGMENTS

I am very grateful to my advisor, Dr Charles, Bloch, for taking time of his busy schedule to guide me through PhD. Dr Bloch has always provided answers to my numerous questions related to proton therapy and radiation therapy in general. Since Dr. Bloch's office is next o mine, the only thing I need to do whenever I need expert advice, is to get up and start asking questions. I felt very fortunate to have such a resource.

I would also like to thank my co-advisor Dr Jay Burmeister for his help in last 8-10 years in facilitating my medical physics career. I started at Wayne State in 2008 for my master's degree in Medical Physics and proceeded to work towards PhD in ensuing years. It is due to my association with Wayne State that I was able to get a residency, attain board certification, and now attain PhD. This would not have been possible without Dr. Burmeister's help and I am very thankful for that.

I also would like to acknowledge contributions of my committee member, Dr. Tony Wong, towards my proton career journey. I had the pleasure of working with Dr. Wong as an intern after my master's degree and that relationship eventually led me to work for him as a physicist in my current job. Dr. Wong has always encouraged and supported me to work towards my PhD degree.

Finally, I would like to thank my committee members, Dr. Michael Joiner and Dr. Michael Snyder, for providing their insight, critique and comments for my research.

DEDICATION

This dissertation is dedicated to my wife, Sonika, for her love, encouragement and her unwavering support to further my career.

I also dedicate this work to our loving girls, Anisha and Sareen, who bring so much happiness to our life every day.

I also dedicate this work to my parents who have spent most of their life through difficult times in India and still managed to provide me with education.

I also dedicate this work to my aunt, Kulwant Kaur, who supported me throughout my life.

TABLE OF CONTENTS

LIST OF TABLES

LIST OF FIGURES

LIST OF ABBREVIATIONS

PBS ..... Pencil Beam Scanning

MC ..... Monte Carlo

TPS ..... Treatment Planning System

PBA ..... Pencil Beam Analytical

RS-MC ..... RayStation Monte Carlo

RS-PBA ..... RayStation Pencil Beam Analytical

GATE ..... GEANT4 Application for Tomographic Emission

PS ..... Passive Scattering

AP/PA ..... Anterior-Posterior/Posterior-Anterior

MeV ..... Mega electron volt

SOBP ..... Spread out Bragg peak

RM ..... Range Modulator

US ..... Uniform Scanning

OAR ..... Organ at risk

IMRT ..... Intensity Modulated Radiation Therapy

MCS ..... Multiple Coulomb Scattering

BP ..... Bragg Peak

AAPM ..... American Association of Physicists in Medicine

RS ..... RayStation

IDDC ..... Integrated Depth Dose Curve

SAD ..... Source to Axis Distance

MLIC ..... Multi Layer Ionization Chamber

PDD.....Percent Depth Dose

RT .....Radiation Therapy

2-D ..... Two dimensional

3-D .....Three dimensional

TCP .....Tumor Control Probability

CTV ..... Clinical Target Volume

EM..... Electro-Magnetic

IDD ..... Integrated Depth Dose

G-MC.....GATE Monte Carlo

WET .....Water Equivalent Thickness

QA..... Quality Assurance

CT .....Computed Tomographic

IGRT..... Image Guided Radiation Therapy

kV ..... kilo-voltage

OS .....Operating System

MU.....Monitor Unit

TG ..... Task Group

TRS-398.....Technical Report Series #398

IAEA..... International Atomic Energy Agency

FWHM.....Full width half maximum

MFO .....Multi Field Optimization

RBE.....Relative Biological Effectiveness

AR ..... Alderson-Rando

DT ..... Dose Tolerance

DTA ..... Distance to Agreement

ICRU ..... International Council of Radiation Units

H&N ..... Head and Neck

CSI ..... Cranio-Spinal Irradiation

CHAPTER 1 BASICS OF PROTON THERAPY

1.1. Introduction

The use of proton for radiation therapy was first proposed by Dr. Robert Wilson in his work in 1946 (1), when he postulated that the Bragg peak formed by hadrons could be used to deposit maximum energy inside the tumor. The first treatments with proton therapy were performed at Berkeley Lab in 1954 (2) using the 184 inch cyclotron as a source of protons to treat pituitary gland tumors. Proton therapy was also used to treat pituitary gland treatments in 1957 at Uppsala, Sweden (3) and in 1961 at Harvard Cyclotron Laboratory (4). Proton therapy was limited to major research labs until 1990, when the first hospital based facility was opened at Loma Linda University (5) after two decades of development and collaboration with Fermi National Accelerator Laboratory. From thereon, the number of hospital based centers increased at a slow pace with only four centers in the U.S. treating with protons by the end of 2006. However, in the last decade, proton therapy has seen a tremendous growth in the U.S. and internationally. Proton therapy is becoming increasingly available in the U.S. with close to 25 centers treating patients (6). Worldwide, there are close to 70 centers that are treating patients with protons with another 50-70 facilities in some stage of construction or planning (7). While the availability of proton therapy is increasing, so are the clinical trials that compare the efficacy of proton therapy with conventional radiation. With increasing adoption of proton therapy, the number of patients that are treated with proton therapy is increasing rapidly and thereby providing more data for comparison of clinical outcomes. The superior dose distributions afforded by proton therapy make it an ideal

form of treatment for pediatric patients, re-treatment cases, and complicated targets where conventional radiation therapy may not yield optimum plans.

1.2. Rationale for Proton Therapy

The main goal of radiation therapy is to deposit the dose in cancer cells while minimizing radiation to the normal tissue cells. This is generally achieved by various means i.e. (i) using multiple beam angles (ii) selecting the appropriate beam angles to minimize, normal tissue exposure, (iii) use of intensity modulation, where beams are modulated to conform isodoses to the target volume, and (iv) exploiting the depth dose characteristics of the type of radiation. The main advantage of proton therapy over conventional electron and photon therapies is the characteristics of its depth dose distribution (Figure 1). According to Bethe-Bloch equation (8), the linear stopping power of a charged particle traversing in matter is due to collisional and radiative processes and is given by:

$$S = -\frac{dE}{dx} = \frac{4\pi e^4 z^2 NZ}{(4\pi\varepsilon_0)^2 M_e v^2}\left[\ln\left(\frac{2M_e v^2}{I}\right) - \ln(1-\beta^2) - \beta^2\right] \quad \text{.....Eqn. 1}$$

with the following definitions: v= velocity of the charged particle, ze= charge of the charged particle, Z= atomic number of absorber material, N= number density of absorber atoms, M_e=electron rest mass, e= electron charge, I= average excitation and ionization potential, β=v/c, c=velocity of light. At low charged particle energies, β<<1, the above equation reduces to:

$$S = -\frac{dE}{dx} = \frac{4\pi e^4 z^2 NZ}{(4\pi\varepsilon_0)^2 M_e v^2}\left[\ln\left(\frac{2M_e v^2}{I}\right)\right] \quad \text{.....Eqn. 2}$$

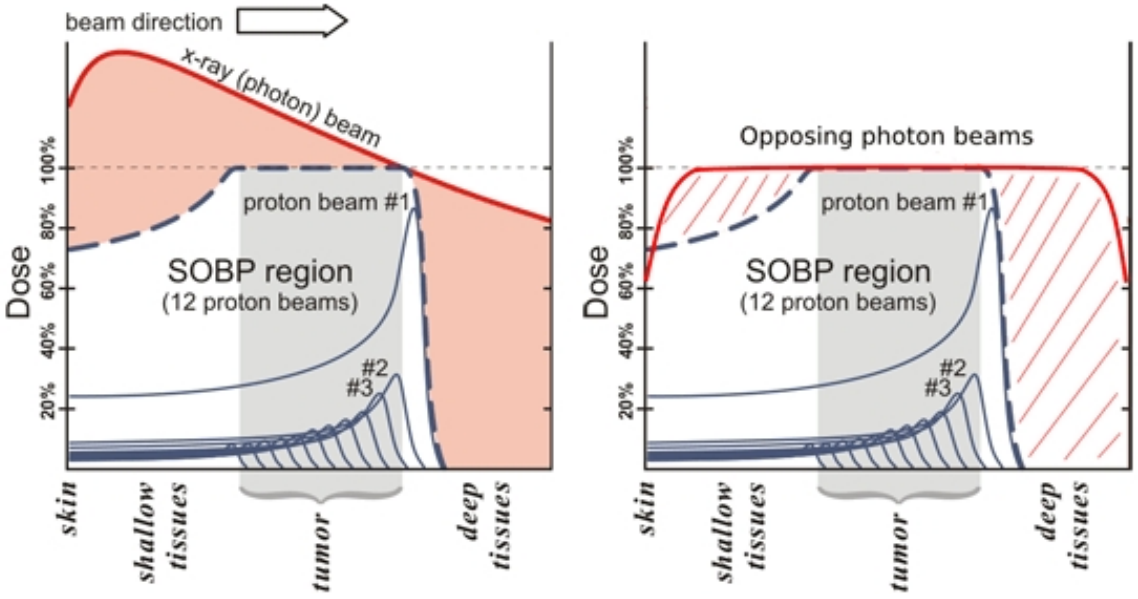

Figure 1. (Left) Comparison of depth dose characteristics between a proton SOBP beam and an X-ray beam. The SOBP beam is composed of 12 elemental Bragg peaks with variable weights to create a SOBP (Right) Even when AP/PA configuration of beams is used; there is advantage of using proton beam due to reduced entrance dose and no dose to deep tissue. Figure obtained from www.radiotherapie.nl.

Figure 2 shows the stopping power of a 200 MeV proton beam in water. It can be seen that due to the $1/v^2$ dependence, the stopping power increases sharply when the residual energy of the beam is below 30 MeV. It is this phenomenon that gives rise to the Bragg peak (figure 1). This is a major advantage over conventional radiotherapy using photons. The photon depth dose, when entering a medium, has an initial build up before reaching maximum and then decreases exponentially. Since most tumors treated with radiotherapy are located deeper than the depth of maximum dose, this effectively means that a photon beam will deposit more dose in the normal tissue upstream of the tumor. With proton therapy, one could position the location of Bragg

peak inside the target thereby reducing the dose to the overlying tissue. Another advantage of the proton beam is its ability to completely stop in the tissue and thus give no dose to any tissue beyond the target. A photon beam, due to its exponential decline, will keep on depositing substantial dose to underlying tissue. Even when using an AP/PA beam arrangement for photons, there is a substantial reduction in integral dose for shallow and deep tissue using the proton therapy (figure 1).

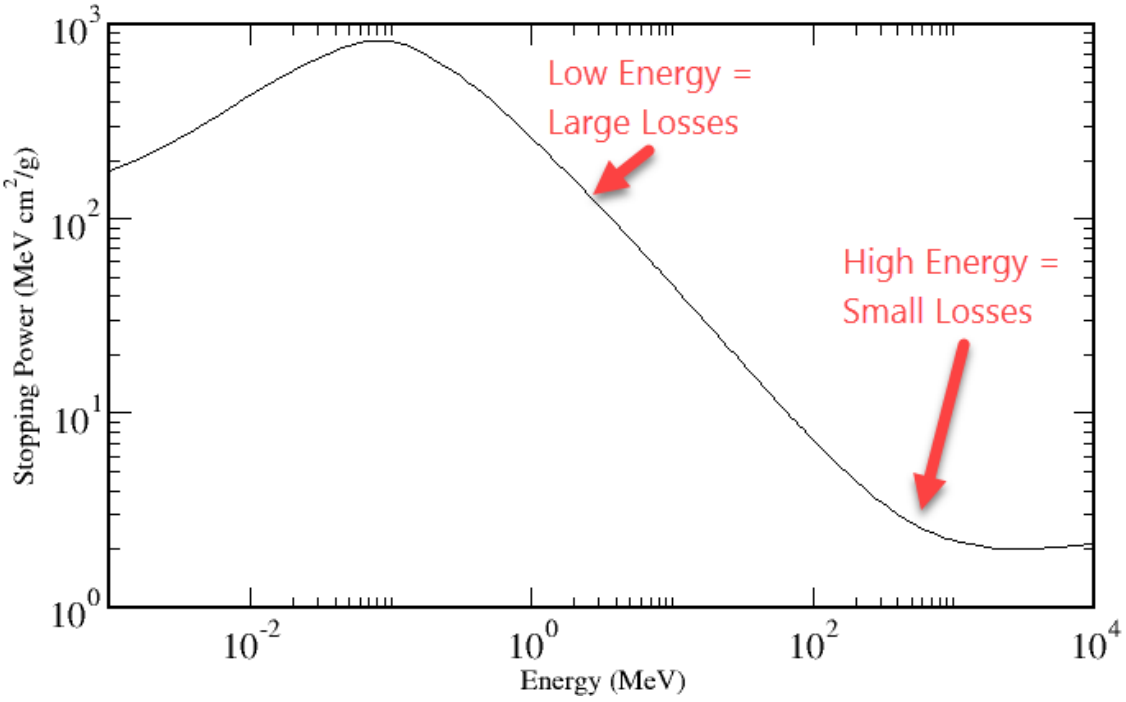

Figure 2. Stopping power of 200 MeV proton beam in water. Plot obtained from physics.nist.gov

1.3. Types of proton therapy

The proton beam generated by the cyclotron is generally a very narrow beam and needs to be spread to cover the required field cross-section to be useful clinically. There are two commonly used techniques to achieve this: (i) Passive Scattering, and (ii) Active Scanning.

1.3.1. Passive Scattering Systems

In order for a narrow beam to be useful for clinical treatments, it has to be spread in the lateral as well as depth directions. For cyclotrons, the spreading in the depth direction is typically accomplished by a range modulator (RM) (9) (figure 3). The RM wheel has many tracks and steps of variable thickness corresponding to the range of energies desired for clinical use. The incident energy of a proton beam is reduced relative to the thickness of the material in the beam path. In order to generate a Spread Out Bragg Peak (SOBP) from a pristine peak, the RM wheel can be programmed to introduce varying thicknesses of material in the beam path as a function of time. As each step is a different thickness, a spectrum of output ranges can be obtained. By passing the pristine beam from each step for a set amount of time, the intensity of the output peak can be controlled. By adding many modulated peaks of different energy and intensity, an SOBP is obtained (figure 3).

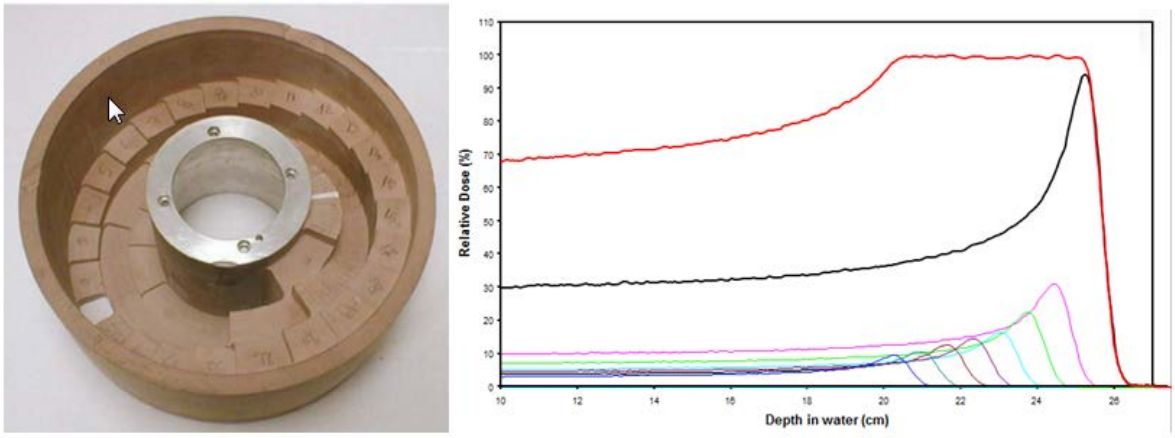

Figure 3. (Left) An example of modulator wheel used by IBA (Louvain La Neuve, Belgium) system. Image obtained from Kooy et al (10). (right) Demonstration of how elemental Bragg peaks are added to form a spread out Bragg peak (SOBP) beam.

The broadening of narrow beam in the lateral direction is performed through a dual foil scatter system (11). The first scatterer is a uniform thickness material in the beam path that is generally made of high Z material. The output beam profile after the first scatterer is approximately a forward peaked Gaussian shape that must be further flattened for clinical usability. A second scatterer that has a non-uniform thickness or atomic composition is used to produce a flat or nearly flat distribution at the patient plane.

Once a beam is spread laterally and in the depth direction, a rectangular uniform dose distribution in a water phantom can be obtained. However, further modifications are required to the beam profile to fully exploit the potential of proton therapy. By adding beam modifying hardware such as apertures and range compensators (12), a flat beam profile can be conformed to patient specific target. An aperture (figure 4) is a piece of hardware that shapes the lateral extent of proton beam to the target outline in beam's eye view. Generally, apertures are made up of brass of sufficient thickness to completely stop the unwanted protons that are outside the projection of the treatment volume. The shape of the aperture is determined during the treatment planning process and the design is typically transferred to a CNC machine for milling. Use of apertures allows lateral conformality of the proton beam to the target. The conformality on the distal side of the target is achieved through the use of a range compensator (figure 4). A range compensator is generally made up of acrylic or wax and has spatially varying thickness that is dictated by the geometry of the target volume. A range compensator is able to account for spatial changes in the patient surface, inhomogeneities, and distal tumor shape. Both compensator and aperture are beam specific devices that are

custom built for each patient field. The full schematic of passive scattering system is shown in figure 5.

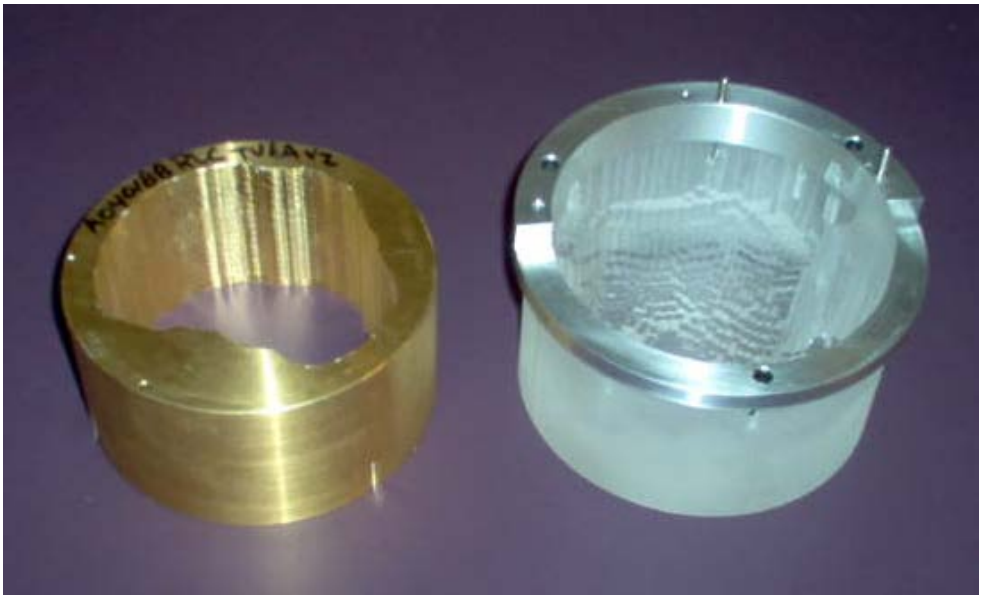

Figure 4. Patient specific hardware for passive scattering and uniform scanning: aperture (left) and compensator (right). Apertures are used to conform the isodoses laterally to the target volume. Compensators provide conformality of isodoses at the distal side of the target.

As seen, a passive scattering system is able to conform isodoses to the desired target in both the lateral and distal directions. However, as the modulation of the beam is fixed, the beam cannot be conformed to the target in the proximal direction. This can be seen in figure 5, where there is increased dose at the proximal side of the target. In addition, passive scattering systems require patient specific hardware that leads to higher cost and increased lead up times. Furthermore, beam modifiers produce additional neutron background that has potential to increase the risk of secondary cancers.

1.3.2. Active Scanning Systems

There are currently two main technologies that are used by active scanning systems: uniform scanning (US) and pencil beam scanning (PBS). For the US systems (figure 6), a constant intensity proton beam is scanned across the field area defined by the snout resulting in a flat uniform profile. For the IBA systems, the beam is scanned at 30Hz in vertical direction and 3Hz in horizontal direction. The advantage of US over passive scattering is that protons are able to maintain their energy as they do not have to travel through as much scattering material. In addition, there is reduction of unwanted scattered radiation due to removal of scatterers. However, the US systems still require the use of patient specific apertures and compensators for conforming isodoses to the target. The US systems produce a square or a circular uniform field that needs to be collimated to the lateral extent of the target. Similarly, the conformality in the distal side of the target is achieved by placing a variable thickness compensator. Both aperture and compensator are mounted on the snout close to the patient surface to reduce geometrical penumbra due to aperture.

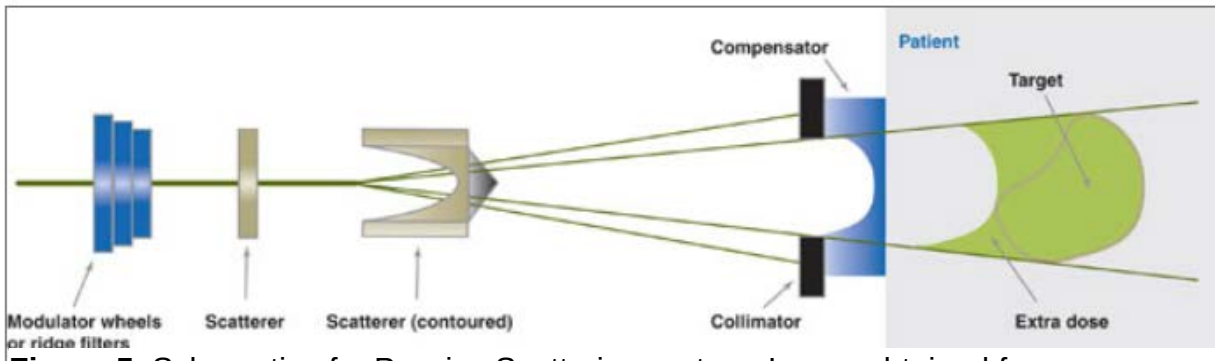

Figure 5. Schematic of a Passive Scattering system. Image obtained from medicalphysicsweb.com

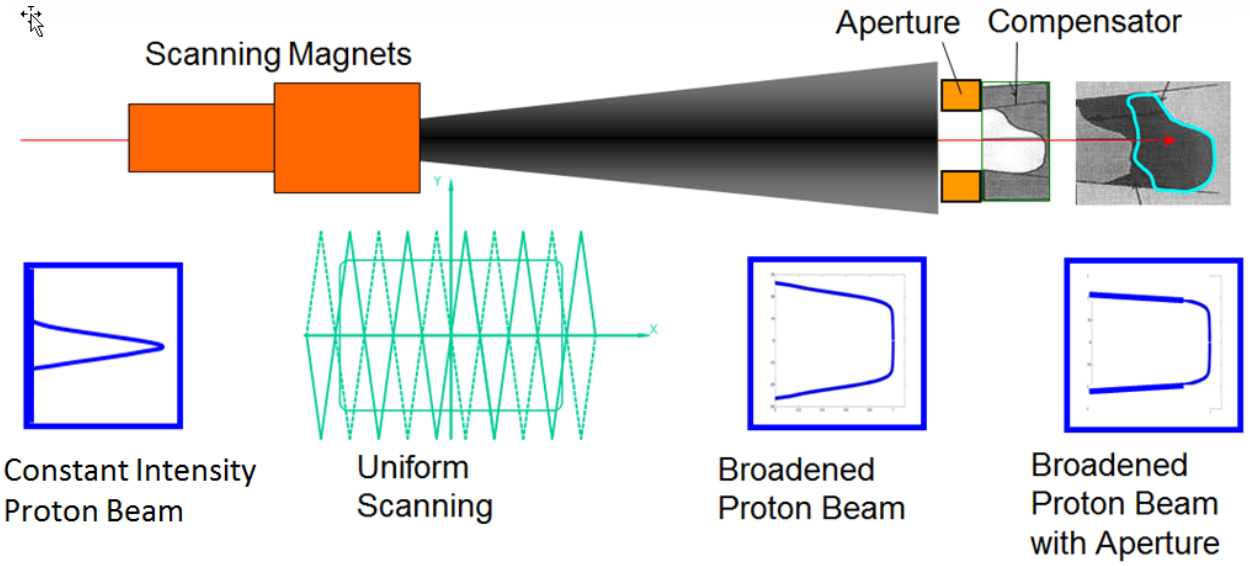

Figure 5. Schematic of an IBA uniform scanning system. A constant intensity proton beam is scanned across the field in both horizontal and vertical direction to produce a flat dose profile. By placing an aperture and a compensator at the end of the snout, the field can be conformed to a target.

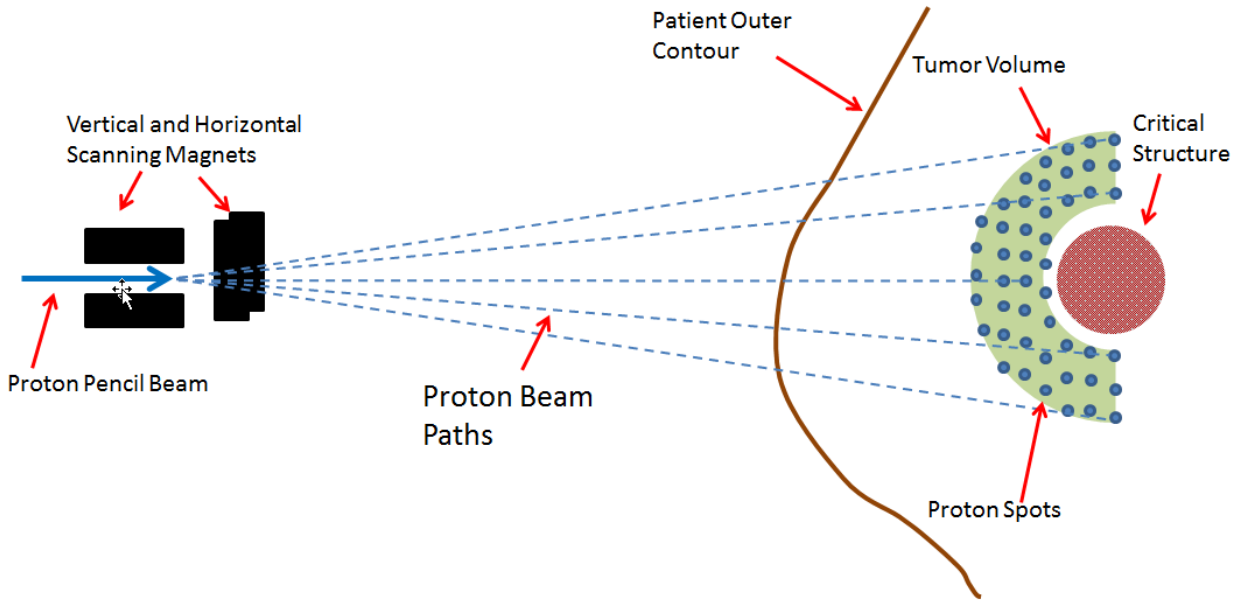

Figure 6. Schematic of a proton pencil beam scanning system. Dose is deposited using individual spots that can be conformed to the target volume.

A pencil beam scanning system (figure 7) enables dose conformality in the proximal, distal and lateral directions without the need for any beam specific hardware. The dose is deposited in the form of many narrow individual pencil beams (spots) of varying energy and intensity. The lateral position of the spots is controlled by varying the current on scanning magnets in the X and Y directions. The longitudinal position of the spot (Bragg peak) is controlling by varying the energy of the proton beam. A 3-D target is divided into many layers and dose is deposited sequentially from distal to proximal layer. Within each layer, dose is deposited by spots, whose location and intensity is determined by the planning system. By positioning the spots to the outline of the target volume, the dose distribution can be conformed to the target in all directions. Pencil beam scanning systems provide numerous advantages over US and PS systems such as, (i) no need for field specific hardware, (ii) low neutron background due to fewer beam modifiers, (iii) higher effective dose rate as scanning is limited to the extent of the target instead of the whole field when compared to uniform scanning. The main disadvantage of PBS over US or PS systems is sensitivity to motion in terms of interplay effect i.e. relative motion between the delivery of spots and moving target region and anatomy. Due to time dependent nature of PBS delivery, there is a possibility of a target moving out of the position within the delivery of layer. Mitigation strategies for the interplay effect have been developed such as repainting of layers or repainting of the entire treatment volume (13).

Another difference between passive scattering, uniform scanning and pencil beam system is from the treatment planning point of view. Both US and PS treatment planning is performed using forward planning methods. The target and OAR doses are

manipulated by iteratively varying one of the many treatment parameters such as range, modulation, aperture opening, and compensator thickness. In PBS, treatment planning is performed using inverse optimization similar to intensity modulated radiation therapy (IMRT). The treatment planner will provide the planning system with a set of instructions in the form of target and OAR dose-volume objectives and constraints, and the planning system will come out with a solution that best matches the specified criteria. For PBS plans, users are able to specify energy layer spacing and spot spacing for each beam before dose optimization.

1.4. Proton Interactions in Matter

Protons interact with matter in mainly three types of interactions, (i) coulomb interactions with orbital electrons, (ii) coulomb interactions with the nucleus, and (iii) nuclear interactions.

Due to the proton's large mass relative to the electron, most of them will travel in a straight line when they are in the vicinity of an orbital electron (figure 8a). In contrast, the columbic interaction with nucleus often results in deflection of proton from its straight line trajectory. In the entrance region, most of the proton interactions are coulombic and cause excitation or ionization of the orbital electrons. Since the mass of an electron is ~2000 times smaller than a proton, there is negligible deflection of a proton during this interaction. Although inelastic interactions occur in this region, the amount of energy transfer for each interaction is small and causes very slight deflection of the proton from its original path. As the proton traverses through the media, it keeps on losing small increments of energy to orbital electrons. The secondary electrons produced in the process have low energies and deposit most of their energy locally. As

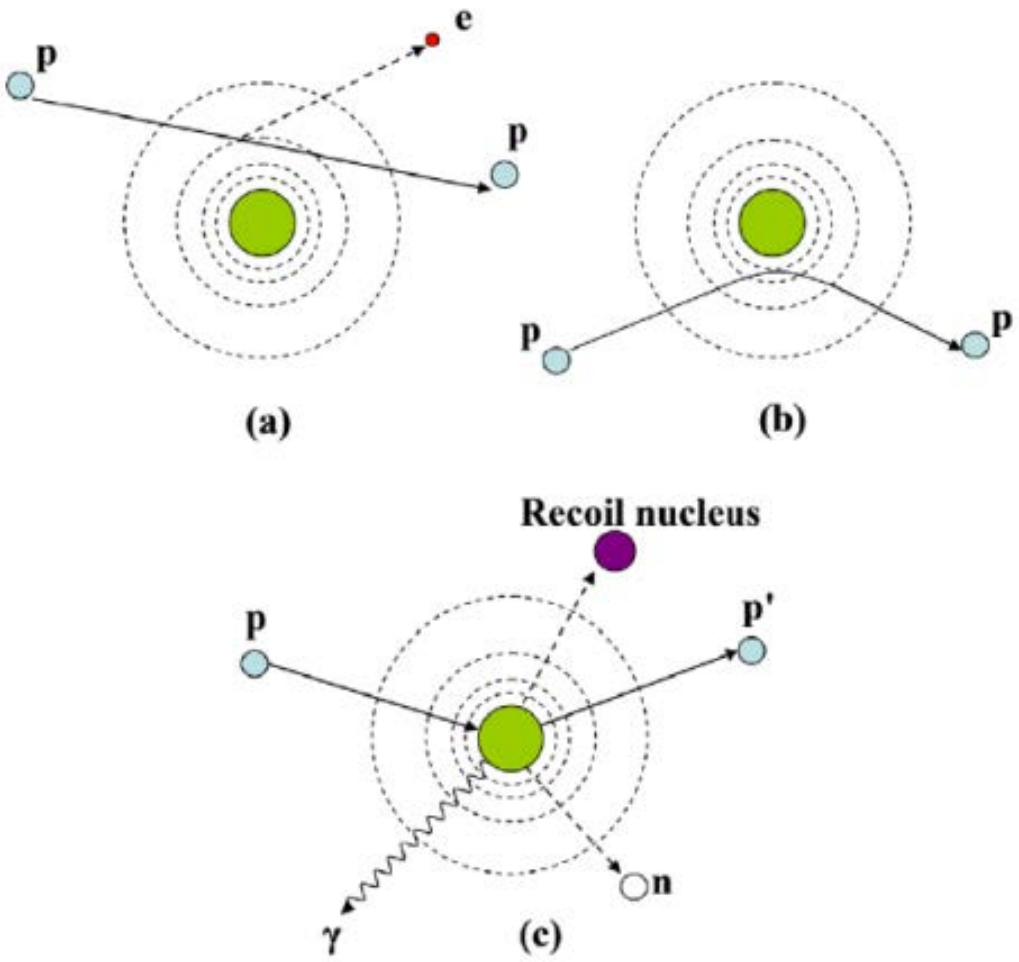

Figure 7. Proton interactions in matter. (a) Coulombic interaction of proton with an orbital electron causing ionization of the atom. (b) Coulombic interaction of proton with nucleus causing deflection of proton from its straight line trajectory. (c) Example of a nuclear interaction where proton collides with the nucleus and produces a recoil nucleus, gamma ray, a neutron, and a proton. Figure obtained from Newhauser et el (14).

the velocity of the original proton gradually decreases, it spends more and more time in the vicinity of the orbital electron thus gradually increasing the amount of energy transfer. The rate of energy loss i.e. linear stopping power formalism provided by Bethe and Bloch (equation 1) shows that energy loss is directly proportional to: (i) inverse square of proton's incident velocity, and (ii) density of electrons in the absorber material. Both of these dependencies have clinical significance for a proton beam

traversing through an absorber material. It is the inverse square dependence on the proton's velocity that gives rise to distinctive high dose peak area in the depth dose known as the "Bragg peak ". The dose in the Bragg peak is mainly due to low energy protons spending more time in the vicinity of orbital electrons and transferring maximum energy to them, which is deposited locally thus creating a sharp Bragg peak. The range of a proton beam inside a medium is dictated by the initial proton beam energy and the electron density of the absorber medium. Since the physical density of a material is closely related to electron density for human tissues, the range of protons in a material is mainly a function of density of the material. Clinically, this means that proton energy required to treat a tumor depends on the physical depth of the tumor as well as the density of the overlying tissue.

In terms of coulombic interactions with the atomic nucleus (figure 8b), the proton gets deflected from its straight line path due to the large mass of the nucleus. Although large deflections of the primary proton can occur, most of deflections are small. However, the cumulative impact of many such small events can lead to an increase in angular spread of the proton beam as its travels through an absorber medium. This gradual increase in angular distribution is called multiple coulomb scattering. Due to multiple coulomb scattering (MCS), the trajectory of a particle traversing a medium has multiple short straight line paths. A given proton will undergo a random number of interactions and will lose varying amounts of energy during each interaction. These statistical fluctuations in energy loss and number of interactions for each proton lead to a spread of proton energies at any particular depth. This phenomena is called range straggling and has an impact of increasing the width of Bragg peak. In addition, the

incident proton beam is not completely mono-energetic but also has an inherent energy spread that also contributes to widening of the Bragg peak. The most accepted theory to explain the characteristics of MCS as a function of particle type, energy and absorber material was given by Moliere (15). The angular distribution of protons that undergo MCS is approximately Gaussian. Moliere theory provides a formalism to calculate the width of the Gaussian distribution from the incident proton energy and target thickness. In terms of clinical significance, MCS determines the sharpness of the lateral penumbra. As the mass of the proton is relatively light compared to a nucleus, the amount of nuclear coulombic deflections from a straight line path is greater than for electron interactions thus increasing the lateral penumbra. In contrast, for particles like carbon, the deflection angle is smaller thus resulting in overall sharper lateral penumbra. Clinically, sharper penumbra is an advantage to reduce the normal tissue dose.

A very small fraction of incident protons will undergo direct head-on collision with the nucleus of an atom as shown in figure 8c. There are three types of nuclear interactions, (i) elastic, (ii) inelastic, and (iii) non-elastic. With elastic interactions, the kinetic energy of the incident proton is conserved and the proton scatters off the target nucleus. MCS, single or plural scattering are examples of elastic nuclear interactions. With non-elastic interactions, the kinetic energy is not conserved and secondary particles are generated that carry energy away from the interaction site. An incident proton bombards the target nucleus to cause break-up or elevation to an excited state. Inelastic interactions are a special case of non-elastic as part of the incident proton energy is used for excitation of the nucleus but the final nucleus is same as bombarded

nucleus. Generally, nuclear interactions are mostly referred to non-elastic interactions in literature. For non-elastic interactions, part of the incident proton energy is used to overcome the binding energy of the nucleus. The types of secondary particles that are possible are protons, neutrons, gammas and heavy nuclear fragments. There are two types of secondary particles that may be formed: short range charged particles and long range neutral particles. The secondary particles such as neutrons and gammas have relatively high range and thus end up depositing dose away from the local site. On the other hand, short range secondary particles such as alphas, protons and nuclear fragments will deposit most of their energy locally. The probability of a proton undergoing nuclear interaction increases with energy and is shown in figure 9 (16).

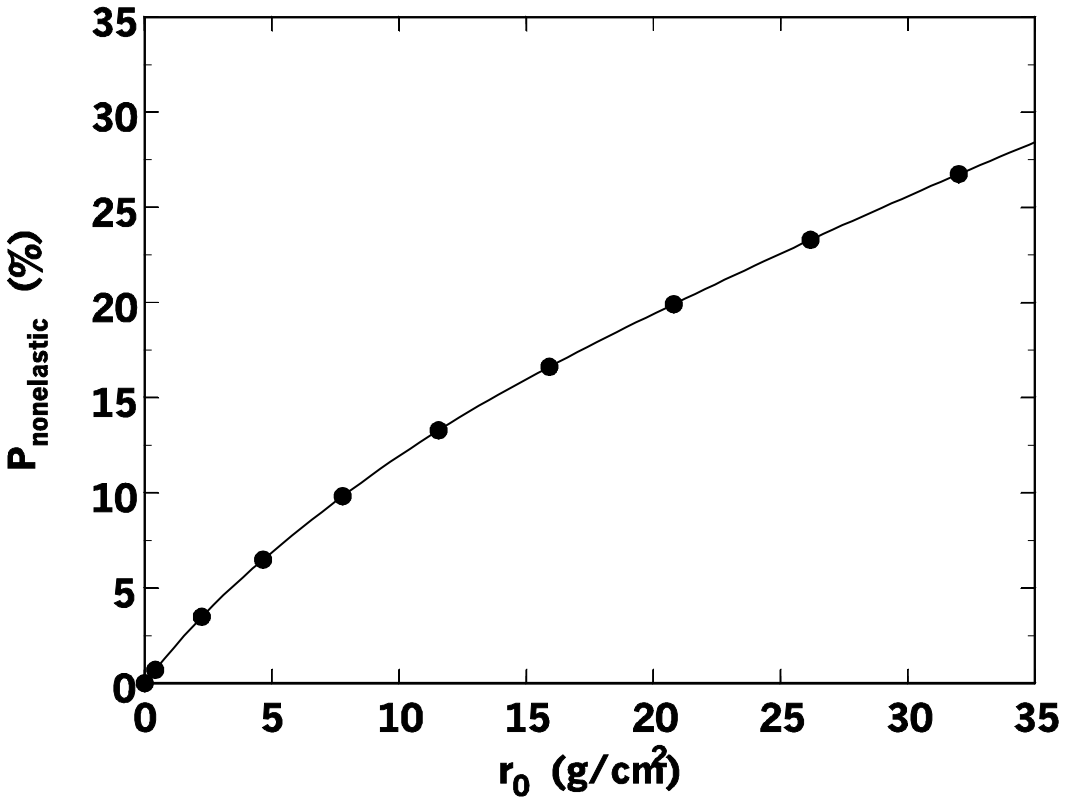

Figure 8. Nonelastic interaction probability as a function of proton range in water. Figure obtained from Gottschalk (16).

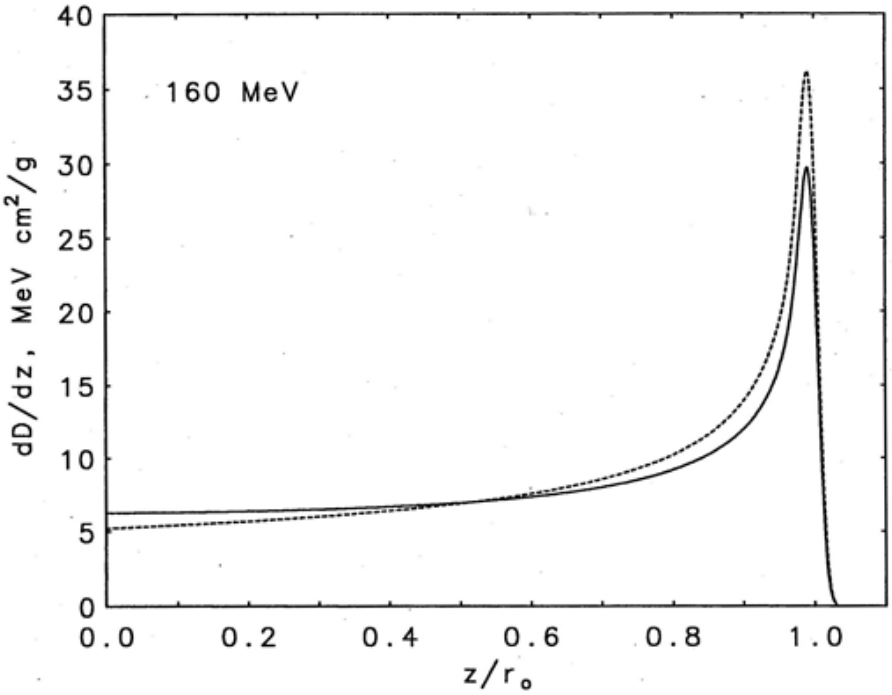

Figure 9. Depth dose for a 160 MeV proton beam with (solid line) and without (dashed line) nuclear interactions. The solid curve is an actual Bragg peak. The dashed line is simulated using MC with nuclear reactions switched off. Figure obtained from Berger et al (17).

In terms of clinical significance, nuclear interactions result in reduction of primary proton fluence thus changing the shape of Bragg peak (figure 10). The mean fluence reduction as given by Bortfeld (18) is 1.2% g^{-1} cm^2. The long range particles such as gammas and neutrons will remove dose from the Bragg peak and add dose to the surroundings. The short range particles have greater angular spread and carry lower energies that are deposited locally but result in a low dose region around the primary proton dose. This low dose region is referred to as nuclear halo in the literature (19, 20). It is critical to account for the nuclear halo in commissioning of proton spot scanning as excluding it could result in dose differences of up to 15% (19). Generally, the measurements of nuclear halo are difficult due to its low intensity and corrections are performed based on Monte-Carlo simulations.

1.5. Dose Calculation Algorithms

The following section is based on work by Clasie et al (21), Schaffner et al (22), Sokup et al (23), Newhauser et al (14) and Hong et al (24)

The currently available treatment planning systems for proton spot scanning can be divided into two classes, analytical and Monte-Carlo (MC) algorithms. Pencil beam algorithms are analytical in nature as the output dose distribution is the same for the same set of input parameters. On the other hand, MC dose calculation algorithms use random sampling of interaction cross-sections to simulate individual particles trajectories. The statistical nature of MC dose scoring can result in variation of output dose distribution based on the number of particle histories in the simulations. However, the statistical uncertainty decreases as the number of histories is increased.

1.5.1. Pencil Beam algorithms for Proton Spot Scanning

In the pencil beam analytical (PBA) algorithms, a wide proton beam is divided into many narrow mini-beams for dose calculation. In fact, these mini-beams are generally referred to as pencil beams with corresponding dose calculation algorithms called pencil beam algorithms. The PBA algorithms model the patient as a set of laterally infinite homogenous slabs whereas material encountered by the central axis of pencil beam is considered to be the material composition of the slab along the depth. This approach leads to PBA algorithms being insensitive to lateral inhomogeneities. The general formalism for calculating dose to water is the convolution of proton fluence ϕ with an elemental pencil beam dose distribution called dose kernel, k. k represents dose deposited in water by an infinitesimally narrow proton pencil beam. For a subset of pencil beams, the dose deposited at a point is given by:

$$D(x, y, z) = \sum_{\tilde{y}} \sum_{\tilde{x}} \Phi(x - \tilde{x}, y - \tilde{y}, z) K(\tilde{x}, \tilde{y}, \mathrm{wer}(\tilde{x}, \tilde{y}, z))$$

……..Eqn. 3

The convolution is replaced by a summation in the above equation to calculate dose on a discrete grid. The above formalism uses *wer* as water equivalent range at the central axis of the beam to account for inhomogeneities. The dose kernel, *k*, is terms of dose deposited at position *(x,y,z)* by a pencil beam along the z-axis and positioned at (x_0, y_0) is given by:

$$K(x, y, z) = N_{p^+}\mathrm{ID}(\mathrm{wer}) \frac{1}{2\pi\sigma_x\sigma_y} \exp[-(x_0 - x)^2/2\sigma_x^2] \exp[-(y_0 - y)^2/2\sigma_y^2]$$

…..Eqn. 4

ID= integral dose obtained from depth-dose look up table

wer= water equivalent range along the central axis of the beam.

σ_x, σ_y are standard deviation of spot intensity (spot sigmas) in x and y respectively

N_{p+} is the number of protons in the beam spot.

The integral depth dose (IDs) is obtained either by measurement or through MC simulations. The measurements are performed by using a wide area detector such as a Bragg peak (BP) chamber in a water tank. The beam is composed of a single spot that is incident at the central axis of the BP chamber. Such measurements are inherently difficult and time consuming due to need of high resolution in depth direction so as to capture the true shape of the Bragg peak. The alignment of the BP chamber is also critical to obtain correct ratio of Bragg peak to entrance region dose. For this reason, the measurements are sometimes fit to MC simulated IDs to obtain the energy spread for each available energy. Most of the dose kernels have some form of Gaussian function in the x and y directions to account for transport for proton spots through a

media. The Gaussian approximation is able to account for beam divergence and multiple coulomb scattering. However, there is a low dose envelope due to nuclear interactions called “nuclear halo” centered on a Gaussian profile. The corrections for nuclear halo are sometimes applied by adding a second Gaussian profile with a larger sigma or by modeling spots using non-Gaussian functions.

1.5.2. Monte Carlo (MC) Algorithms for Proton Spot Scanning

Dose calculation using MC algorithms generally starts at the exit plane of the nozzle where protons are tracked in the ensuing air gap, beam modifiers and lastly patient. The beam information at the nozzle exit is stored in a file, called “phase space”, which has information about the particle type, energy distribution, lateral profile, and divergence. For each beam energy, the phase space data can be generated from measurements or MC simulations of the nozzle and upstream components of the beam line. The same phase space data can be used for all patients as there is no change in the beam components on the source side of the beam. The MC simulation starts by randomly picking particles from the phase space distribution and transporting them through beam modifying devices, air gaps, and finally inside the patient. An individual particle will undergo physical interactions based on the interaction cross-sections in the medium of absorption. The interaction models for electromagnetic and nuclear interactions are based on theoretical models, parameterization, or experimental data. Energy transfer occurs when primary particles excite or dislodge orbital electrons or undergo nuclear interactions to produce neutrons, deuterons, tritons, alphas, electrons, and secondary protons. These secondary particles are tracked individually until they their energy falls below a certain threshold when all the energy is assumed to be

deposited locally. A very large number of particle histories have to be run, tracked, and doses scored to achieve required statistical uncertainty in the dose distribution.

MC methods are generally considered the gold standard for dose calculation due to their high accuracy. However, most MC methods are too slow for routine dose calculations. The statistical uncertainty for dose in a voxel using MC algorithm is inversely proportional to the square root of the number of particles simulated. Therefore, to improve the statistical uncertainty by a factor of two, one has to simulate four times as many particles. Most of the MC dose calculations for treatment plans have been performed using one of the research based codes. The clinical use of MC for dose calculation had been very limited due to the lack of commercial offering by any vendors until recently. With the advancement in computing resources, it should now be possible to routinely calculate doses using MC methods fast and efficiently. In fact, two vendors (RaySearch Inc., Garden City, NY, and Varian Medical Systems, Palo Alto, CA) have recently offered commercial MC dose calculation algorithms for proton spot scanning. With increasing sophistication of computers, it is likely that MC methods will overtake analytical methods for dose calculation in the very near future.

1.6. Project Overview

Proton therapy is becoming a mainstream cancer treatment option. With the advancement of proton therapy, newer and more accurate dose calculation engines are being released in the market. However unlike photons, there is a great dearth of commissioning and validation information for proton treatment planning systems (TPS). Unlike photons, there are no AAPM task group reports that can serve as a guidance document. This dissertation provides validation of two commercially available dose

calculation engines, i.e. Analytical and Monte Carlo distributed by RaySearch America. In chapter 2, we provide results of the commissioning and validation of RayStation's analytical algorithm for proton spot scanning. The beam data measurements were performed in the fixed gantry room of the Seattle Cancer Care Alliance Proton Therapy Center (SCCA-PT). A journal article summarizing the findings of chapter 2 was successfully published in International Journal of Proton Therapy in March 2016. In chapter 3, the dosimetric validation of RayStation's Monte Carlo (RS-MC) algorithm will be described including a discussion of simulation and measurement techniques. A beam model (G-MC) for the gantry room of the SCCA-PT center was created in the GATE code. The benchmarking between G-MC and RS-MC was performed for a variety of simulations in virtual homogenous and heterogeneous phantoms. In addition, validation of RS-MC was also performed against measurements in similar geometries to the simulations. The results of the validation were summarized in a manuscript that is published in the journal Physics in Medicine and Biology. In chapter 4, the G-MC model was used to evaluate a newly available ceramic fiducial marker for ocular melanoma. Fiducial markers are commonly used in radiation therapy for image guidance thus reducing the treatment margins. Most fiducial markers are however made up of high atomic number material that causes dose shadows in the underlying tissue. Ceramic markers have the promise to reduce the dose shadow while still maintaining the visibility on x-rays. We used our G-MC beam model to study the dose shadows caused by the marker and validated the results with measurements. The results of the evaluation were published in a technical note in Biomedical Physics and Engineering Express in Feb 2017.

CHAPTER 2 CLINICAL COMMISSIONING AND COMPREHENSIVE EVALUATION OF A COMMERCIALLY AVAILABLE PENCIL BEAM SCANNING TREATMENT PLANNING SYSTEM FOR PROTON THERAPY

2.1. Introduction

The physical advantages offered by protons due to their finite range and nature of their depth dose is leading to a surge in the number of new centers opening in the world and heavily in the United States (25). The current technologies used to deliver proton therapy are passive-scattering (PS), uniform scanning (US), and pencil beam scanning (PBS) (26-30). With PS, the lateral enlargement of the proton beam is done by placing either single or dual scatterers in the beam path. A range modulator wheel that is placed in the beam path before the scatterers rotates rapidly to generate a sequence of Bragg peaks with different ranges and weights. All these peaks are added together to produce a spread out Bragg peak (SOBP). A number of range modulator wheels are generally required to cover the clinically required combination of SOBPs. Another method of laterally spreading beam is through the use of uniform scanning, in which a proton beam is continuously scanned laterally using magnets. The proton beam scans a fixed pattern in the field for each layer. The relative weights of layers are chosen to produce a flat dose in SOBP. A range modulator wheel present in the beam path indexes to a particular track for the complete delivery of the layer. Once a layer has been delivered, the wheel rotates to next track with a different thickness. Both the passive scattering and US methods require field specific hardware such as compensators and apertures for target dose conformity.

PBS scanning is a relatively newer technology that can reduce the need for field-specific hardware (e.g. apertures and compensators) and offers better dose conformation to the target (31). In PBS beam delivery, a three dimensional target is divided into many slices. The dose is deposited from the most distal slice to the most proximal slice sequentially. Within each slice, the dose is deposited through individual spots that can have unique intensity and position. A major difference between PBS and US/PS comes due to the planning techniques used; PBS utilizes inverse planning techniques while US/PS treatment planning is done through forward planning methods. This is a big advantage for PBS as inverse planning provides the ability to have multiple dose levels in a target within a single field, also called dose painting. In addition, a PBS beam can be optimized to have both distal and proximal conformity of dose around the target.

Proton therapy has been clinically used since 1954 but there is still very limited data available that could be used as a resource for commissioning and verification of treatment planning beam models. In the US there are multiple commercial systems that offer the capabilities of planning with PBS, i.e. CMS XiO (Elekta CMS Software, St. Louis, Missouri), Varian Eclipse (Varian Medical Systems, Inc., Palo Alto, CA), and RayStation (RaySearch Americas, Inc., Garden City, NY). Gillin et al. (32) have provided their experiences of commissioning Varian Eclipse planning system on a Hitachi ProBeat delivery system at University of Texas M.D. Anderson Cancer Proton Therapy Center, Houston (PTC-H). The PTC-H system utilizes a synchrotron with the capability of delivering 94 discrete energies. Another study done at PTC-H by Zhu et al. (33) compared the beam models based on single and double Gaussian approximations

of the in-air spot profiles. Both of these studies were done for the Varian Eclipse planning system and Hitachi ProBeat delivery system. Thus far, there are no published reports about the commissioning methodology for RayStation TPS for proton PBS system of IBA's universal nozzle. Accordingly, this report presents details of the commissioning and verification process of RayStation PBS at our center. It is not intended that this should be a guideline or recommendation for the use of RayStation PBS planning, but other potential users may benefit from the approaches taken for the commissioning process.

The Seattle Proton Therapy Center (SPTC) is the first proton therapy center in the Pacific Northwest Region. The center has four treatment rooms that comprise a full 360 degree capable gantry room, two inclined beam rooms, and one fixed horizontal beam room (34). The gantry and fixed beam rooms have the capability to deliver the treatments using the PBS technology. Initially, the fixed beam room was commissioned in CMS XiO treatment planning system to plan with the PBS methods. After the RayStation (RS) planning system received FDA approval, the fixed beam room was re-commissioned in RS. The commissioning was completed in July 2014 and the system was released for clinical use.

2.2. Materials and Methods

2.2.1. The Fixed Beam Pencil Beam Delivery System

The SPTC fixed pencil beam delivery system is an IBA universal nozzle (Figure 11) that provides the proton beam at a single horizontal gantry angle. The protons are accelerated to 230 MeV in an IBA cyclotron before being extracted and transported to the beam line. The proton beam line consists of a degrader, energy selection system,

dipoles, quadrupoles and steering magnets. The proton beam spot is magnetically scanned through each layer of the target volume. Each spot within a layer can have unique MU ranging from minimum of 0.02 to maximum of 11. A three-dimensional target is divided into many slices and proton beams sequentially paint the dose from deepest slice to the most superficial slice. The system provides the clinically usable ranges as measured in water from 7.5 to 32.6 cm that correspond to proton energies 98.5 to 228.5 MeV respectively. The maximum field size available is 40 cm x 30 cm with spot sigma in air that varies from 3.5 mm for highest energy to 7.5 mm for lowest energy at the isocenter plane.

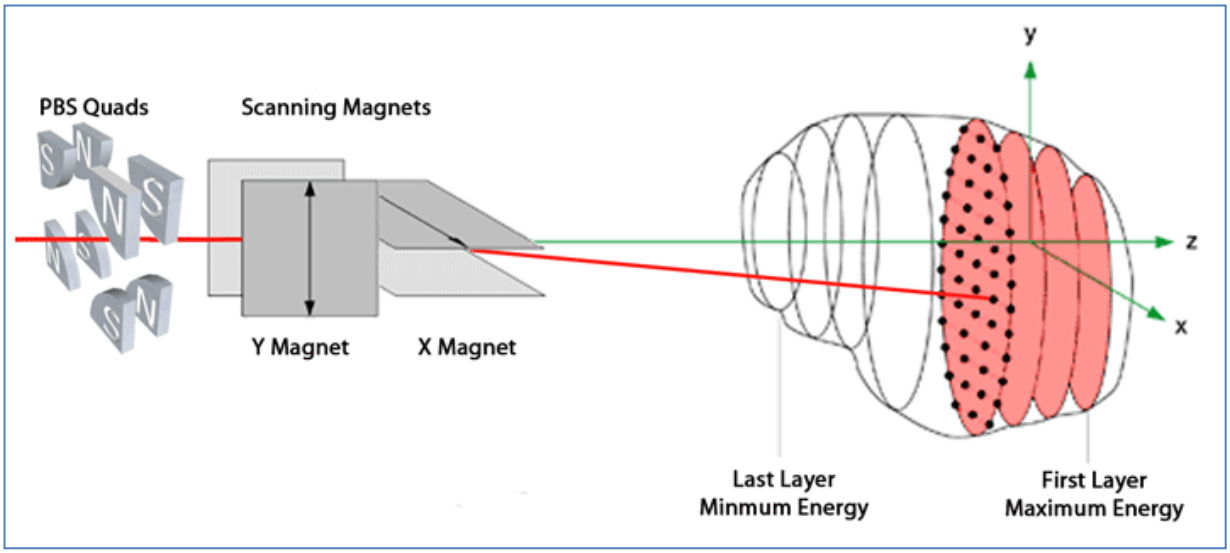

Figure 110: Schematic of the pencil beam delivery system at Seattle Proton Therapy Center

2.2.2. The RayStation treatment planning system

The RayStation (RS) treatment planning system distributed by RaySearch America was commissioned for delivery of PBS treatments. The beam data requirements for the commissioning were obtained from the vendor. The initial version (4.51) of RayStation models proton fluence through the air before hitting the patient or

phantom medium using a single Gaussian approximation. Correspondingly, the transport in the medium is performed using two Gaussian approximations. The first Gaussian accounts for the small angle multiple coulombs scattering (MCS) while the second Gaussian accounts for the nuclear interactions and larger angle MCS also called “nuclear halo”. In order to accurately account for the lateral inhomogeneities within the medium, each spot is split into 19 sub-spots for dose calculations. An example of measured vs the calculated spot profiles in air is shown in Figure 12.

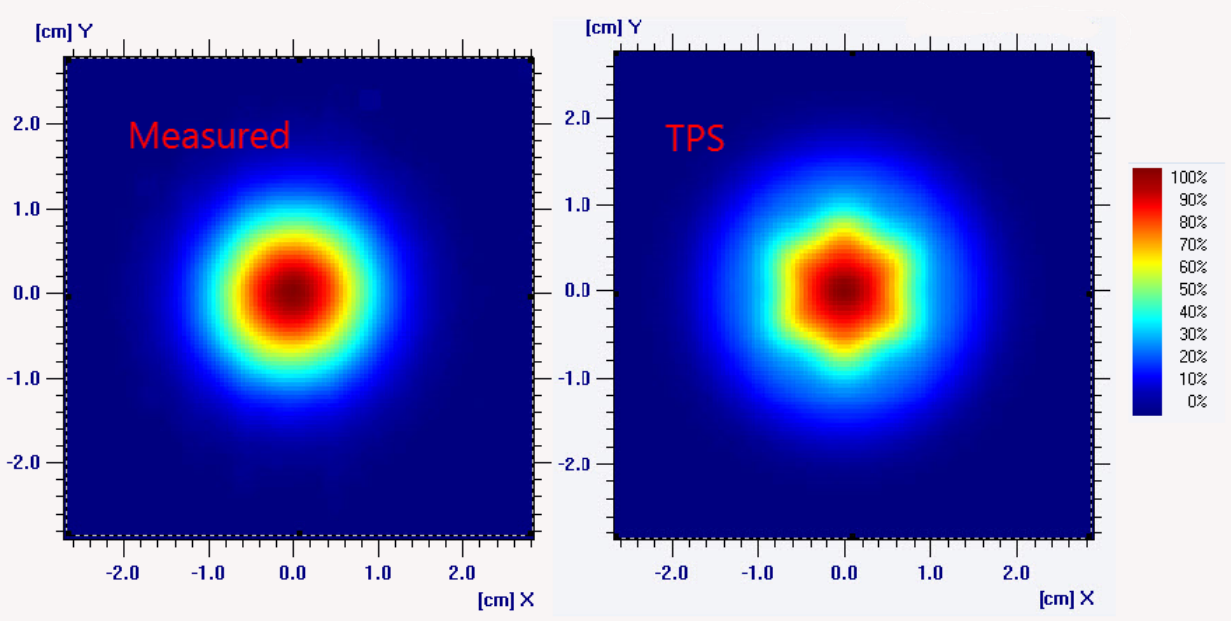

Figure 111: Example of spot profile measured and calculated in TPS. The RayStation TPS uses sub-spot resolution of 19.

2.2.3. Measurement of Beam Commissioning Data

The beam data measurements were done at 18 energies that were selected from the available energies of 98.5 to 228.5 MeV. These 18 energies were sampled at the regular interval of 7.5 MeV in accordance with TPS vendor‘s recommendation. In our clinic, the range of the beam is defined at the distal 90% of the Bragg peak (or

spread out Bragg peak). Table 1 lists the energies along with their corresponding ranges that were used for beam data measurements.

Table 1: 18 energies were selected from the available pool for beam data measurements. The spots for each beam were placed in a 25 mm rectilinear grid pattern for a total scanning area of 10.5 X 10.5 cm^2. Each spot was assigned MU value of 1 thus resulting in total MU of 1849 for the beam.

Energy (MeV)	D90 Range in Water (mm)	Depth of Measurement in Water (mm)	Total RBE Dose (cGy)
98.5	75.1	30	176.2
106.0	85.6	30	171.3
113.5	96.6	30	167.6
121.0	108.2	30	165.2
128.5	120.3	40	169.1
136.0	132.9	40	166.7
143.5	146.0	40	164.7
151.0	159.6	40	162.6
158.5	173.7	50	164.2
166.0	188.2	50	163.5
173.5	203.2	50	162.6
181.0	218.6	50	160.7
188.5	234.4	60	162.8
196.0	250.7	60	163.1
203.5	267.4	70	161.7
211.0	284.5	70	161.4
218.5	301.9	80	162.5
228.5	325.8	80	162.5

2.2.3.1. Integrated Depth Dose Measurements

The integrated depth dose curves (IDDC) were obtained for each of the 18 proton energies by scanning a large area detector in a proton beam with a continuous mono energetic single spot beam incident on the central axis. As the only available beam direction is horizontal, the presence of phantom wall in the beam direction requires the careful determination of water equivalent thickness (WET) of the wall. A custom phantom with 1D scanning abilities was manufactured in house. The phantom

has dimensions of 25 x 25 cm^2 in plane normal to the beam direction, with scanning ability of up to 36 cm in beam direction. This phantom has a front entrance window made up of acrylic with 1.45 mm thickness. By using a tank with such a thin window, any uncertainties in the determination of wall WET are minimized.

The IDDCs were measured using an 8 cm diameter integrating PTW Bragg Peak ionization chamber (PTW, Germany) and Sun Nuclear PC Electrometer (Sun Nuclear Corp., FL, USA). A large area detector such as the 8 cm Bragg peak chamber helps ensure that spots are adequately captured in the lateral direction. Integrated charge measurements at the interval of 1 mm were acquired for the entire length of the Bragg peak. The phantom was set up with the front face positioned at the isocenter. At each interval, at least 10 measurements were acquired to minimize the impact of any noise in the resulting data. The measured depth dose curves were shifted to account for the WET of the tank wall and effective point of measurement of Bragg peak chamber (4.2 mm). Generally these measurements are the most time consuming and therefore great consideration should be given to the methodology employed. The IDDC's were normalized to the same nominal value of 100 for all 18 beams and are shown in Figure 13.

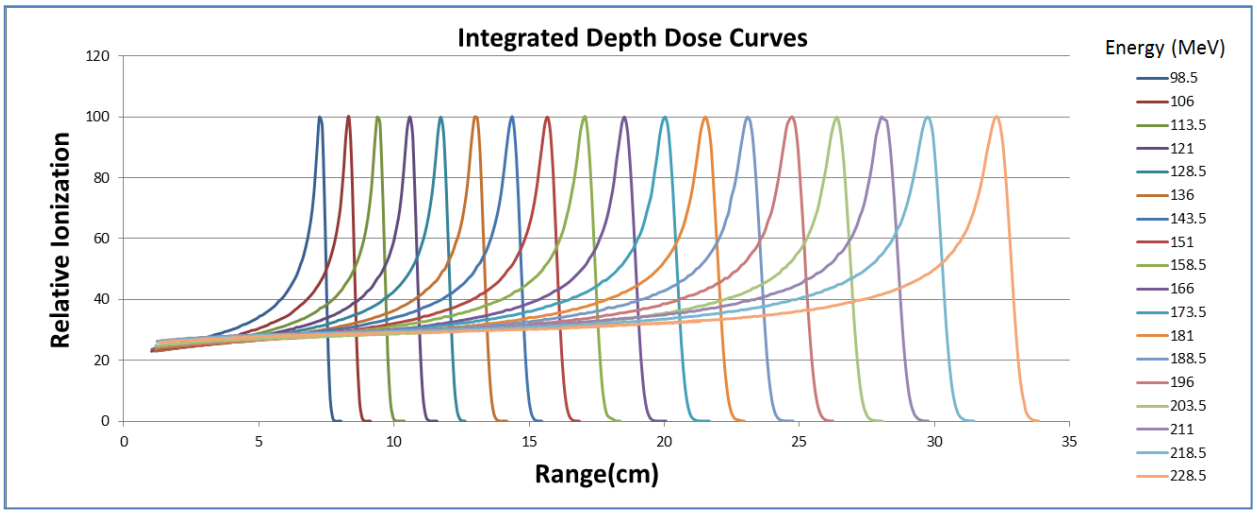

Figure 112: Integrated depth doses acquired using 8 cm Bragg Peak Chamber in a field with a single spot positioned on the central axis of the beam. The curves are normalized to common value of 100.

2.2.3.2. Spot Sigma Size and Virtual Source Position:

The spot profile characteristics are an essential part of the commissioning measurements. These measurements are performed in air using a high resolution 2D scintillation detector. The recommendation of the TPS vendor is to perform these measurements in at least five planes that cover the distances suitable for clinical use.

We used the Lynx 2D scintillation imager (IBA Dosimetry, Germany) for the measurements of spot profiles at five different planes; isocenter plane, 10 cm upstream, 10 cm downstream, 20 cm upstream, and 20 cm downstream. The spot profiles were measured in air (no build up) for the selected 18 energies. The planning system assumes that spot shapes are invariant with respect to lateral displacement in the scanned field. Figure 14 shows an example of a field that was created to measure spot sigmas. Sigmas for all 5 spots in a field were measured in both X and Y direction, with average values used in the planning system. A 2D elliptical Gaussian fitting was

used for the spot profile to determine the sigmas. Figure 15 shows the spot profiles for three given energies at isocenter plane.

The spot patterns obtained at different planes were used to calculate the divergence and subsequently virtual source-to-axis distance (SAD). The centroid of the spot can be plotted as a function of distance to obtain the SAD. As the scanning magnets in X direction are upstream of Y direction, the virtual SAD should be higher for X axis. The SAD values used in the TPS were averaged over all 18 energies.

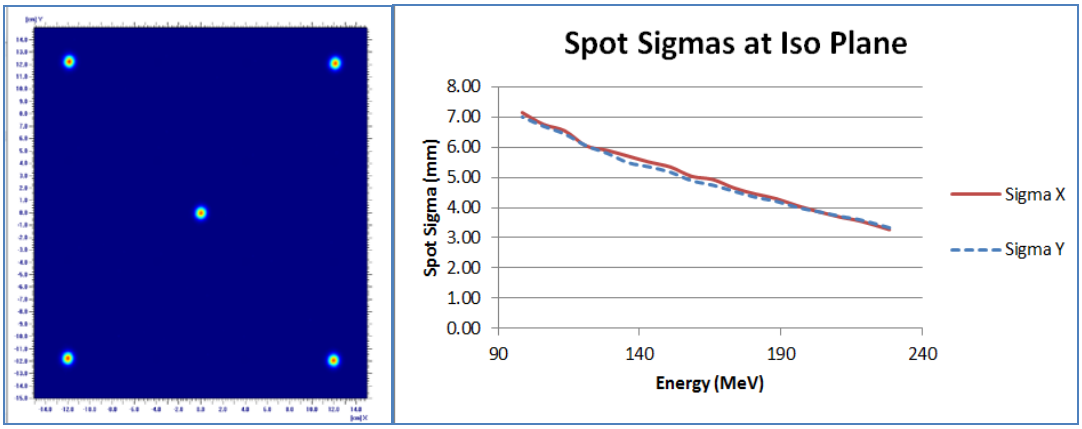

Figure 113: (a) Field with 5 spots was created to measure spot sigmas. The sigmas values were averaged for these 5 spots, (b) Variation of X and Y sigmas with energy at the isocenter plane.

2.2.3.3. Absolute Beam Calibration

The absolute beam calibration is based on measurements made in uniform unmodified single layer fields. Square 10 x 10 cm^2 fields were created with spots arranged in a uniform grid pattern with center-to-center spot of 2.5 mm. Each spot was assigned a value of 1 MU to create a laterally uniform profile (Figure 16). The RS TPS requires the measurements to be made approximately midway between 1 cm depth and the position corresponding to one half of the Bragg peak maximum. A water tank was set up with an ADCL calibrated PPC05 parallel plate ion chamber and electrometer for these measurements. The measurement parameters such as air gap, source to

phantom distance, detector depth, field size, and field specifications were clearly documented as these are needed for the beam modelling. The physical doses measured were scaled up by a factor of 1.1 so as to account for proton RBE. The results of the measurements are given in Table 1.

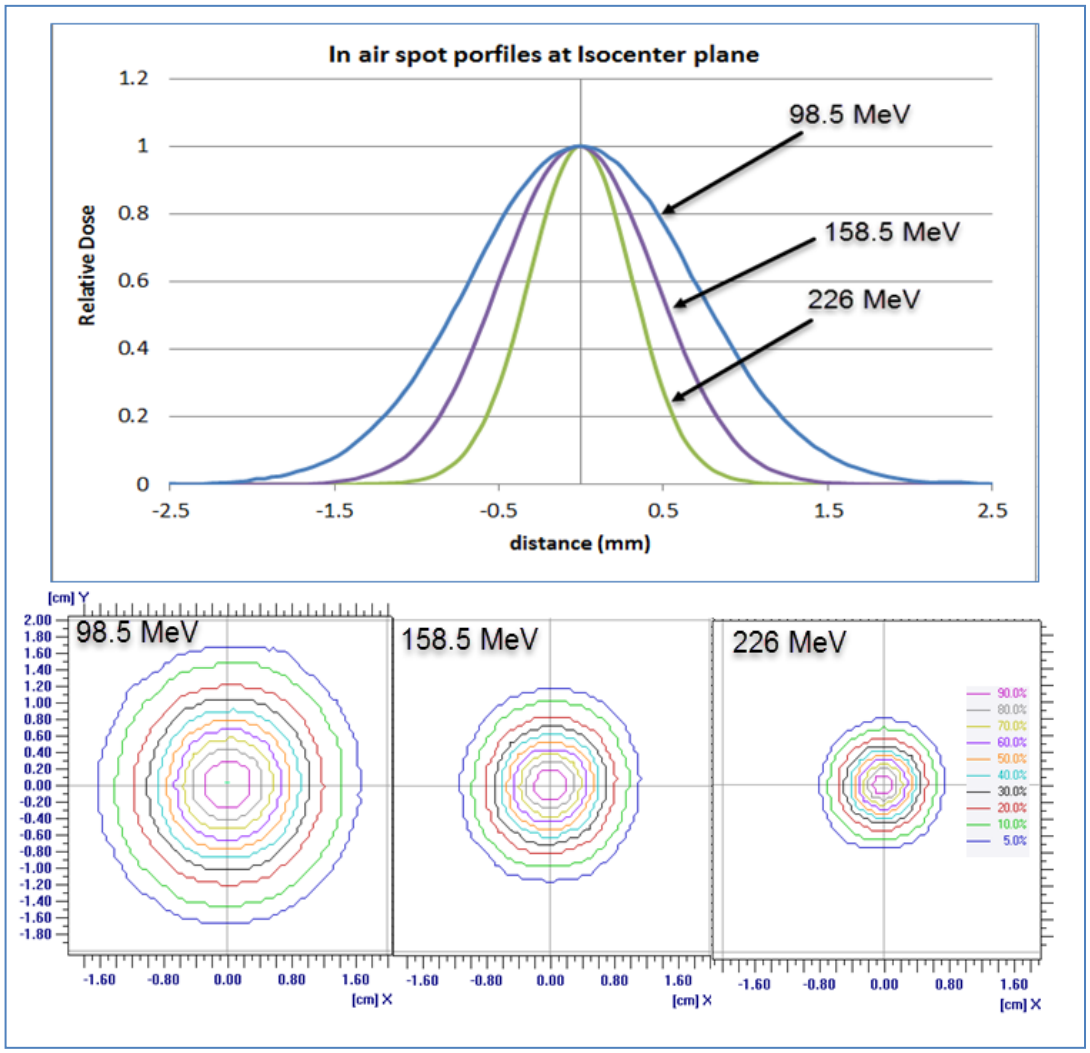

Figure 114: Spot profiles for three energies at isocenter plane in air.

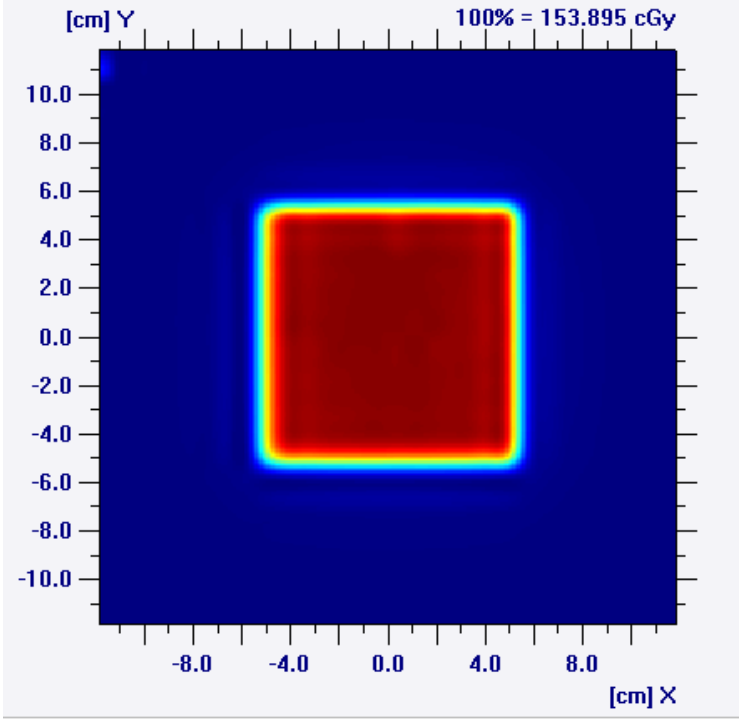

Figure 115: Single layer 10x10 cm fields used for absolute calibration of the beam.

The absolute relationship between dose-MU was performed in two steps. First, a relative model was obtained from RayStation based on the normalized IDDCs and dose measurements in single layer fields. This relative beam model was necessary to determine relative spot weights needed to create a uniform SOBP. It was then used to optimize a square field of 10 x 10 cm^2, Range = 20 cm, SOBP Width =10 cm to deliver 100 cGy (RBE) in the center of the SOBP. This beam is used for absolute calibration of the machine utilizing the IAEA TRS-398 protocol. The relation between dose and MU is arbitrary and completely dependent on user's clinical preferences. At our center, a value of 1000 MUs was chosen to deliver 1 Gy (RBE) in the center of SOBP for the above defined field. Therefore, the second step of establishing dose-MU relationship involved scaling the whole beam model so that 1000 MUs are required to deliver 1 cGy (RBE) in the center of SOBP for the calibration beam.

2.2.3.4. Beam Modelling Process

Currently, the beam modelling for pencil beam scanning is done directly by the vendor. All the beam data as well as non dosimetric data was sent to RaySearch. The name and ID of the machine, snouts, and range shifters were made to match the machine parameters defined in the Mosaiq (Elekta Medical Systems, Sunnyvale, CA)) Oncology Information System. The coordinate system for couch motion, gantry angles, and field scanning area should also be clearly defined.

2.2.4. Verification of Beam Model

The verification of the beam model consisted of evaluation of many different aspects; (i) spot profile, (ii) depth doses for single layer plans, (iii) absolute dose vs field size for single layers, (iv) depth doses of optimized SOBP plans, (v) absolute doses for SOBP plans, (vi) lateral dose profiles, and (vii) patient specific QA of mock phantom plans.

Table 2: Single layer plans corresponding to the given energies were created for field sizes 5x5 to 29x29 cm^2. Point dose measurements were made at above given depths, in entrance region and near Bragg peak.

Energy	Depth of Measurement (cm)	
	Near Entrance	Near Bragg Peak
98.5	2	5
113.5	3	6
128.5	5	8
143.5	5	8
158.5	5	11
173.5	5	14
188.5	5	17
203.5	5	20
211.0	5	22
218.5	5	23
228.5	5	26

To verify the modelled spot sizes, various phantom plans with a single spot located on the central axis were generated. The spot profile characteristics at the surface of the phantom were compared to measurement data obtained through Lynx 2D scintillator imager in the same set up. A maximum discrepancy of 1 mm was allowed between measured and calculated spot sigmas. In order to evaluate the change in dose at the central axis with field size, single layer (mono-energetic) beams were generated for square fields with sizes of 5 x 5, 10 x 10, 15 x 15, 20 x 20, 25 x 25, and 29 x 29 cm^2. These single layer beams have spots arranged in a uniform grid fashion with each spot assigned the same MU value. Eight different energies (Table 2) were sampled from the entire available range for the purpose of this evaluation. The combination of six field sizes and eight different energies resulted in total of 48 unique beams. Point dose measurements were made at two different locations along the Bragg peak, i.e. in the flat plateau region and another point near the Bragg peak. Furthermore, depth doses for 10 x10 cm field were also measured through Multi-layer Ionization Chamber (MLIC, IBA Dosimetry, Germany) and compared to the depth doses calculated in a virtual phantom. The point dose measurements were considered to be acceptable if measurements were within +/-3% of the calculated. The pass criteria for the depth doses were to have accuracy of the distal edge within 1 mm and local point-to-point dose difference to be <3%.

To validate point doses, depth dose curves, and lateral profiles phantom plans were created to deliver uniform dose to box targets. 3-dimensional targets corresponding to field sizes of 5x5 to 25x25 cm^2, ranges 7.5 to 32.5 cm, and widths 0.5 to 22 cm were created in a phantom. Each target was inversely planned to deliver a

uniform dose within the SOBP region using a single beam. Figure 17 shows an example plan corresponding to range of 22 cm, SOBP width 10 cm, and field size of 10 x10 cm. A total of 28 plans were made as shown in Table 3. These plans were delivered and measurements for point doses, PDDs, and lateral profiles were made. Based on the initial verification measurements, additional plans were generated to investigate any areas of disagreement in the beam model. The point dose measurements were performed using the calibrated PPC05 parallel plate chamber at multiple locations in the SOBP region as well in the entrance region. Additionally, for plans with field sizes smaller than 10x10 cm^2, percent depth doses were obtained using the MLIC. Because of the internal electronics, the MLIC cannot be used for any field sizes with a side greater than 10 cm. A depth dose measured through the MLIC represents the average charge collected in the central 2.5 cm diameter disc corresponding to the size of the ion chamber. Therefore, it is imperative that the uniform dose plans have flat profiles in the lateral direction to have a fair comparison with the MLIC measurements. The profile measurements were performed using either radiographic film or MatrixxPT (IBA Dosimetry) at one to four depths in the SOBP region. The following tolerances were employed for analysis: point dose accuracy +/- 3% of the calculated; SOBP depth doses +/- 3% at any point along the curve; and range accuracy +/- 1 mm. For profiles, a tolerance of 1 mm was allowed for comparison of full width half maximum (FWHM) determined by TPS vs measurement.

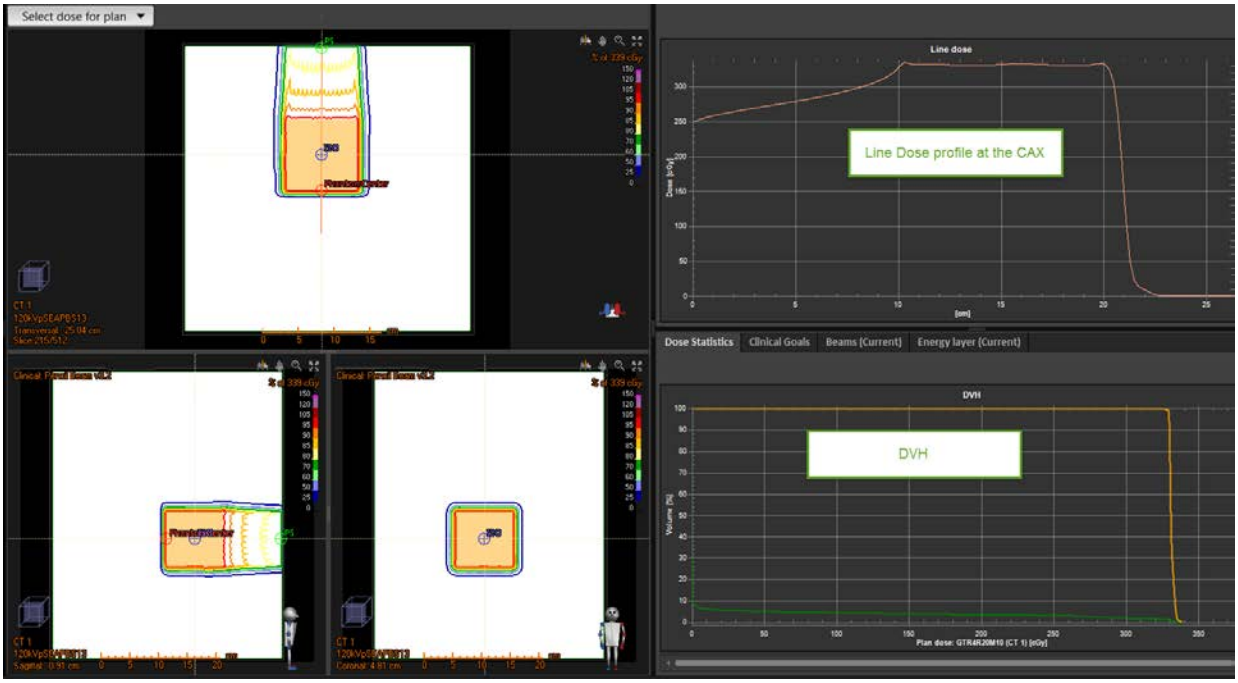

Figure 17: Single beam uniform dose phantom plans for TPS validation were created. The beam is inversely optimized to give flat dose profile within the SOBP region.

Table 3: List of uniform dose plans corresponding to given range, SOBP width, and field size that were created as part of treatment planning system verification.

Range	SOBP Width (mm)	Field Size (cm)	Planned RBE dose at center of SOBP (cGy)
85	10	10x10	350
100	20	10x10	200
120	40	20x20	200
130	50	10x10	350
160	70	8x8	200
180	100	8x8	200
200	100	10x10	200
200	100	15x15	400
200	100	20x20	260
210	120	6x6	200
240	150	6x6	200
260	40	25x25	200
260	80	20x20	200
270	100	5x7	350
290	100	5x5	350
290	200	10x10	200
290	100	10x25	200
290	50	10x10	200
300	50	10x10	400
300	50	25x10	200
310	150	10x10	200
310	220	5x5	350
320	50	10x10	400
320	200	10x10	200
320	100	20x20	200
325	60	20x20	350
325	100	5x5	350
325	20	25x5	400

The final component of the verification process involved the evaluation of overall accuracy for treatment planning and the delivery of realistic clinical plans. AAPM report TG-119 pertaining to IMRT commissioning has provided several planning exercises for institutions commissioning their IMRT systems (35-36). In the absence of any such standard guidelines for proton spot scanning systems, we adopted some aspects of TG-119's planning and delivery exercise for testing of our system. The CT dataset

along with relevant structure as provided by TG-119 were imported into a mock patient in the planning system. The report and the associated documentation comes with the standard test cases and the planning goals, further details of which can be found on the AAPM website. The following beam arrangements were used for developing these plans; (i) a three field multi-target, (ii) a two field prostate, (iii) a two field head and neck, (iv) a three field C-shape target with easy constraints, and (v) a three field C-shape target with difficult constraints. The plans were optimized using the multi field optimization (MFO) methods i.e. all beams optimized simultaneously to achieve the desired goals. The planner was given the flexibility to achieve the given dose-volume goals by creating appropriate objectives and constraints in the prescription. The final plans were mapped to a solid water phantom and doses recalculated. Each beam was delivered and measurements performed at multiple depths using the MatrixxPT detector. The analyses were performed on a beam-by-beam basis and quantified using the gamma index. A tolerance of 3% /3 mm was used with a minimum pass rate of 90% for gamma index analysis along with a dose threshold of 10%.

2.3. Results

2.3.1. Spot Profile Analysis

The results of the spot analysis are shown in Table 4. The maximum deviation of the sigma was noted for lowest energy to be 0.6 mm. The deviation between the measured and calculated sigma values in air was found to be within tolerance. The observed deviation of spot sigma in Y axis was worse than the X axis. The TPS systematically underestimated the Y axis sigmas values by 0.3 to 0.6 mm. This may be attributed to the fact that each spot is composed of 19 sub-spots (Figure 12) to

accurately account for lateral inhomogeneities. By representing each spot with 19 sub-spots, there is a difference in X and Y axis spot projections that could result in modeled sigma slightly larger in Y axis.

Table 4: Results of the spot profile analysis between measured and TPS calculated spot sigma values at Isocenter plane in air. The measurements were performed with an IBA Lynx.

Energy (MeV)	TPS		Measured			
	Y	X	Y	X	ΔY (mm)	ΔX (mm)
98.5	6.4	6.9	*7.0*	*7.1*	0.6	0.3
106	6.1	6.7	*6.7*	*6.8*	0.6	0.0
113.5	5.9	6.5	*6.4*	*6.5*	0.5	0.1
121	5.5	6.0	*6.1*	*6.0*	0.6	0.0
128.5	5.3	5.8	*5.8*	*5.9*	0.5	0.1
136	5.1	5.6	*5.5*	*5.7*	0.4	0.1
143.5	5.0	5.4	*5.3*	*5.5*	0.4	0.1
151	4.8	5.2	*5.2*	*5.3*	0.4	0.1
158.5	4.5	5.0	*4.9*	*5.0*	0.3	0.1
166	4.4	4.8	*4.7*	*4.9*	0.3	0.1
173.5	4.2	4.6	*4.5*	*4.6*	0.3	0.1
181	4.0	4.4	*4.3*	*4.4*	0.3	0.1
188.5	3.9	4.2	*4.2*	*4.3*	0.3	0.0
196	3.7	4.0	*4.0*	*4.1*	0.3	0.0
203.5	3.6	3.9	*3.9*	*3.9*	0.3	0.0
211	3.4	3.7	*3.7*	*3.7*	0.3	0.0
218.5	3.3	3.6	*3.6*	*3.5*	0.3	0.0
228.5	3.1	3.3	*3.3*	*3.3*	0.3	0.0

2.3.2. Depth Doses for 10x10 cm Single Layers

This is a relative comparison of depth doses measured through the MLIC and calculations done in the TPS. The normalization depth was selected to be the same as what was initially chosen for absolute calibration (Column 3, Table 1). Figure 18 shows the measured and calculated curves for three energies; 98.5, 158.5, and 226 MeV. All of the measurements passed the +/-3% criteria between the measured and calculated

values. The maximum deviation between the measured and calculated range was found to be 0.3 mm.

2.3.3. Point Doses for Single Layers of Different Field Sizes

The difference between calculated and measured doses for single layer plans (Table 2) at two different depths, (i) near Bragg peak and, (ii) in flat entrance region, are shown for field sizes 10x10 and 29x29 cm^2 in Figure 19a and 19b respectively. A positive difference of the plots represent that the measured dose is higher than what is calculated by the TPS. The maximum difference for measurements near Bragg peak was found to be for largest field size 29 x 29 cm^2 at highest energy of 226 MeV to be 3.4%. A trend can be seen from the graph whereas the discrepancy between measured and calculated doses increases with the field size. A similar trend was also observed for other field sizes (i.e. 25x25 cm^2, 20x20 cm^2, and 15x15 cm^2). The higher differences for larger fields may be attributed to couple of reasons, (i) the use of an 8 cm Bragg peak chamber for pristine peak measurements will not collect any charge outside the active area, and (ii) the inability of the pencil beam algorithm to accurately account for the low dose region produced around the central spot which is called the “nuclear halo.” .

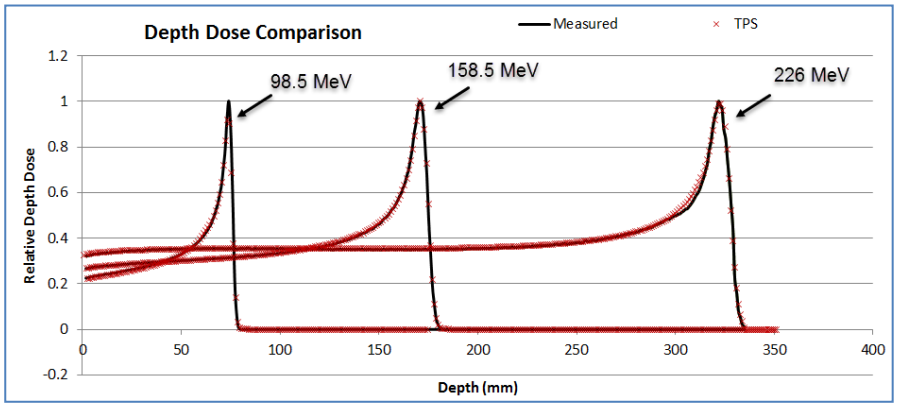

Figure 18: Evaluation of single layer depth doses for three different energies.

2.3.4. Depth Doses for SOBP Fields

For the 18 beams with field sizes smaller than 10x10 cm^2 (Table 3), central axis depth dose measurements were made using the MLIC detector. The maximum range error was seen for plans utilizing the highest energy and found to be less than 1 mm. All the points in measured depth doses were within 3% of the calculated values. Four cases of the depth dose comparison are shown in the Figure 20 along with the range, SOBP width, and field size of the plans. As can be seen, there is excellent agreement between measured and calculated depth doses.

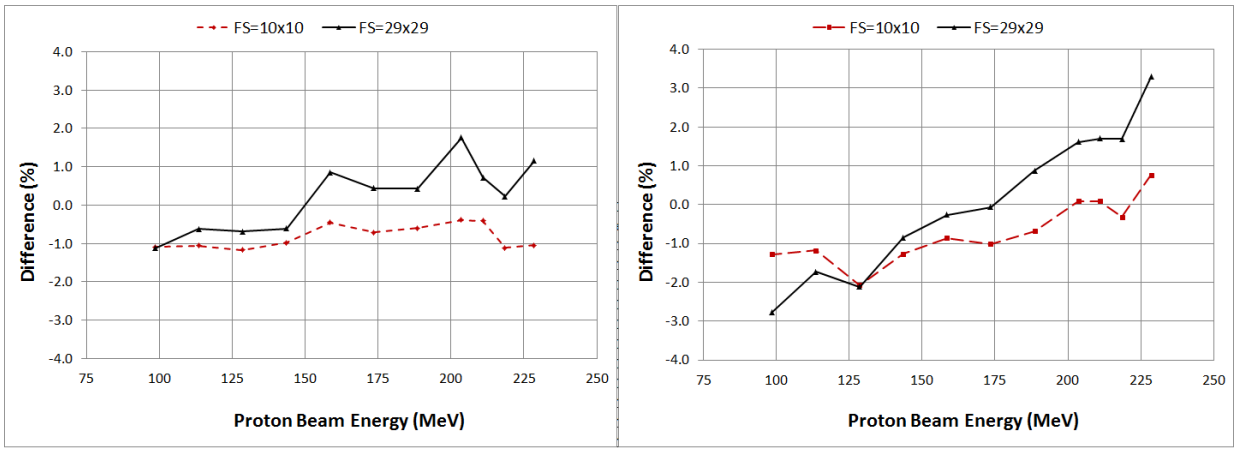

Figure 19: The percentage difference between calculated and measured point doses for field sizes 10x10 and 29x29 cm^2 at depths, (a) in entrance region; and (b) near Bragg peak. A positive difference on plot implies that measured dose is higher than calculated by TPS.

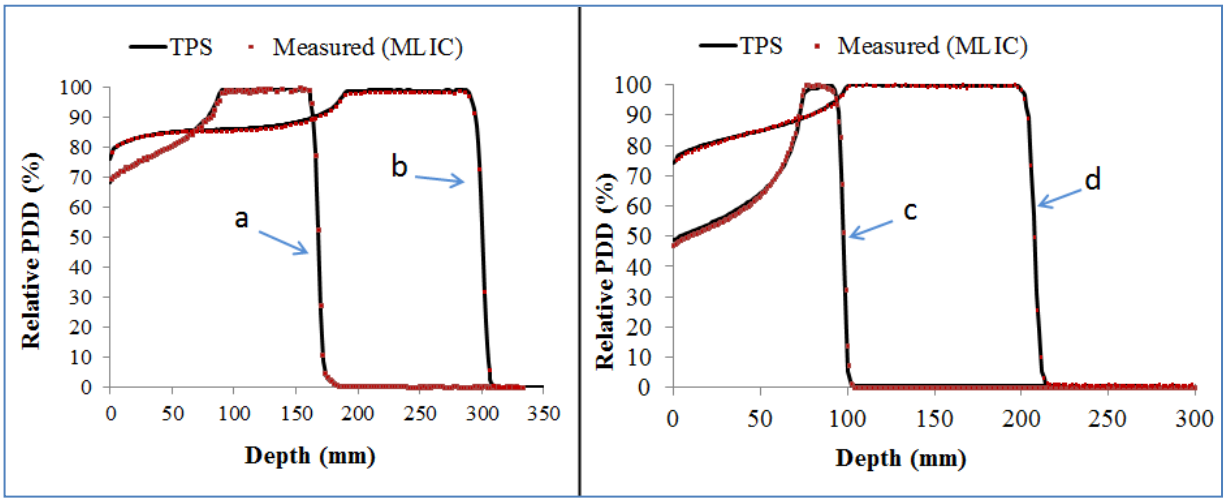

Figure 20: Central axis depth dose comparison for four cases; (a) Range =16 cm, SOBP Width = 7 cm, Field Size = 8 x 8 cm2, (b) Range =29 cm, SOBP Width = 10 cm, Field Size = 5 x 5 cm2, (c) Range =8.5 cm, SOBP Width = 1 cm, Field Size = 10 x 10 cm2, and (d) Range =20 cm, SOBP Width = 10 cm, Field Size = 10 x 10 cm2.

2.3.5. Absolute Point Doses for SOBP Fields

Figures 21 (a-c) summarize the percentage differences between the dose calculated by the TPS and measurements made on central axis in the middle of the SOBP as a function of range, field size and measurement depth for plans given in Table 3. As can be seen from these results, there are some point dose values outside the tolerance of +/-3%. Specifically, the percentage difference is larger than 3% for beams with ranges >30 cm, field sizes > 15x15 cm^2, and depths>25 cm. This may be related to the higher dose differences of up to 3.4% observed for point dose verifications in single layer plans. Since the SOBP plans are basically composed of many single layers with different weights, the dose differences from unmodified single layers are propagated to the complex inversely modulated SOBP plans. Both the impact of not measuring complete charge using the 8 cm bragg peak chamber for pristine peak measurements and the inadequacy of the dose algorithm to model low dose tails progressively gets worse with the increasing field size and the depth. The

maximum difference of 4.5% correlates to beam with range =32cm, SOBP width =5cm, field size =25 cm x 10 cm, and depth =31 cm.

2.3.6. Lateral Dose Profiles

Using the plans given in Table 2, the profile measurements were made at one to four different depths within the SOBP region as well as at 5 cm depth in entrance region. The measurements were performed using either EDR2 film (Carestream Health, Inc, NY) or a MatrixxPT ion chamber array device. Plans were selected to cover field sizes of 5 x 5 to 20 x 20 cm^2, ranges 8.5 to 32 cm, and SOBP widths 5 to 22 cm. Overall, more than 60 profile measurements were performed. The planned and measured profiles match well at both the shoulder and penumbra regions. The maximum deviation in full width half maximum was less than 1 mm. Figure 22 shows the profile comparison for four SOBP cases.

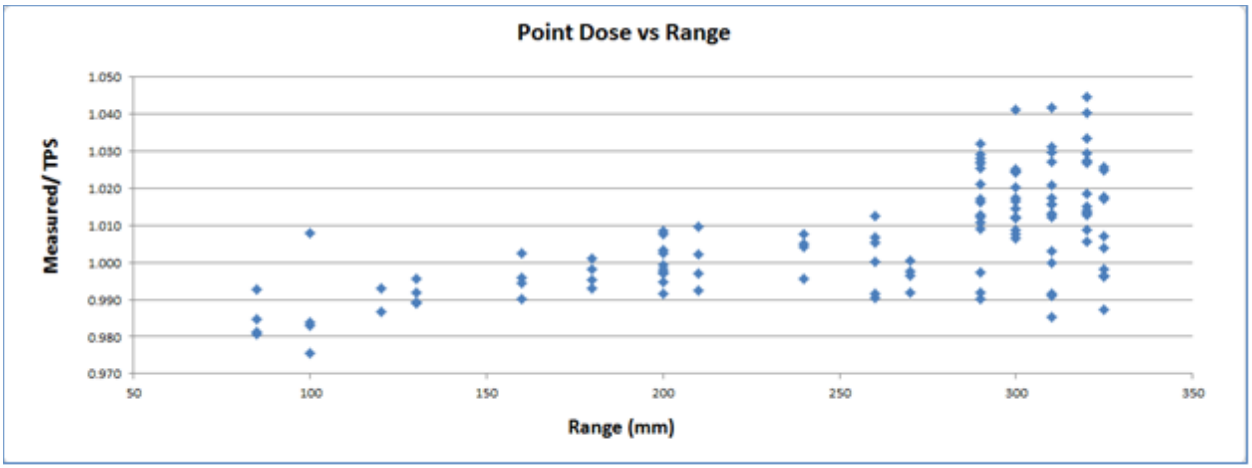

(a)

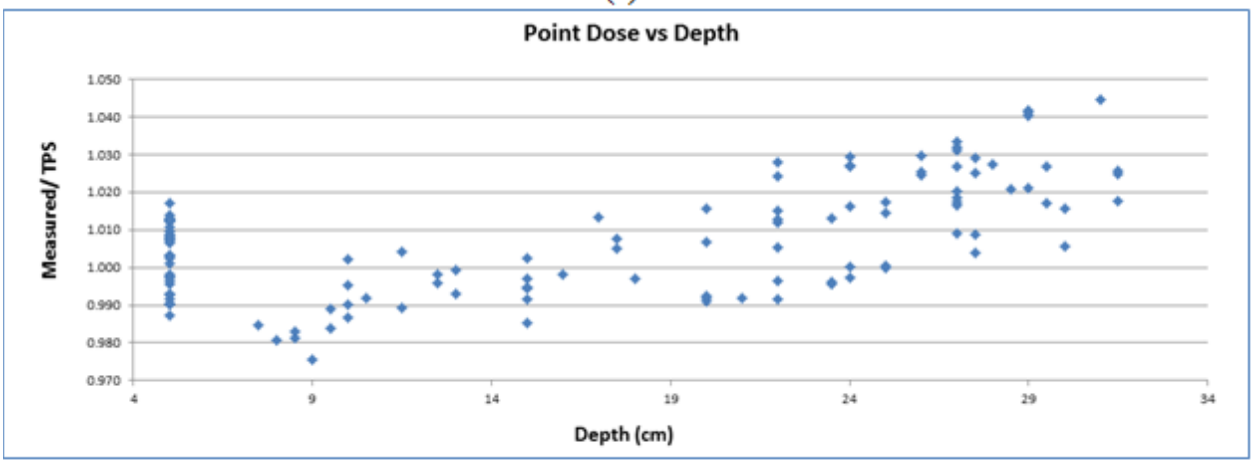

(b)

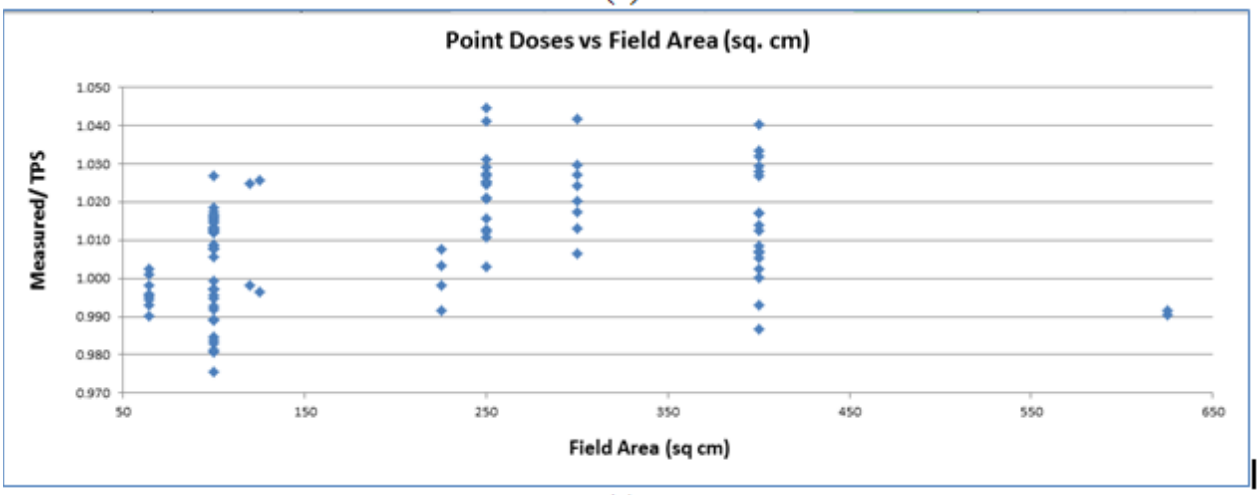

(c)

Figure 21: Ratio of measured over calculated point doses at the central axis for various plans given in Table 3 as a function of (a) Range, (b) Depth, and (c) Field Area

2.3.7. TG-119 QA Plans

The goal of these tests was to test the overall accuracy of the spot scanning planning and delivery system.

2.3.7.1. Test Plan P1: Multi Target

A three beam arrangement consisting of left lateral, vertex and anterior beams was used to optimize the three given dose levels. The planning system was successful in finding a solution that met all the given treatment plan goals as outlined in TG-119. The quality assurance of the plan consisted of the beam by beam delivery and verification using the 2D MatrixxPT array. Two to three planes were selected for each beam and analyzed for gamma index. The results are given in Table 5. The gamma pass rate for all the planes was greater than 94.5% at 3%/3 mm criteria.

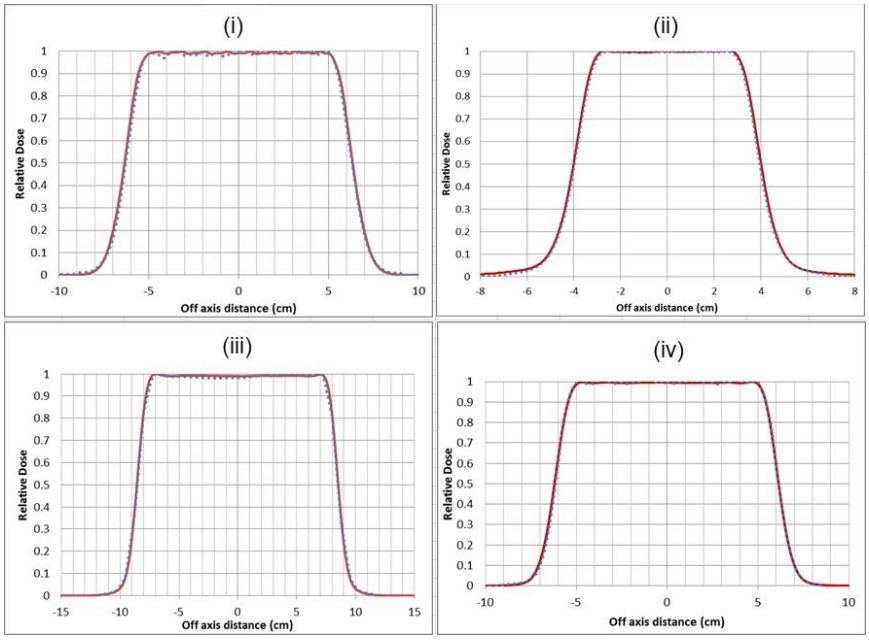

Figure 22: Comparison of measured and planned lateral dose profiles for four SOBP fields, (i) Range =8.5 cm, SOBP width= 1 cm, Profile Depth =8 cm; (ii) Range =13 cm, SOBP width= 5 cm, Profile Depth =10.5 cm; (iii) Range =20 cm, SOBP width= 10cm, Profile Depth =17.5 cm; and (iv) Range =32.5 cm, SOBP width= 10 cm, Profile Depth =23.5 cm.

2.3.7.2. Test Plan P2: Mock Prostate

The prostate target was irradiated by using two opposed lateral beams. All the treatment planning goals provided in TG-119 were met. The QA was done at two different depths for each beam i.e. at the proximal side of SOBP at 10 cm depth and in the middle of the SOBP at 15 cm depth. Table 5 shows the results of the gamma index analysis. The minimum gamma index for all the planes was 99.2% using the 3%/ 3 mm criteria.

2.3.7.3. Test Plan P3: Mock Head/Neck

The mock head and neck target was planned using two beams: left lateral and vertex. All the constraints given in TG-119 were met during the plan optimization. Three planes, one in proximal region and other two in the middle of the SOBP were picked for beam by beam quality assurance. The results of the gamma index analysis are given in Table 5. Also shown is the gamma analysis for vertex beam at a plane 10 cm depth in Figure 23. The minimum gamma index for all the planes was 99.7% using the 3%/ 3 mm criteria.

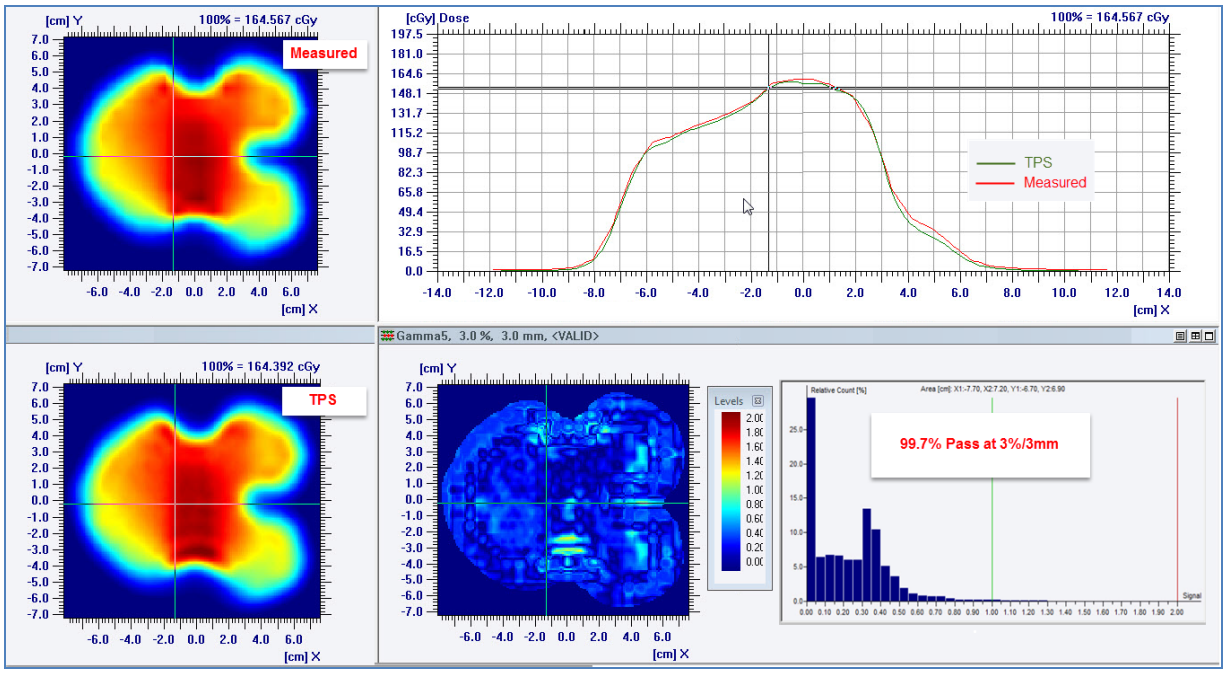

Figure 23: Gamma analysis corresponding to vertex beam of H&N plan at 10cm depth.

2.3.7.4. Test Plan P4: C Shape Target (easy and difficult constraints)

The first variant for this mock target case as given in TG-119 has relatively easy dose optimization constraints. The second variant has more difficult constraints with the idea of pushing the planning system harder. A three beam arrangement consisting of a left lateral, right lateral, and an anterior beam was used to optimize the desired dose levels. All the goals given by TG-119 were met for the target with easy constraints. The second variation with more stringent goals had two constraints that could not be met even after successive optimizations. The structures with violations are Core (5% of the volume to receive no more than 1000 cGy, achieved value = 23.3%) and CShape PTV (95% volume to receive at least 5000 cGy, achieved value = 84.1%). Two to three planes were selected for each beam for quality assurance. The results of the gamma index analysis are given in Table 5. The minimum gamma index for all the planes (both the easy and difficult constraints) was 92.8% using the 3%/ 3 mm criteria.

Table 5: Results of the field by field gamma index (GI) with 3%/3mm criteria at given depths for various targets outlined in TG-119. Only dose values greater than 10% of maximum were evaluated for GI.

Multi-target		C Shape Target- Hard		C Shape Target- Easy		Head and Neck Target		Prostate Target	
Left Lateral	GI(%)	Anterior	GI(%)	Anterior	GI(%)	Left Lateral	GI(%)	Left Lateral	GI(%)
d=10cm	97.6	d=8.5cm	94.6	d=8.5cm	97.4	d=10cm	100.0	d=10cm	100.0
d=15cm	94.5	d=4cm	97.8	d=4cm	97.9	d=15cm	99.8	d=15cm	99.6
						d=18cm	99.7		
Vertex		Left Lateral		Left Lateral		Vertex		Right Lateral	
d=10cm	98.9	d=10cm	99.1	d=10cm	98.4	d=10cm	99.7	d=10cm	100.0
d=15cm	98.0	d=13.5cm	99.8	d=13.5cm	100.0	d=12.5cm	99.9	d=15cm	99.2
d=20cm	99.5	d=15cm	94.8	d=15cm	92.8	d=19cm	99.8		
Anterior		Right Lateral		Right Lateral					
d=13cm	97.1	d=10cm	98.5	d=10cm	97.5				
d=15cm	98.5	d=13.5cm	99.2	d=13.5cm	98.5				
d=22	97.4	d=15cm	95.3	d=15cm	93.3				

2.4. Discussions

The clinical implementation of the RayStation proton pencil beam scanning system has been presented. The beam modelling for pencil beam in RayStation requires the IDDCs (or Bragg peaks) in relative units. In order to measure these Bragg peaks with a scanning ion chamber, a reference signal is required. The positioning of the reference detector in the beam path is difficult due to the small size of the spot. One way to mitigate this issue is to get a reference signal directly out of the nozzle MU chamber.

A trend can be seen in Figure 24 where the discrepancy between measured and calculated doses increases with the field size for higher energy. We found that the RayStation planning system underestimates doses for beams that have field sizes>15x15 cm^2 and energy >218 MeV. The maximum differences for some points were found to be as much as 4.5%. Most of these beams are rarely used in the clinic. The higher differences for larger fields and higher energies may be attributed to a couple of reasons: (i) The measurements of the IDDCs using an 8 cm Bragg peak

chamber will not account for any charge in the low dose region that is further than 4 cm from the central axis (16, 37-39), and (ii) the inability of the pencil beam algorithm to accurately account for the low dose region produced around the central spot which is called “nuclear halo.” Although a second Gaussian is used to model the nuclear halo, it may not be enough to model the low dose tails that are produced farther from the central axis. As the field size increases, this effect gets compounded by the addition of low dose tails at the central axis. Since the SOBP plans are basically composed of many single layers with different weights, the dose differences from unmodified single layers are propagated to the complex inversely modulated SOBP plans. The efficiency of an 8 cm BP chamber was estimated using the open source, highly validated GATE (Geant4 Applications for Tomographic Emission) code (40). The Bragg peak corresponding to 226 MeV cm was simulated for two scenarios: (a) charge collected in 8 cm diameter disc to simulate the BP chamber, and (b) charge collected in 40 cm slab to account for low dose tail (Figure 24). The maximum loss of charge was -8.3% at 21 cm depth. Although, it is very desirable to have a chamber bigger than 8 cm for IDDC measurement, at the time of our commissioning no bigger chamber was available. Even though our measurements were done with 8 cm, the validation results show that the performance of the TPS is clinically acceptable under most of the conditions. An 8 cm BP chamber was also used for commissioning purposes by Fracchiolla et al. (41).

Commissioning of range shifters is necessary to enable the treatment of shallow targets. In the version 4.5 of RS, whenever a range shifter is added to the beam path, the range shifter and the physical air gap are considered part of the patient geometry. The dose calculations are started at the upstream surface of the range shifter. The

result is a large inhomogeneity (air gap) in the beam path that is not handled well in RS version 4.5. Discrepancies as large as 8% were seen at the shallow depths for the thicker (7.5 cm WET) range shifter. One possible solution is to commission a separate beam model from spot profiles and IDDCs measurements made with the range shifter in place. This was not done as RS was developing an improved analytical as well as a MC dose algorithm.

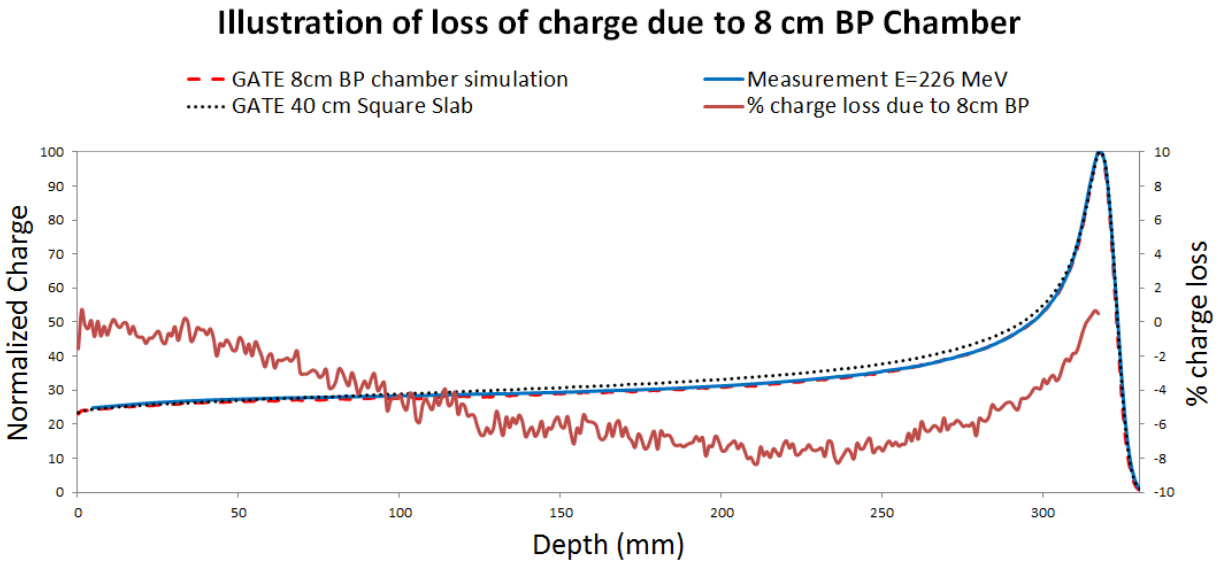

Figure 24: GATE Simulation illustrating loss of charge due to 8 cm Bragg Peak Chamber.

Prior to the clinical release of the TPS, an independent verification of dose-MU calibration was performed by a physicist not involved in the commissioning process. Later, calibration check OSLDs from the Imaging and Radiation Oncology Core (IROC, Houston, TX) were irradiated and the output was determined to be within 1%. In January 2015, a site visit was undertaken by an IROC team to credential the use of proton therapy in NCI-funded clinical trials at SCCA-PTC. As part of the credentialing process, various anthropomorphic phantoms (proton head, proton lung, proton prostate, and proton liver) were irradiated. After the successful irradiation of phantoms, site visit,

and calibration check TLD, the SCCA-PTC completed the IROC approval process and obtained the credentialing in April 2015.

The commissioning and verification methodology presented in this study can be used as a reference guide by upcoming proton therapy centers. Very often, the capabilities of a newly acquired TPS in terms of dose calculation accuracy and limitations are not known before the commissioning process. Our study will aid such centers and has a potential to reduce the variability of the proton PBS commissioning. This could further standardize the RT dose reporting in future multi-center trials utilizing pencil beam scanning.

2.5. Conclusions

A successful clinical implementation of RayStation TPS for pencil beam planning was performed. The beam model data requirements were obtained from the RayStation physics manual. Measurements were performed using a variety of detectors such as parallel plate ion chambers, 2D ion chamber arrays, Bragg peak chamber, 2D high resolution scintillation imager, and radiographic film. All the beam data was packaged and sent to a RayStation team for beam modeling process. The resulting beam model was put to a series of tests that involved verification of point doses, PDDs, profiles, and doses in patient specific plans. Tests were also done to study the variation of beam output with the field size. The results of the verification process were found to be adequate for clinical release of the TPS. The limitation of the planning system to accurately predict the doses for larger field and larger ranges were also noted. It was deemed that the cases exhibiting results outside the tolerances were less clinically

relevant. Subsequent upgrades to the planning system were anticipated to address some of the limitations.

The validation of analytical pencil beam algorithm was performed by comprehensive set of measurements in a water phantom. The accuracy of analytical pencil beam algorithm in determining accurate doses in water is no guarantee that algorithm will also be able to perform adequately in non-homogenous media. In non-homogenous media, additional consideration due to change in density and atomic composition of materials become important and need to be considered in the dose calculations. In next chapter, we have presented the results of validation of RayStation's Monte-Carlo algorithm in both homogenous and non-homogenous media. We have also contrasted the performance of analytical pencil beam algorithm to RayStation’s Monte-Carlo algorithm for a variety of test cases.

CHAPTER 3 DOSIMETRIC EVALUATION OF A COMMERCIAL PROTON SPOT SCANNING MONTE-CARLO DOSE ALGORITHM: COMPARISONS AGAINST MEASUREMENTS AND SIMULATIONS

3.1. Introduction

Accurate dose calculation is paramount in radiation therapy so that clinicians can make the most informed decision during treatment planning. Tumor control probability (TCP) and normal tissue complication probability are steep functions of absorbed dose in certain disease sites and therefore dose calculations with an accurate algorithm are necessary to plan treatments within a narrow therapeutic window. Most proton dose calculation algorithms can be assigned to two classes: analytic and Monte Carlo (MC). Analytical methods such as pencil beam algorithms (22-24, 42) involve the transport of energy fluence through infinitesimally narrow beams. Each beam is divided into many pencil beams that are ray-traced individually through the medium. For each pencil beam, the particles undergo elastic and inelastic interactions based on proton energy and the medium of interaction. The dose at any point is found by summing the individual contributions from all pencil beams. MC algorithms, on the other hand, track individual particles where for each interaction, energy loss and scattering effects are calculated through the random sampling of cross section data (43).

Most of the clinical dose calculations for proton spot scanning are carried out using pencil beam analytical algorithms as they are commercially readily available and provide fast and efficient dose calculations. However, analytical algorithms do not provide accurate dose calculation in heterogeneous media as multiple elastic Coulomb scattering as well as elastic and inelastic nuclear interactions can only be approximated in these algorithms (44). Analytical algorithms model patients as a stack of semi-infinite

layers - i.e. assuming materials encountered by the central axis of each pencil beam to be laterally homogenous slabs along the depth. This approximation is a major limitation in complex geometries where lateral inhomogeneities are not accurately accounted. MC algorithms do not suffer from these drawbacks as they track individual particle trajectories through material and therefore can provide accurate dose calculation in both homogenous and heterogeneous media. Several studies (45-52) have shown the importance of proton dose calculation using MC for certain sites. Scheumann et al. (48) assessed the impact of analytical dose calculation algorithms for various sites and found TCP differences of up to 11% for lung, head and neck and prostate patients. Another study by Grassberger et al. (49) showed an under-dosing of the CTV exceeding 5% for small fields in lung. Additionally, for larger lung tumors penumbra broadening was observed resulting in higher normal lung V5 and V10 values. These studies underline the importance of using MC dose calculations for clinical use in proton spot scanning.

There are many codes and packages available for MC calculations for protons including Geant4 (53, 54), MCNPX (55), FLUKA (56), and PHITS (57). In addition, there are toolkits and extension packages, such as Tool for Particle Simulation (TOPAS) (58), Geant4 Application for Tomographic Emission (GATE) (40), Pre-calculated Monte Carlo (PMC) (59), and MC-Based treatment planning tool (MCTP) (60), that wrap around one of these MC codes to provide an environment suitable for running radiotherapy MC simulations. However, most of these packages are research based applications and do not have FDA approval for clinical use. Due to their research-based nature, these packages do not offer all the features that are expected from commercial treatment

planning system (TPS) such as an intuitive graphical user interface, ability to import and export plans, and ability to visualize patient anatomies in a user friendly manner. In addition, the calculations are often too slow for routine treatment planning even with the aid of dedicated high performance computing resources. Recently, RaySearch Americas Inc. (NY) introduced a new commercial solution RayStation ver 6.0 (RS6) for MC treatment planning intended for clinical use and equipped with all the features expected from a modern TPS. RS6 provides users with the choice of two algorithms for dose calculation: analytical pencil beam algorithm ver 4.0 (RS-PBA) and a proprietary Monte-Carlo algorithm ver 4.0 (RS-MC). Both dose algorithms may be used to drive inverse plan optimization and final dose calculation. According to the manufacturer, RS-MC provides fast and accurate dose calculations for routine use in a clinical setting. However, the process of implementing a fast and efficient MC dose engine can often result in approximations for physical processes that could compromise the desired dose calculation accuracy. Accordingly, this report presents the validation of RS-MC using measurements performed in homogenous and heterogeneous phantoms, and simulations performed in the validated GATE MC package.

Our work for validating RS-MC is divided in the following phases:

- Developing a beam model (G-MC) for our gantry in the GATE MC toolkit using measured beam data. Validation of G-MC is carried out against measurements performed in a water phantom.
- Comparison between measurements, G-MC, RS-MC, and RS-PBA in homogenous and simple slab heterogeneous geometries for a variety of test cases.
- Comparison between RS-MC and RS-PBA in an anthropomorphic phantom.

3.2. Methods and Materials

3.2.1. RayStation Treatment Planning System

RS6 provides options for calculating doses for pencil beam scanning plans with either RS-PBA or RS-MC. The RS-MC dose engine does not require any separate commissioning and the same beam model that is used for RS-PBA dose calculation can be used for MC dose calculations. Our previous work (61) described the clinical commissioning of RayStation ver 4.51 for pencil beam dose algorithm. The commissioning of ver 6.0 is same as ver 4.5. All of the treatment planning calculations in this work were performed with a 1 mm isotropic grid. For calculations using RS-MC, the doses were calculated to have <1% statistical uncertainty.

3.2.2. SCCA Proton Therapy System

Measurements were performed in a proton gantry at the Seattle Cancer Care Alliance Proton Therapy (SCCA-PT) center. SCCA-PT is a four room center (34) with IBA Proteus Plus (Ion Beam Applications, Louvain-Neuve, Belgium) cyclotron and has capabilities to deliver spot scanning and uniform scanning beams. The spot scanning gantry offers full 360 degree rotation and provides a proton beam with continuous range in water from 7.5-32 cm (proton energies 98.5-226 MeV). The maximum available field size at the isocenter plane is 40 X 30 cm^2.

3.2.3. Development and Validation of G-MC Beam model

A beam model was commissioned in G-MC based entirely on measured beam properties at nozzle exit avoiding the modeling of any nozzle components as described here (62). The nozzle exit was placed 40 cm upstream from the isocenter plane in the simulation (Figure 25). 18 discrete energies (61) with a spacing of 7.5 MeV were

selected from the continuum of available energies 98.5- 226 MeV. For MC simulations, the recommendations provided by Grevillot et al (63) for different GEANT4 settings for proton particle therapy energy range were used. As recommended, 1 mm was used for the range cut (production threshold for secondary particles after EM interactions) and maximum allowable step size value (distance to next interaction). The pre-calculated EM tables for mean free path, restricted stopping power, and range were set to 20 bins per decade to accurately describe the EM interactions. The physics models were implemented using the pre-defined physics builder mechanism and included binary cascade along with option 4 for electromagnetic interactions. The ionization potential for water, important for accurate range modeling, was set to 75 electron volts based on the recommendations of ICRU reports 37 (64) and 49 (8). The voxel size was set to 1 mm^3 isotropically.

G-MC provides a mechanism to create a pencil beam source model by means of including all beam related parameters in a single “source-properties” file (62). The source-properties file has –x and –y direction polynomials related to spot size, energy spread (expressed as percentage of mean energy), and angular spread (beam divergence) as a function of energy. In addition, the source-properties file also needs information about the position of the scanning magnets and assumed nozzle exit position from the isocenter.

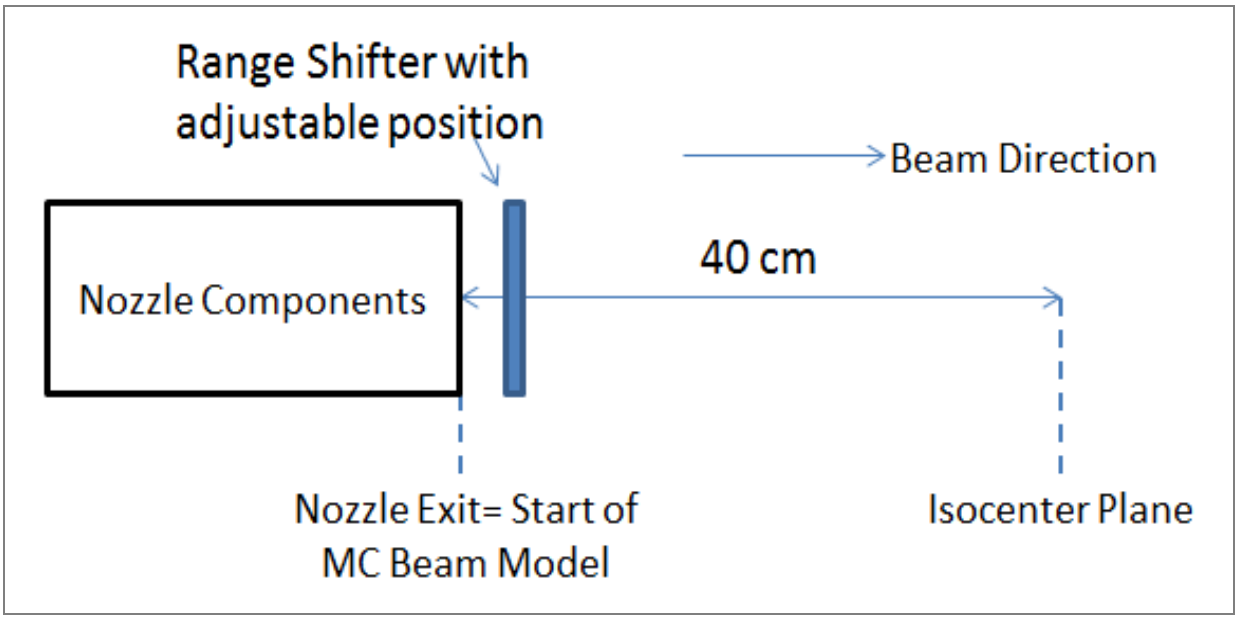

Figure 25. The G-MC model for the gantry beam at the SCCA Proton Therapy Center was created in GATE. The model, based on measured beam properties, started at the nozzle exit i.e. 40 cm upstream from isocenter.

The lateral profile of a single spot incident along the central axis for each of the 18 energies was measured using a two dimensional Lynx scintillator detector (IBA Dosimetry, Schwarzenbruck, Germany). These measurements were made at two planes i.e. at nozzle exit (40 cm upstream) and isocenter. The lateral spot profiles were fit to a 2-D Gaussian function and standard deviation values (spot sigma) were obtained for –x and –y directions. The enlargement of the spot sigma with the downstream distance from nozzle exit was used to calculate angular spread for all 18 energies. Six degree polynomial functions were obtained for variation of spot sigma and angular spread with energy and resulting coefficients were placed in the source-properties file. Integrated depth doses (IDDs) were obtained using the 8 cm Bragg Peak ionization chamber (PTW Inc., Freiburg, Germany) and a PC Electrometer (Sun Nuclear Corp., Melbourne, FL) with a single spot incident at the central axis. The IDDs were scanned with a 1 mm resolution. Simulations were carried out in G-MC using the same

geometry and beam set up with preliminary values of mean energy and energy spread. The mean energy was adjusted until the error in R80 (distal depth corresponding to 80% of maximum) depths for simulated and measured values was less than 1 mm. Similarly, the energy spread was adjusted in small increments to minimize the local error between the simulated and measured IDDs to less than 2% at any point. The measured and simulated IDDs were normalized to area-under-the-curve and analysis for dose-to-peak and mean point-to-point dose differences were performed as described here (41, 62). The final values of energy spread versus energy were fit to a six degree polynomial and resulting coefficients were placed in the source-properties file.

All the G-MC simulations were performed on a commercial MacBook Pro (Apple Inc., Cupertino, CA) laptop computer with 2.2 GHz quad-core Intel Core i7 processor, 16 GB of 1600 MHz DDR3L onboard RAM running the OS X Yosemite version 10.10.4 operating system. The G-MC doses were calculated for <2% statistical uncertainty.

3.2.4. Comparisons in Homogenous Media

Measurements were carried out in a water phantom for three different spread out Bragg peak (SOBP) combinations with field size of 10 x 10 cm^2: (i) SOBP1: Range=13 cm, Modulation = 5 cm, (ii) SOBP2: Range= 20 cm, Modulation= 10 cm, (ii) SOBP3: Range = 25 cm, Modulation=10 cm. These SOBPs were generated by inversely optimizing dose to box targets in the planning system using the RS-PBA algorithm. The beams were made perpendicular to the simulated water phantom without any beam modifiers (i.e. range shifter) to deliver uniform dose to the box targets. Once a SOBP was optimized, the plan was copied and re-calculated using the RS-MC algorithm. The

spot map and energy information of each layer was extracted from RayStation and converted to a G-MC compatible file. Finally, depth doses were calculated in G-MC by simulating the measurement geometry.

A four-way comparison of depth doses and lateral profiles was made between measurements, G-MC simulations, RS-MC, and RS-PBA. The depth dose measurements were conducted using a commercial multi-layer ionization detector (MLIC) (Zebra, IBA Dosimetry, Schwarzenbruck, Germany) that has 180 detectors and depth dose resolution of 2 mm. A tolerance of +/-3% was allowed for depth dose comparison between measured and calculated (RS-MC, RS-PBA or G-MC) for all points except at the distal edge. The distal edge was evaluated by comparing the range at R80 depth of measured versus calculated. The range was considered acceptable if the deviation from measured was less than 1 mm. The lateral profiles were measured at four different depths for each SOBP using the MatrixxPT detector (IBA Dosimetry, Schwarzenbruck, Germany). The calculated profiles were compared to measurements (reference dose) through a gamma index analysis (65) with a dose tolerance (DT) of 3% and distance-to-agreement (DTA) of 3 mm.

Range shifters are very common for proton spot scanning when treating a target that lies shallower than the smallest available range. Current analytical pencil beam algorithms are not able to accurately account for perturbations in dose distributions distal to the range shifter. RS-PBA accounts for a range shifter by assuming the range shifter and air gap to be part of the patient outline (66), where ray tracing starts at the upstream surface of the range shifter. This results in geometry with a very large inhomogeneity. Currently, the RS-PBA algorithm does not formally handle the transport

of secondary low energy protons that result from interactions in a range shifter. Since these are low energy protons, there is a greater dose discrepancy at shallower depths (<3 cm) when large air gaps (>10 cm) are used. In order to test the impact of the air gap between the range shifter and patient geometry, SOBP2 was measured at two different air gaps: 5 and 31.5 cm. A range shifter with water-equivalent-thickness (WET) of 7.5 cm (Base material = Acrylic, Physical Thickness = 6.5 cm) was inserted in the beam path and measurements were made using the MLIC detector. The measurement geometry was produced in G-MC and RS6 TPS to obtain depth doses at the central axis. Local dose differences between calculated and measured depth doses were analyzed.

For many clinical sites such as head and neck, breast and brain, use of oblique beams with a range shifter is necessary for sparing of critical structures. Generally, patient specific QA is performed by orienting the beam angles to have a normal incidence to a phantom. Unfortunately, this process could give a false sense of assurance in a treatment plan as some dosimetric errors are due to an inability of the analytical dose calculation algorithm to model obliquity, and will be missed. Analytical algorithms split a broad proton beam into many small pencil beams that are traced individually through a material. At oblique angle incidence, the protons will traverse different thicknesses of material within each pencil beam. However, analytical algorithms assume a constant thickness of material corresponding to the central axis of pencil beam. Thus, one could expect to see changes in the spectrum of proton energy as the beam travels through the medium, potentially impacting the shape of the distal edge. We created a test using SOBP2, range shifter of 7.5 cm, air gap 12 cm (at central

axis), to be incident on water phantom at 45 degrees (Figure 26). The depth doses at the central axis were calculated using G-MC/RS-PBA/RS-MC. Measurements were performed using the MatrixxPT detector in solid water at several depths with a 45 degree angle of incidence.

3.2.5. Comparisons in Heterogeneous Media

The goal of this test was to evaluate the accuracy of dose calculations by RS-MC/RS-PBA/G-MC due to interfaces created by placing bone or lung slabs in a water phantom. Figure 27 shows the phantom set up for these measurements. The bone or lung slab (CIRS Inc., Norfolk, Virginia) was placed at 15 cm depth in a water phantom to align the edge with the central axis of the beam. This was done to have only half of the SOBP beam to go through the heterogeneity so that an interface of lower and higher protons can be formed at the distal end of the beam. Since analytical algorithms use central axis approximation where the material at any depth is assumed to be laterally infinite, the range of proton pencil beam at the sharp interface due to the inhomogeneity is not properly handled. Due to this limitation, the calculated doses using analytical algorithms may exaggerate hot and cold spots in some areas near the central axis towards the distal edge of the beam. The atomic composition of the slabs was obtained from the manufacturer (Table 6) so that equivalent materials can be created in RS-TPS and G-MC.

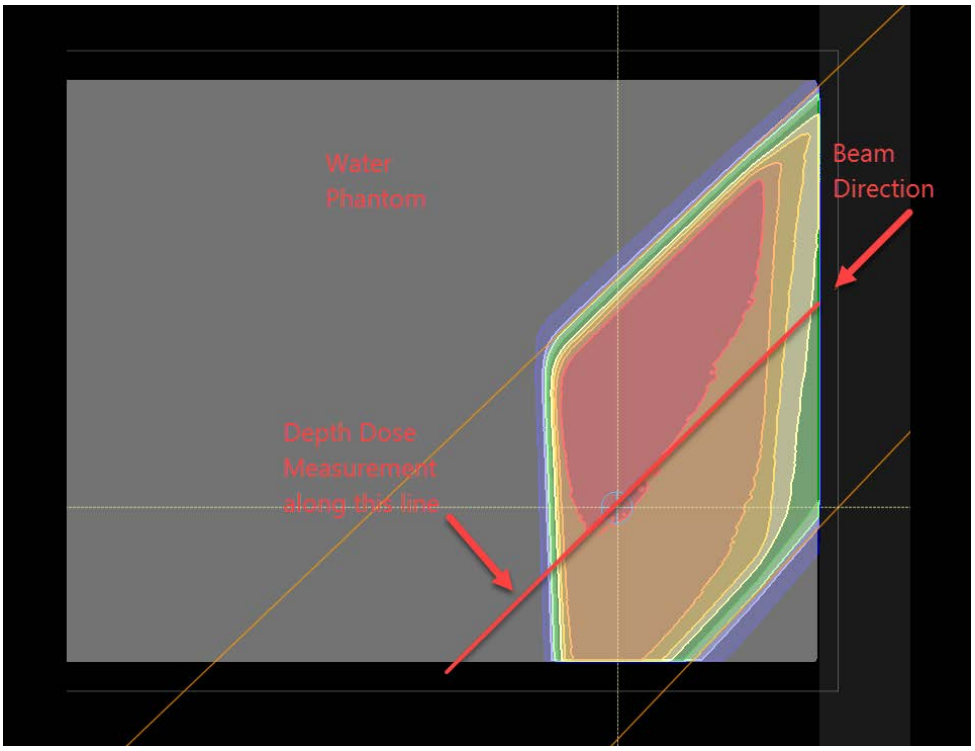

Figure 166. Depth doses at central axis were obtained for SOBP2 with oblique incidence (45 degrees). An acrylic range shifter with physical thickness of 6.5 cm (WET=7.5 cm) was placed at an air gap of 12 cm.

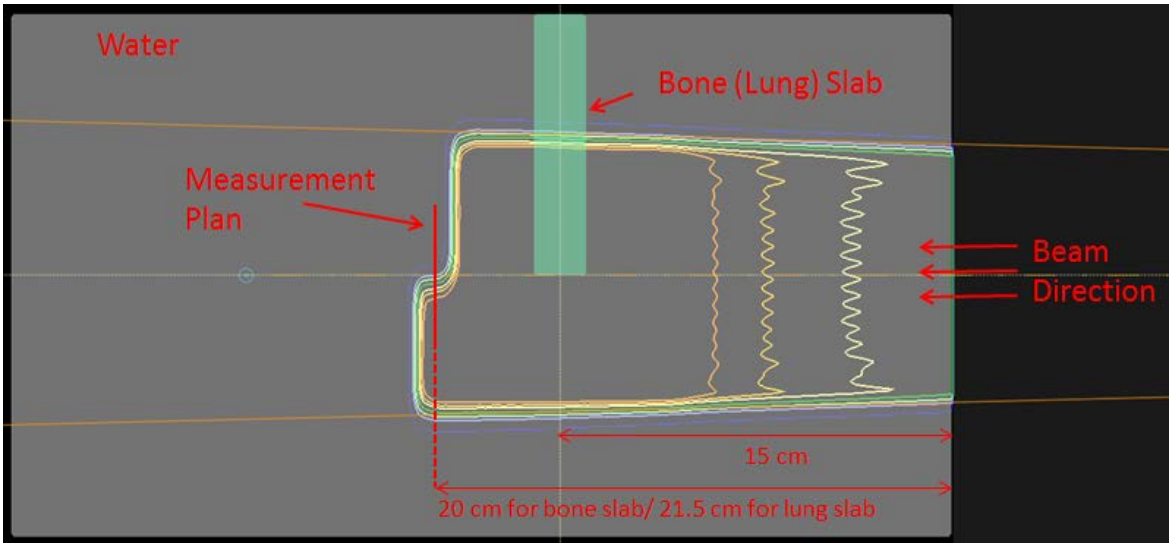

Figure 27. Inhomogeneous phantom with a bone or lung material equivalent slabs were created by placing slabs in a water phantom. The slab was positioned at 15 cm depth such that edge of the slab was aligned with the central axis of the beam. SOBP2 (Range= 20 cm, M= 10 cm) was used for measurement and simulations. The measurement was performed at the distal edge of the beam.

Table 6. Elemental Composition of bone and lung slab was obtained from manufacturer. Published with permission from CIRS Inc.

	Percentage by weight									
	Mfr. Product Name	C	O	H	N	Ca	P	Cl	Mg	Density (g/cc)
CIRS-Cortical Bone	BN20-10-CB	25.37	35.28	3.3	0.91	22.91	8.82	0.03	3.36	1.91
CIRS-Lung Medium	LU20-10-CB	54.78	25.71	7.91	2.47	0	0	0.95	8.14	0.307

Measurements and simulations were performed by using the SOBP2 beam. Dose profile measurement at the distal edge interface i.e. 20 and 21.5 cm for bone and lung respectively, were made using the microDiamond detector (Type 60019, PTW-Freiburg, Germany) and PC electrometer (Sun Nuclear Corp., Melbourne, FL). The MicroDiamond detector has been shown to be independent of dose rate and proton energy (67) and due to its small size, introduces a minimum amount of perturbation. Qualitative analysis was performed using the one dimensional gamma index analysis (tolerance: Dose =1% to 3% and DTA=1 mm) between measurement (reference dose) and GATE-MC/ RS-MC/RS-PBA.

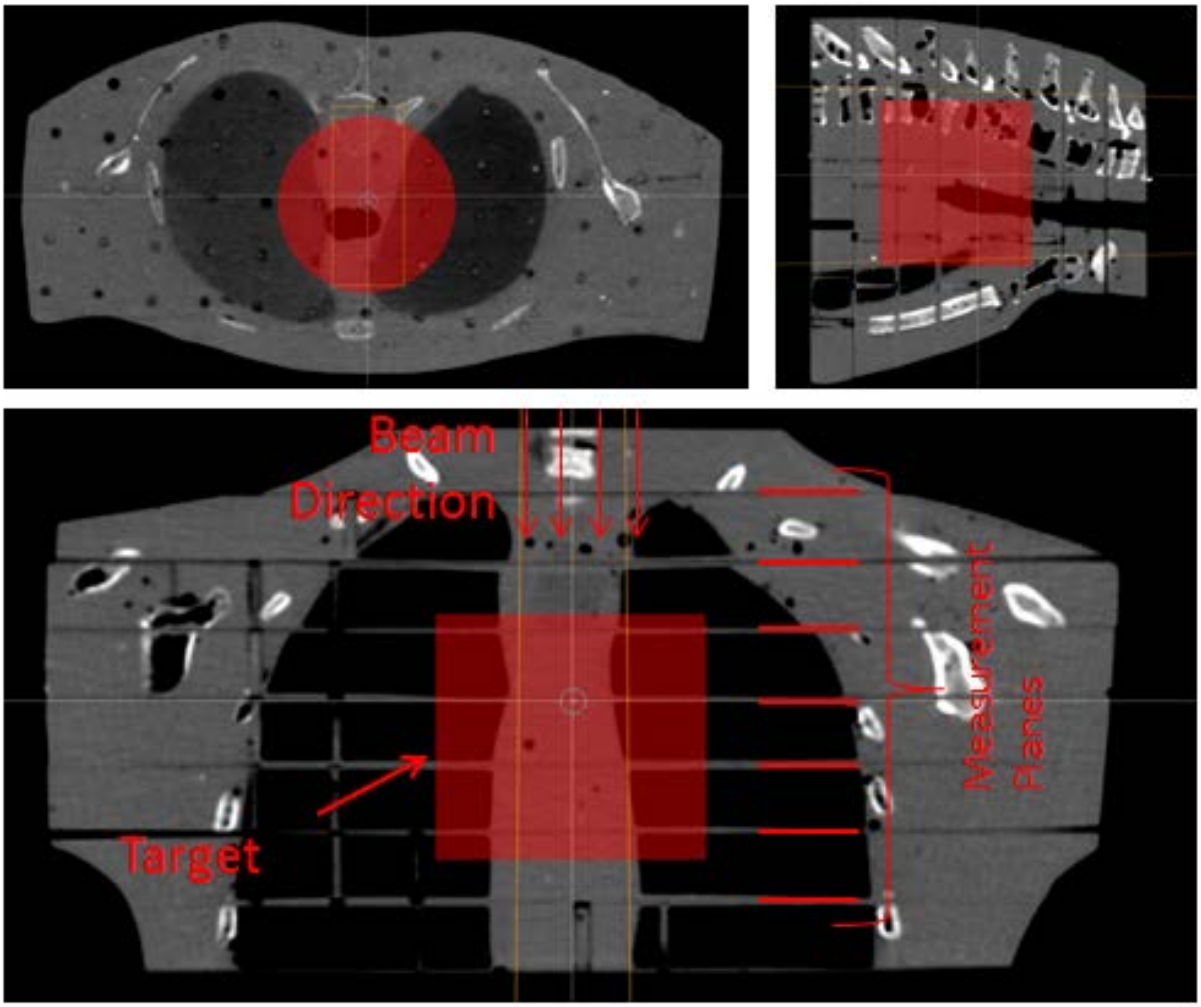

Figure 28. Axial, sagittal and coronal planes of the AR Phantom section with assumed cylindrical target (red shaded). A vertex beam (orthogonal to AR slices) was used to deliver uniform dose to the target.

3.2.6. Comparisons in Anthropomorphic Phantoms

In order to test the performance of dose calculation algorithms in clinical conditions, an Alderson-Rando (AR) (Radiology Support Devices, California, US) phantom section with heterogeneous anatomy (figure 28) was used for planning and measurements. The phantom section encompasses various tissues such as lung and mediastinum where inhomogeneities run parallel to the beam direction. Computed tomographic (CT) images of phantom were obtained using a GE Optima CT580

scanner (GE Healthcare, Waukesha, WI) with 120kVp and 1.25 mm slice thickness. The CT images were transferred to the RayStation treatment planning system for contouring and treatment planning. A quasi cylindrical target with a 10 cm diameter and 9 cm length was created in the phantom (figure 28). A treatment plan with a single beam incident orthogonally to slice direction was used to deliver 40 Gy (RBE) uniform dose in 10 fractions to the target. The beam direction was chosen to have lateral interfaces between lung and normal tissue that may not be accurately accounted for by analytical dose calculation algorithms. The plan was optimized using RS-PBA with a 1 mm grid size in –x, -y, and –z directions. The same plan was copied and also calculated using the RS-MC algorithm with a statistical uncertainty of <1%. The plan was transferred to the system Mosaiq (Impac Medical Systems, Elekta, CA) to be delivered to the AR phantom. Gafchromic EBT3 film (Ashland Inc., NJ) was placed between each slice of the AR phantom. The phantom was then placed on the couch to align the treatment isocenter with lasers. The irradiated films were scanned 24 hours post exposure on a flatbed scanner (Epson Expression 11000XL, Epson America Inc., California, USA) using 72 pixels per inch of resolution and landscape orientation. The digitized films were analyzed using the commercially available DoseLab software (Mobius Medical Systems, TX, US). A control film that was similarly handled but not exposed was also scanned to obtain net optical density using the red channel. The film doses were compared to doses calculated by RS-MC and RS-PBA algorithm using gamma index analysis (various DT and DTA tolerances). The dose profiles after every AR phantom slab were also measured using the MatrixxPT (IBA Dosimetry, Schwarzenbruck, Germany) detector. The doses from MatrixxPT detector were used to

scale the corresponding Gafchromic film doses at the same depth to obtain absolute doses needed for gamma index analysis.

3.3. Results

3.3.1. Gate MC Beam model validation

The lateral spot profiles expressed in terms of sigma values at the isocenter and nozzle planes are shown in figure 29(i). The variation of energy spread as a function of energy is shown in figure 29(ii). Our value of energy spread is in agreement with reported values in literature (41, 62). The maximum difference in range (as described by R90) between simulated and measured IDDs was -1.0 mm (proton beam of 218.5 MeV) and the average was less than 0.3 mm. The mean point-to-point difference between simulated and measured IDDs when normalized to area-under-the-curve was always less than 1.5%. In addition, the maximum difference at dose-to-peak for all 18 energies was -2%. The detailed results are shown in figure 30(i). These results confirm that the performance of the G-MC model is acceptable for benchmarking the RS-MC and RS-PBA algorithms. An example of simulated and measured IDD with the point-to-point error along the depth dose for energy of 226 MeV proton beam is shown in figure 30(ii).

The maximum difference in measured and modeled spot profiles at the isocenter plane is 0.12 and 0.09 mm for –x and –y directions with average differences of 0.05 and 0.03 mm in –x and –y directions respectively.

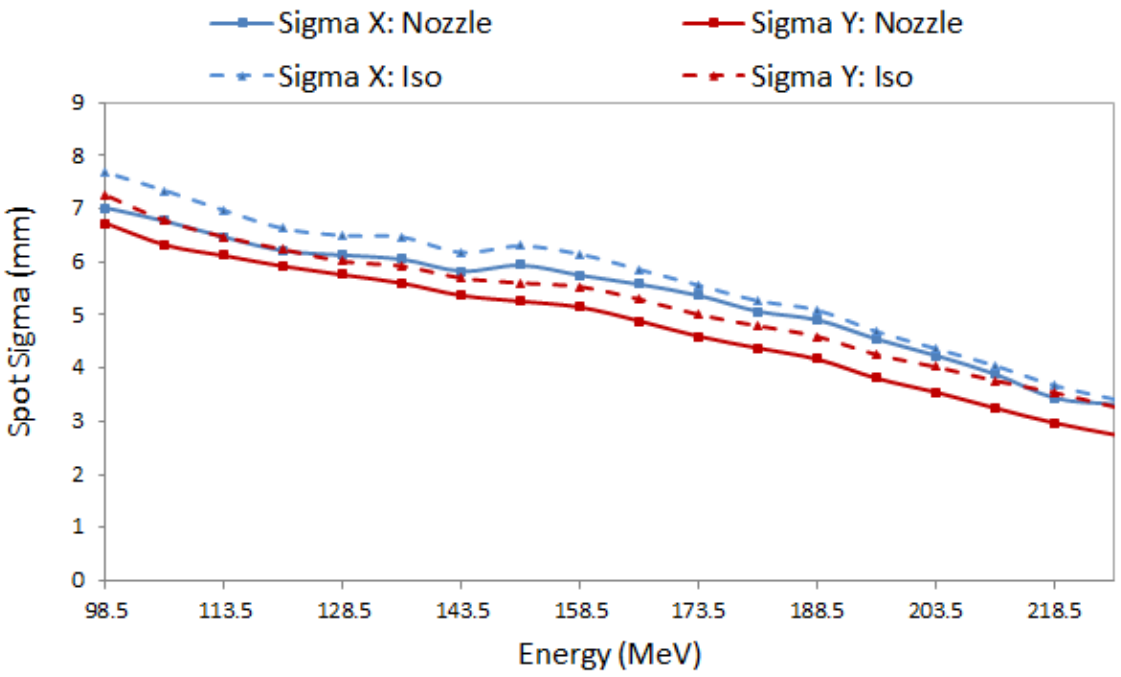

(i)

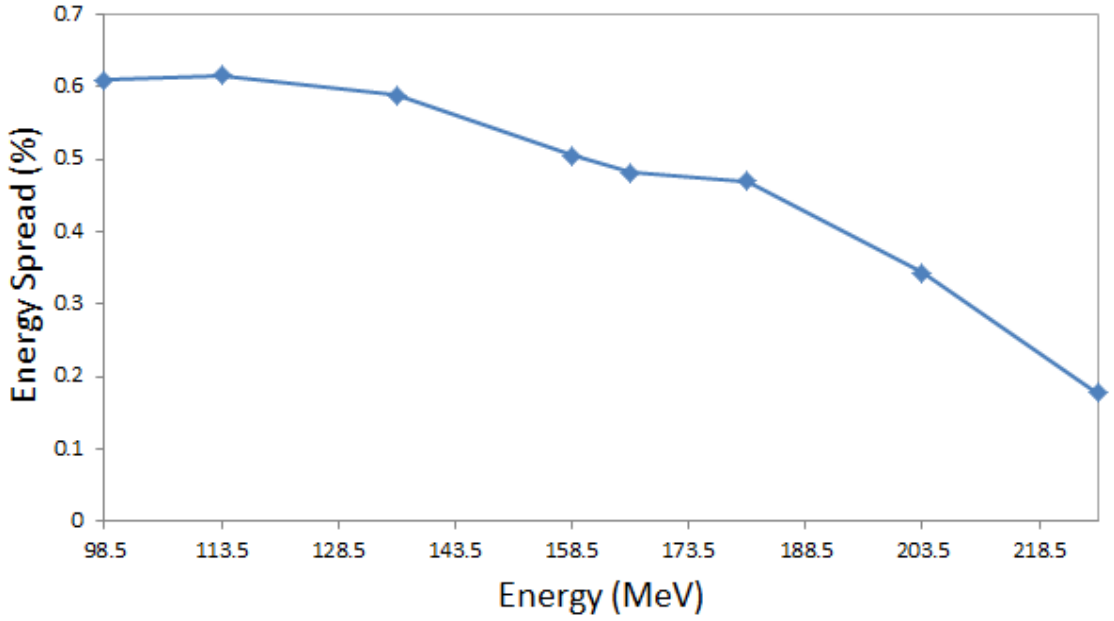

(ii)

Figure 29. (i) Variation of spot sigma with energy. The spot sigma values at the nozzle entrance i.e. 40 cm upstream of isocenter are shown for –x direction (blue solid squares) and –y direction (red solid squares). The spot sigma values at the isocenter plane are shown for –x direction (blue solid triangles) and –y direction (red solid triangles). (ii) Variation of percentage energy spread as a function of proton beam energy.

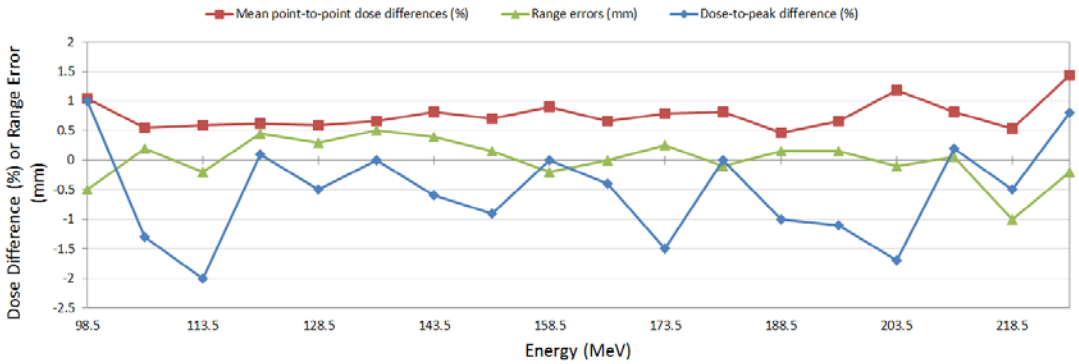

(i)

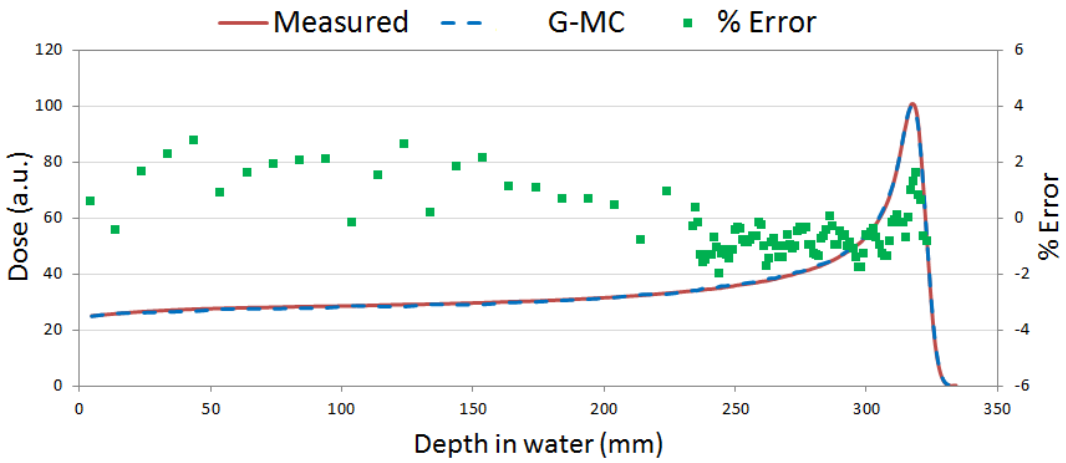

(ii)

Figure 30. (i) Performance evaluation of G-MC model against measurements. The simulated and measured IDDs were analyzed for mean point-to-point difference (red solid squares), range errors (green solid triangles), and dose-to-peak differences (blue solid diamonds). (ii) An example of IDDC for proton beam energy 226 MeV: simulated (blue dashed line), measured (solid red line), and local dose differences in percentage (green solid squares). The IDDs were normalized to area-under-the-curve.

3.3.2. Comparisons in Homogenous media

The depth dose comparison for SOBP1-3 between measurement and RS-MS/RS-PBA/G-MC is shown in figure 31. A spread of +/-3% from the measured is shown with the dotted lines. All the points for RS-PBA, RS-MC and G-MC are within 3% of the measured except at the distal edge. The accuracy of distal edge was measured by R80 values and was within 1 mm for all cases (Table 7). Table 8 shows the gamma results of measured versus RS-MC/RS-PBA/G-MC lateral dose profiles for all three

SOBPs at four different depths. The average gamma index value of RS-MC, RS-PBA, and G-MC versus MatrixxPT measurement averaged over all the measured planes was 97.2, 97.3, and 98.9% respectively.

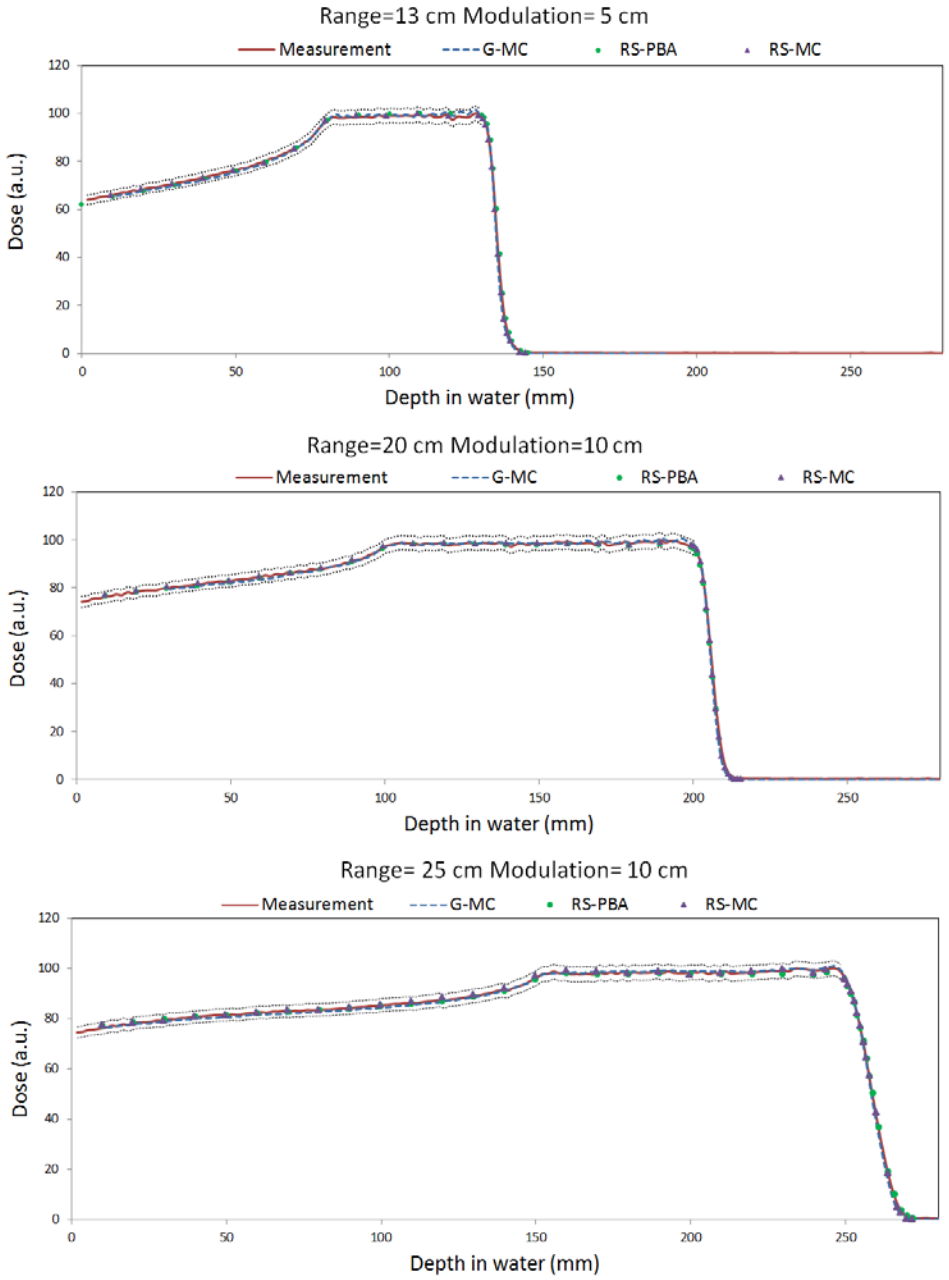

Figure 31. Comparison of percentage depth doses between measurement (solid red), G-MC (dotted blue), RS-PBA (solid green circles), and RS-MC (solid purple triangles). Top: SOBP1, Range 13 cm, Modulation 5 cm. Middle: SOBP2, Range 20 cm, Modulation 10 cm. Bottom: SOBP3, Range 25 cm, Modulation 10 cm. Also shown are error bars corresponding to +/-3% of measurement (dotted black lines).

Table 7. Difference in R80 range from measurement for G-MC, RS-MC and RS-PBA for SOBPs1-3. Results are given in mm.

	R80 (G-MC - Mea)	R80 (RS-MC - Mea)	R80 (RS-PBA - Mea)
Range= 13 cm, Modulation = 5 cm	-0.16	0.70	0.70
Range= 20 cm, Modulation = 10 cm	-0.30	0.60	0.50
Range= 25 cm, Modulation = 10 cm	-0.35	0.40	0.10

Table 8. Gamma index analysis results for SOBPs1-3 against measurement at four different depths using tolerances: DT= 3%, and DTA= 3mm.

	Range = 13 cm, Mod =5 cm				Range = 20 cm, Mod =10 cm				Range = 25 cm, Mod =10 cm		
Depth (cm)	Mea. vs G-MC	Mea. vs RS-MC	Mea. vs RS-PBA	Depth (cm)	Mea. vs G-MC	Mea. vs RS-MC	Mea. vs RS-PBA	Depth (cm)	Mea. vs G-MC	Mea. vs RS-MC	Mea. vs RS-PBA
5	98.0	99.5	98.5	5	98.2	97.9	97.5	5	96.50	93.50	96.20
12.5	99.3	99.4	98.7	9	99.4	100.0	96.3	17.5	99.10	99.10	96.40
15	99.3	98.5	99.1	10.5	99.7	99.7	99.4	20	99.10	99.80	99.40
17.5	99.5	99.4	99.8	12	99.1	99.5	98.4	22.5	99.10	99.90	99.90
Average	99.0	99.2	99.0		99.1	99.3	97.9		98.5	98.1	98.0

The depth doses and corresponding percentage errors for SOBP2 with a range shifter are shown in figure 32. At 5 cm air gap, the maximum local dose error from measured was 2.3, 1.3 and 2.0% for RS-PBA, RS-MC and G-MC respectively. At an air gap of 31.5 cm, all the points for RS-MC and G-MC were within +/-3% of measurement. However, RS-PBA, over-estimated the dose by as much as 10% at shallow depths (<0.5 cm). The discrepancy between measured and calculated decreased with depth and reduced to less than 3% at a depth of 5cm.

Figure 33 shows the comparison of depth doses when SOBP2 is incident at 45 degree angle. For dose points measured in the flat SOBP area and proximal region of the SOBP, both RS-MC and G-MC had acceptable agreement with measurement with a maximum error of -1.4% and -2.3% respectively. For RS-PBA, up to 6.5% error was seen from measurement in the SOBP area and dose points on the proximal side of the SOBP. Greater discrepancy between RS-PBA and measurement were found in the

distal penumbra region. Distal penumbra (distance between points corresponding to 80% and 20% of maximum dose at the distal fall-off) comparisons between measurement and RS-PBA/RS-MC/G-MC were performed (Table 9). Both RS-MC and G-MC were able to predict distal penumbra within 2 mm of the measured. For RS-PBA, the distal penumbra increases as much as 5 mm.

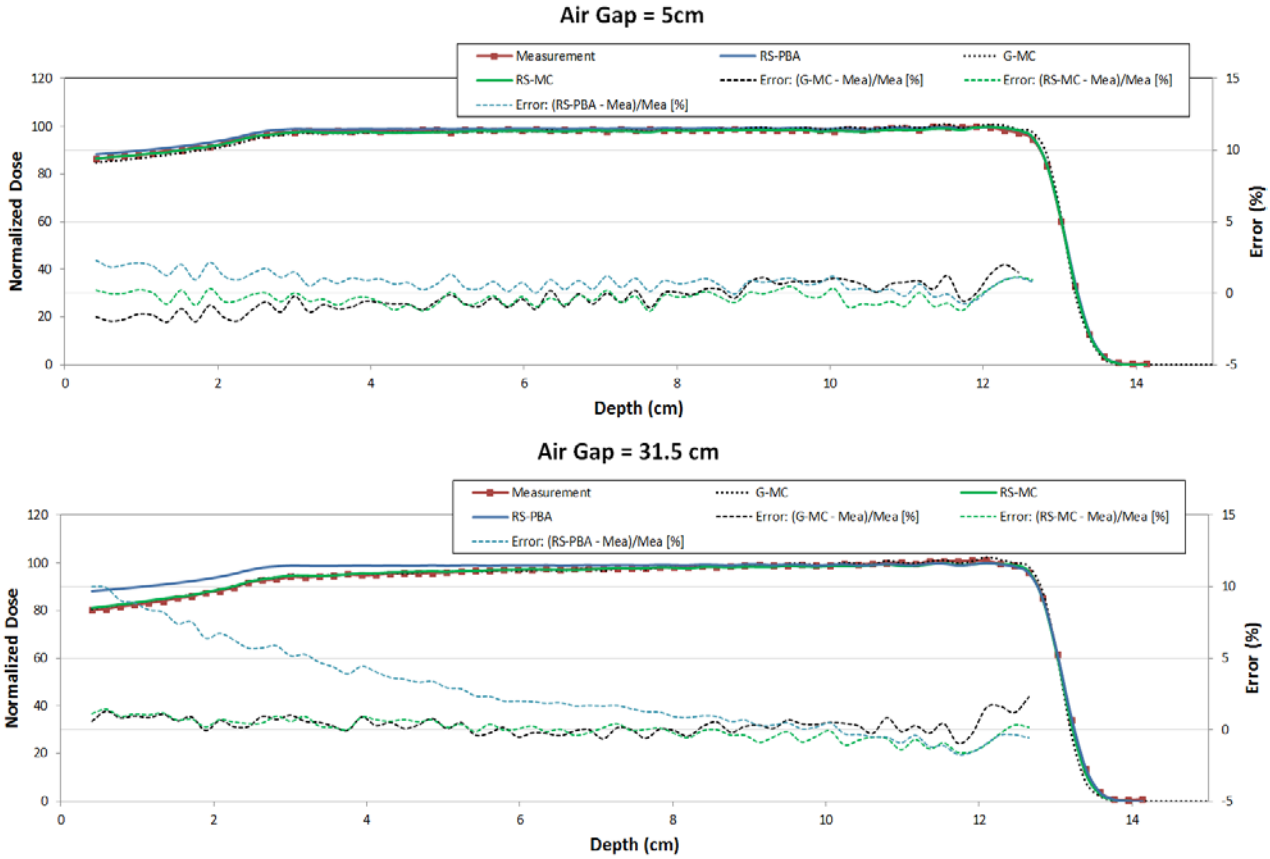

Figure 32. Evaluation of SOBP2 with range shifter of 7.5cm WET at two different air gaps, 5 cm (top) and 31.5 cm (bottom). Comparison is shown for measurement (red), G-MC (dotted black), RS-MC (solid green), and RS-PBA (solid blue). The local error between measurement and G-MC (dashed black), R-MC (dashed green), RS-PBA (dashed blue) is shown.

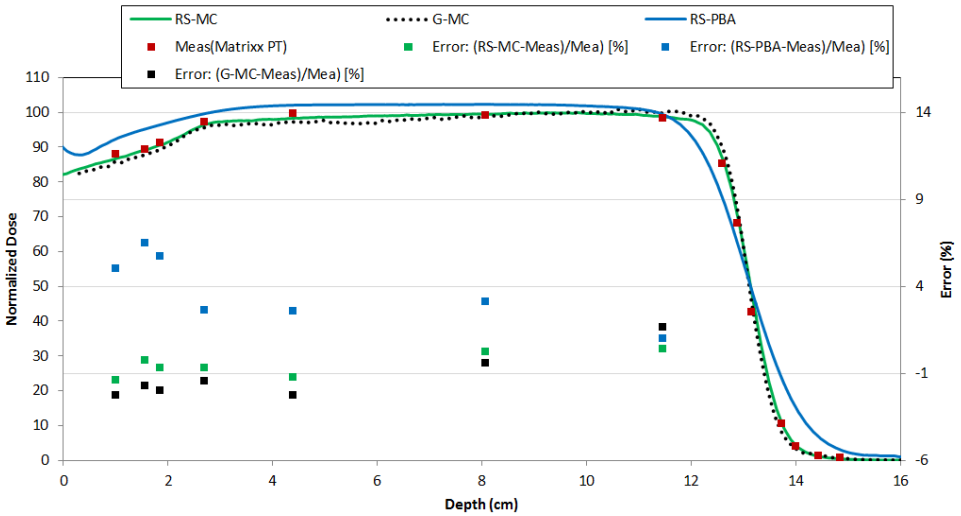

Figure 33. Depth dose comparison at the central axis for SOBP2 with a range shifter of 7.5 cm WET. The beam was incident at 45 degrees on water phantom. Measurements (solid red squares) were performed by a MatrixxPT device. The depth doses generated by RS-MC (solid green line), RS-PBA (solid blue line), and G-MC (dotted black) are shown. The local error between measurement and RS-MC (solid green square), RS-PBA (solid blue squares), G-MC (solid black squares) is shown.

Table 9. Error in distal fall-off for SOBP2 incident at 45 degrees on water phantom

	Distal Fall off (80% to 20%) (mm)	Error from Measurement (mm)
Meas	8.80	-
RS-PBA	13.90	5.10
RS-MC	8.00	-0.80
G-MC	7.10	-1.70

3.3.3. Comparisons in Heterogeneous media

Figure 34 shows the 2D dose profiles corresponding to the center of the phantom for a bone slab. The line dose profiles measured at the distal edge with the microDiamond detector are shown for both bone and lung slabs in figure 35. Both G-MC and RS-MC algorithms were able to predict accurate dose at the interface. RS-PBA algorithm showed broadening of dose fall-off effectively showing reduction in dose on

the bone (or lung slab) side and increase in dose on the opposite side of the slab. Using the DT=1% and DTA=1 mm criteria for 1-dimensional gamma index analysis between measured and calculated, the pass rates were 100% for G-MC for both lung and bone slabs. In case of R-MC, the pass rates were 100% and 94.4% for bone and lung targets respectively. The gamma index was <30% for lung and bone slabs for RS-PBA. Full results are given in Table 10.

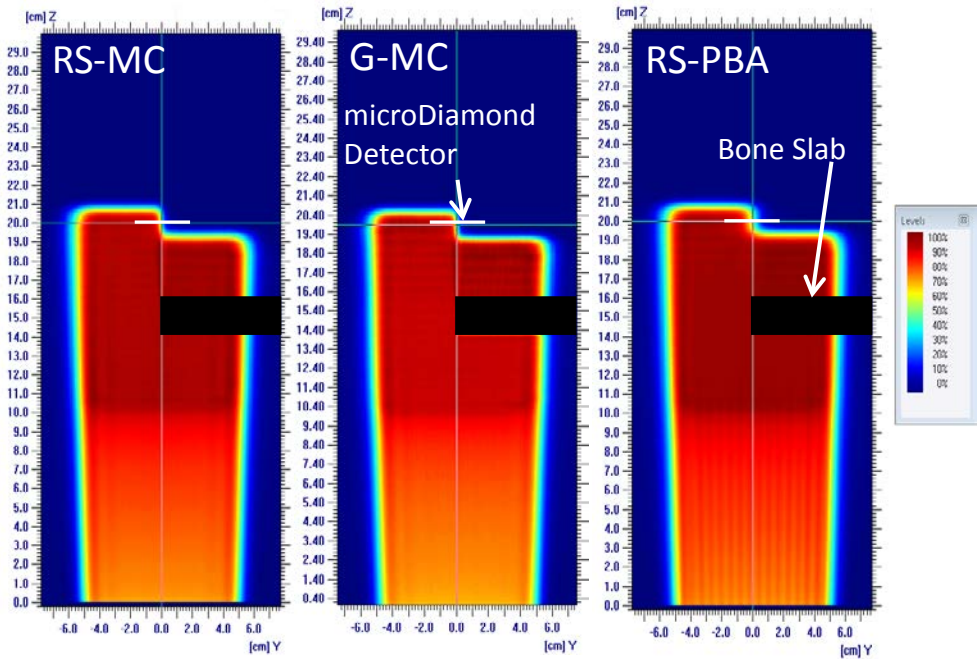

Figure 34. Two dimensional dose profiles obtained at the center of field obtained using RS-MC (left), G-MC (center), and RS-PBA (right) dose calculation algorithms. The bone slab was placed at 15 cm depth to align with the central axis. The microDiamond line dose measurements (as shown by solid white line) were performed at 20 cm for bone slab and 21.5 cm for lung slab.

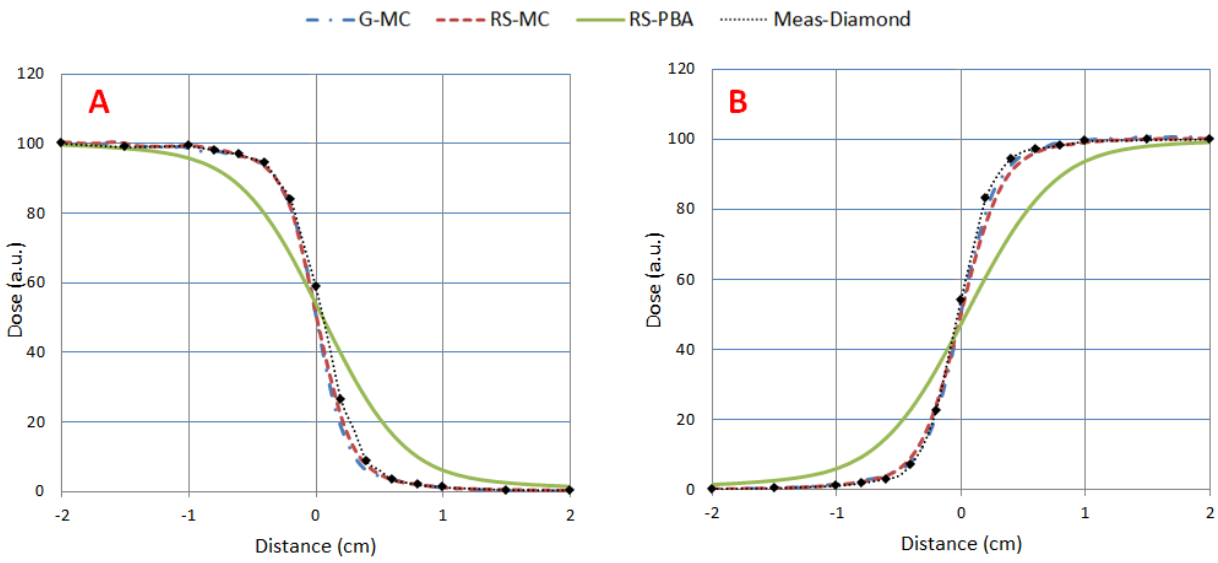

Figure 35. One dimensional dose profiles at the distal side of the inhomogeneity (see figure 27). The measurements (black dotted) were performed by a microDiamond detector. The calculated dose profile are G-MC (blue dash dot), RS-MC (red dash), and RS-PBA (green solid). Panel A: 2 cm bone slab at 15 cm depth, Panel B: 2 cm lung slab at 15 cm depth.

Table 10. Results of 1-D gamma index analysis comparing microDiamond measurement to G-MC or RS-MC or RS-PBA dose calculation algorithms using various DT and 1 mm DTA tolerance.

	Bone Slab			Lung Slab		
	1%/1mm	2%/1mm	3%/1mm	1%/1mm	2%/1mm	3%/1mm
G-MC vs Meas	100	100	100	100.0	100	100
RS-MC vs Meas	100	100	100	94.4	100	100
RS-PBA vs Meas	22	39	50	27.8	33.3	44.4

3.3.4. Comparisons in Anthropomorphic Phantoms

The qualitative results of the 2-D dose profiles acquired with Gafchromic film after every slice of the AR phantom along with RS-MC and RS-PBA measurements are shown in figure 36. There was good agreement between RS-MC and film measurement at all depths while RS-PBA could not reproduce features in the dose profile at depths closer to the distal edge. The –x and –y 1-D dose profiles at depth 15 cm were plotted

in the center of the target for measurement, RS-MC, and RS-PBA (figure 37). It can be seen that the RS-PBA algorithm maintained a high degree of dose uniformity in target and failed to account for dose perturbations resulting from lateral inhomogeneities such as interfaces formed by lung/heart/ breathing air ways and holes in the AR phantom.

The results of the gamma index analysis between measured and RS-MC/RS-PBA are shown in Table 11. The gamma index for RS-MC was greater than 90% (3%/3mm) at all depths except for the most distal plane which had a gamma index of 74.3%. For RS-PBA, 4 of 7 planes had gamma indexes less than 90% while the most distal layer had a gamma index of 45.7%. It should be noted that the most distal plane was outside of the high dose region (and also target) and positioned in the high dose gradient of the distal edge.

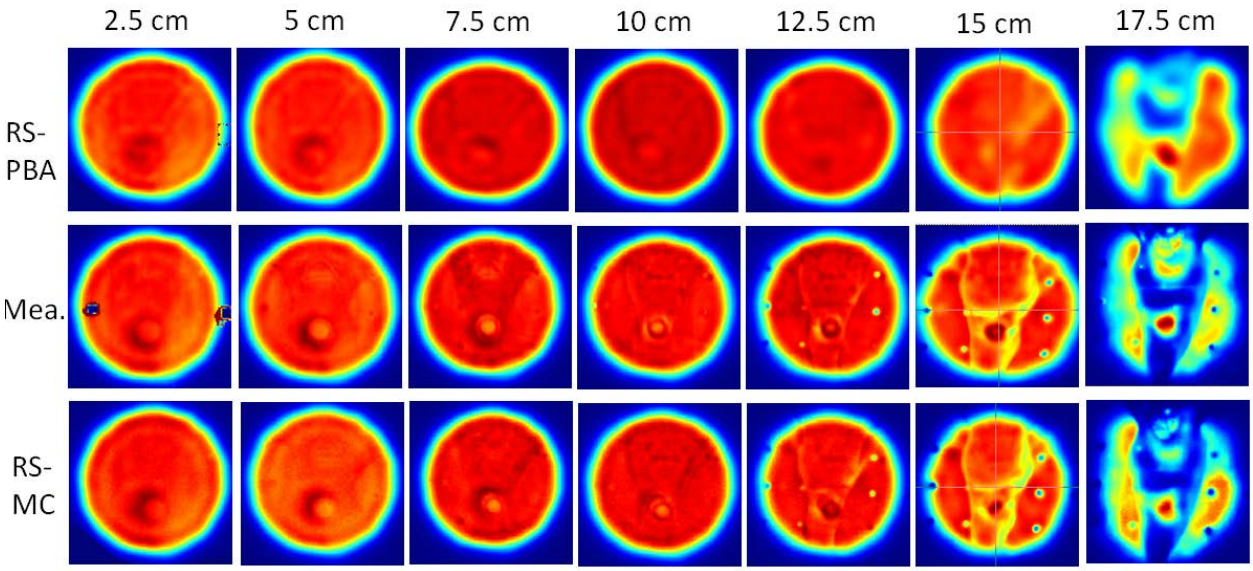

Figure 36. Dose planes obtained using RS-PBA (top), Gafchromic film (center), and RS-MC (bottom) after every slice of mediastinum section of AR phantom as shown in figure 28.

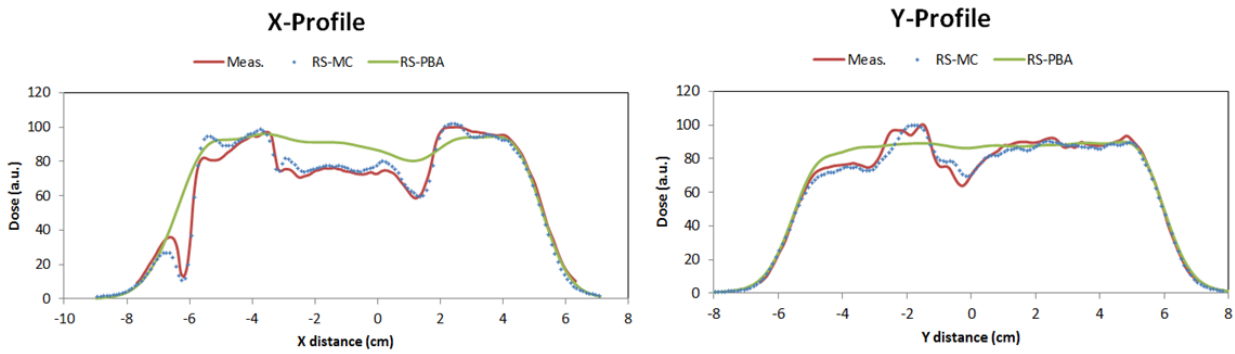

Figure 37. One dimensional dose profiles in –x and –y direction corresponding to depth 15 cm in mediastinum AR phantom. Shown are measurement (solid red), RS-MC (dotted blue), and RS-PBA (solid green).

Table 11. Results of 2-D gamma index analysis comparing RS-MC or RS-PBA dose calculations to measurements in an anthropomorphic mediastinum lung phantom.

	Depth (cm)	3%/3mm	5%/3mm	7%/3mm	7%/4mm
RSA-MC	2.5	96.5	98.8	99.5	99.8
RS-PBA		95.4	98.4	99.4	99.6
RSA-MC	5	93.8	97.5	99	99.5
RS-PBA		90.3	95.5	98.1	98.3
RSA-MC	7.5	93.7	97.6	99.3	99.6
RS-PBA		87.4	93.7	97.6	97.9
RSA-MC	10	96.4	99.3	99.8	100
RS-PBA		90.5	97.1	99	99.1
RSA-MC	12.5	97	98.9	99.3	99.7
RS-PBA		89.7	95.6	97.7	97.8
RSA-MC	15	93.9	96.5	97.7	99.1
RS-PBA		71.4	78.8	84.1	85.3
RSA-MC	17.5	74.3	79.5	83.5	88.3
RS-PBA		45.7	50.5	55.7	61.3

3.4. Discussions

Accurate dose calculations are an essential tool for optimal patient treatment in radiation therapy. Currently, pencil beam analytical algorithms that do not accurately account for inhomogeneities are the standard of care for treatment planning in proton therapy. The limitations of dose calculation algorithms may not be readily apparent in

routine clinical workflow as most of the patient-specific quality assurance measurements are made in the homogenous phantoms with normal incidence. This method does not check the performance of the dose calculation algorithms under clinical conditions where a proton beam traverses through a variety of tissues often at oblique incidence, resulting in very different scatter conditions. ICRU 24 (68) recommended that dose delivery accuracy to be +/-5% to a target volume if the objective of treatment is eradication of the primary tumor. Use of analytical algorithms for sites where a large amount of inhomogeneity is expected could result in dose inaccuracies in excess of 5% to parts of the target volume. The previous investigation by Grassberger (49) showed up to 5.6% overestimation at the center of a lung target when using the analytical dose calculation algorithm. Using MC, the dose difference was reduced to 1.6%. Similarly Schuemann (48) also showed up to 5% dose difference for complex geometries of H&N, and lung when using an analytical dose calculation algorithm. These studies concluded that the integration of MC into routine clinic use is vital for improvement of treatment quality for complex geometrical sites.

The newly introduced RS-MC algorithm provides a substantial improvement in proton therapy dose calculation. The RS-MC algorithm was tested against measurements and G-MC simulations in both homogenous and heterogeneous media. In homogenous media, both the RS-PBA and RS-MC algorithms accurately predict the doses when no range shifter device is used. However, when a range shifter is used, dose discrepancies of up to 8% are observed at shallow depths (< 1 cm) between measured and RS-PBA for an air gap of 31.5 cm. This discrepancy has been attributed to the lack of proper handling of secondary protons (nuclear halo) created in the range

shifter as they are transported over the air gap into the patient. In the RS-PBA algorithm, secondary protons created by non-elastic nuclear scattering are taken into account by a second Gaussian in the proton fluence function, as for example described by Suokup et al. (23). The size and relative weight of this secondary Gaussian is a function of initial beam energy and WET of the calculation point. This implies that the algorithm does not handle inhomogeneities along the beam path. Since the range shifter is treated as an extension of the patient in the RS-PBA algorithm, there can be a substantial inhomogeneity created by the air gap between the range shifter and the patient outline. The angular distribution of the secondary protons is rather wide, with the consequence that they will spread far away from the central beam axis as they move over the air gap. Since this effect is not considered by the ad hoc treatment of the nuclear halo, the dose in the entrance region will be overestimated by the RS-PBA algorithm. Secondary protons with higher energies will be more forward directed, and the error becomes smaller and smaller deeper into the patient. This is clinically significant for sites like breast where the target extends to the surface thus requiring a 7.5 cm WET range shifter for treatment planning. Due to the extent of the target volume, the largest snout (40 cm x 30 cm) is often required for treatment planning. This necessitates the air gap between patient and range shifter to be large (>10 cm) to avoid collisions. At our institution utilizing the RS-PBA algorithm, the measured doses are indeed often lower than the planning doses for such beam configurations, thus requiring additional intervention during treatment planning such as scaling up of monitor units. Utilizing RS-MC algorithm for such cases will provide accurate doses and also improve the workflow.

We also observed superior performance from the RS-MC algorithm in predicting doses when oblique beam angles are used in combination with a range shifter. For our test in a water phantom, with an oblique beam incident at 45 degrees, the RS-PBA algorithm showed broadening in distal-fall off. When an oblique beam with a range shifter is incident on the phantom, the dose discrepancy at shallow depths can be attributed to the limitation of the analytical algorithm to model range shifter and air gap as described in the paragraph above. The broadening of the distal edge can be attributed to the way that each spot is discretized into several algorithmic pencil-beam ray traces, so-called sub-spots. In RS6, this discretization into sub-spots is done at the entrance plane of the range shifter. As the sub-spots are transported through the range shifter and over the air gap, they may become significantly large at the patient surface and star to overlap each other. Since each sub-spot will see the patient as a sequence of semi-infinite layers, stacked perpendicular to the central axis, an inclined surface will not be correctly modeled by the sub-spots. The error will increase with the size of the sub-spots, and thereby with the magnitude of the air-gap. In RayStation 6 Service Pack 1 (RS6 SP1 released in April 2017), the discretization of the spots into sub-spots has been updated when a range shifter is used. Instead of performing the sub-spot discretization at the range shifter entrance plane, it is now done at the patient surface in the same manner as is done when no range shifter is present. The range shifter and air-gap is considered by first transporting the phase-space of the Gaussian spots without discretization (so-called single tracing), a handling that is motivated by the fact that a range shifter is a laterally homogenous device. To investigate the impact on the distal penumbra of this more efficient discretization, we have re-calculated the depth

dose of the inclined SOBP2 beam using PBA algorithm of RS6 SP1 (RS-PBA-SP1). The result is compared to the corresponding central axis doses of RS-PBA, RS-MC, and measurement in Figure 38, which clearly demonstrates that the new algorithm is a substantial improvement as compared to the previous one with respect to the distal fall off. The (80-20%) distal fall-off of the RS-PBA-SP1 dose curve is 10.0 mm, corresponding to an error relative the measured distal fall-off of 1.2 mm. This value should be compared to the RS-PBA distal fall-off error of 5.1 mm. In fact, this value is even better than the error of the G-MC (-1.7 mm), although RS-MC is still best at -0.8 mm (see Table 9).

Having accurate representation of distal penumbra is very important for optimal treatment planning. Quite often in proton therapy, there are critical structures near the distal edge where accurate dose estimation is paramount. Generally, sites like H&N, brain, and breast require oblique beams and the use of a range shifter, with spinal cord, brainstem, and lung structures that may located at or after distal edge. Using RS-PBA algorithm for such cases, the planner may compromise target coverage to meet the critical structure doses. Although RS-PBA-SP1 is an improvement in terms of distal-fall off for oblique beams employing a range shifter, it is still recommended to use RS-MC for such cases, since the problem with the surface dose is still unsolved.

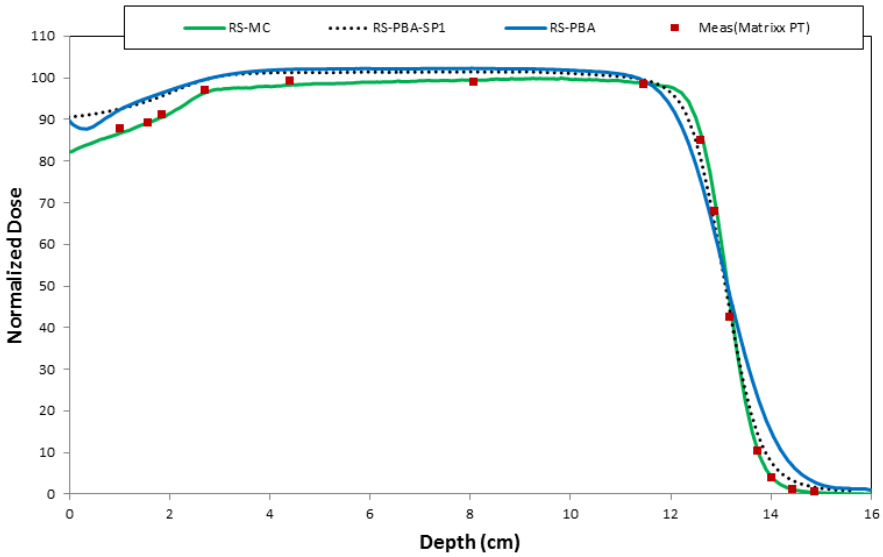

Figure 17. Demonstration of improved distal fall-off modeling in RS-PBA- SP1. SOBP2 at the central axis with a range shifter of 7.5 cm WET is plotted for RS-MC (solid green line), RS-PBA (solid blue line), measurement (red square), and RS-PBA-SP1 (dotted black). The beam was incident at 45 degrees on a water phantom.

RS-MC also outperformed RS-PBA in phantom with simple slab inhomogeneities. For both lung and bone slabs, RS-MC accurately predicted the dose profile due to inhomogeneity verified by measurements and G-MC simulations. RS-PBA showed local dose errors of as much as 50% for doses >20% of the maximum at the distal edge interface. The differences in doses by RS-PBA algorithm is again due to the infinite slab approximation. For protons at the bone (or lung) and water interface, a proton pencil beam that is traversing through bone may be partially in water and vice versa. When many neighboring pencil beams are considered together, this has an impact of broadening in the distal fall-off as seen in figure 35. For sites like H&N, brain, and lung, one could expect complex anatomic interfaces between sinus cavities, bone, and soft tissue resulting in inaccurate doses reported by RS-PBA. In an anthropomorphic phantom test, RS-MC algorithm was found to accurately predict the fine features of the isodose lines due to lateral inhomogeneities for all the measurement

planes. The RS-PBA algorithm often displayed highly uniform doses for planes towards the distal edge, without properly accounting for lateral variation in tissue density.

One of the concerns with MC-based dose calculation engines is the calculation speed. For a commercial dose calculation algorithm to be used for routine use, its performance should be similar to current analytical algorithms. We performed a simple comparison for a few relevant clinical cases to provide an estimate of the speed and performance. We calculated the doses for sites like breast, brain, H&N, lung, prostate (with pelvic nodes) with both RS-PBA and RS-MC calculation algorithms (table 12). The MC plans were calculated with 1% and 2% statistical uncertainty. The plans were previously optimized using the RS-PBA algorithm. Out of six scenarios evaluated, RS-MC was able to calculate doses faster than RS-PBA for three sites using 2% statistical uncertainty. For all six scenarios, calculation times for RS-PBA and RS-MC were within 20 seconds of each other. If 1% statistical calculation accuracy is desired, RS-MC was always slower and could take as much as 4 times the dose calculation time of RS-PBA e.g., for a brain case the time of calculation increased from 10 seconds for RS-PBA to 42 seconds for RS-MC. We found calculation speed of RS-MC algorithm to be adequate for routine clinical use at 2% statistical uncertainty.

Table 12. Comparison of calculation times for six different plans between RS-PBA and RS-MC. The plans were previously optimized using the RS-PBA algorithm.

Site	Plan Description	Isotropic Dose Calc Grid Size	Time (s): RS-PBA	Time (s): RS-MC (2%)	Time (s): RS-MC (1%)
Prostate with pelvic nodes	2 beams: Lt and Rt lateral	2 mm	28	20	80
Brain	Skull base target. 4 beams: PA, LAO, RAO and SAO	2 mm	10	17	42
H&N	3 beams: LPO, LAO and RAO	2 mm	70	50	172
Lung	2 beams: RPO and LPO	2 mm	43	30	92
Breast/ chestwall	Single oblique beam encompassing chestwall, super clav, axillary and IMC nodes	3 mm	7	16	41
CSI	3 PA beams: one each for brain, upper spine, and lower spine.	3 mm	17	21	77

The recent surge in number of proton centers worldwide is due in large part to advantages in proton physical depth dose characteristics that reduce the integral dose to healthy tissue for fixed tumor dose as compared to conventional x-ray therapy. A number of clinical trials (69-72) are underway comparing the long term survival and normal tissue toxicities between proton and photons. While the commercial dose calculation offerings in photons have improved considerably in last decade, not much progress has been made for proton dose calculations beyond mainstay analytical pencil beam algorithms. Our investigation has shown the need to implement MC dose calculations methods for proton spot scanning. Use of analytical algorithms may lead to findings that may show proton radiotherapy as unfavorable for certain disease sites as the magnitude of dose errors (~5 to 50%) is significant.

Several assumptions and limitations of our investigation should be noted. Although, we tested RS-MC for a variety of test cases, not every scenario can be simulated. The comparison between G-MC and RS-MC was performed for test cases in

water and simple slab heterogeneities. We did not evaluate any cases with implanted high density markers or surgical clips that are encountered so frequently in proton therapy. For dose measurements in oblique beam, a MatrixxPT device was utilized. The angular dependence of MatrixxPT has not been investigated in the literature. For G-MC beam model, an Ionization potential of 75 electron volts for water was used. The recent ICRU Report 90 (2016) has updated this value to 78 electron volts, which should change the range of proton beam in water. In our investigation, the maximum range error was 1 mm and average 0.3 mm. As our measured ranges matched well with simulated, the updated value of ionization potential should not impact the results reported in this manuscript. We believe that despite of these limitations, our investigation provides valuable information pertaining to validation of a commercial Monte Carlo dose calculation algorithm that will be beneficial to proton therapy community.

3.5. Conclusions

In this investigation, we performed a comprehensive evaluation of a newly available commercial Monte Carlo dose calculation algorithm, RS-MC, for use in proton spot scanning. The performance of RS-MC was tested against measurements and G-MC simulations in a variety of homogenous and heterogeneous phantom conditions. Both RS-PBA and RS-MC algorithms were found to be suitable for dose calculation in water phantoms with normal incidence of beam and small air gaps with range shifters. However the accuracy of RS-PBA was found to be clinically unacceptable when a range shifter is employed with oblique beams, large air gaps, and/or heterogeneous media. RS-MC provided superior performance for all these scenarios and should be

integrated into routine clinical use. Furthermore, the dose calculation speed of RS-MC algorithm is similar to RS-PBA at 2% statistical uncertainty.

CHAPTER 4 EVALUATION OF CERAMIC MARKER FOR THE TREATMENT OF OCULAR MELANOMA WITH PROTON THERAPY

4.1. Introduction

Although rare, ocular melanoma is the second most prevalent type of melanoma after skin and accounts for about 3.7% of all melanomas (73). It is the most common primary cancer of the eye in adults that arises in the iris, ciliary body or choroid. The current treatment options include surgical enucleation, trans pupillary thermotherapy, cryotherapy, proton therapy, brachytherapy, and stereotactic radiosurgery (74). The goals of the treatment are to prevent further growth of the tumor, preserve vision, and reduce the risk of metastases.

Proton therapy has been used for treatment of ocular melanoma since 1975 (75) with excellent control rates of 73% to 99% (76-80). Utilization of proton therapy for ocular melanoma offers a reduction of integral dose to preserve more healthy tissue around the target and mitigate risk of potential side effects. Due to the small size of ocular tumor volumes, a high degree of accuracy is required for imaging and positioning. Generally this is achieved through the use of implanted markers that are easily visualized through x-ray imaging. The markers are inserted in the vicinity of the target volume and are used for daily image-guided radiation therapy (IGRT). An ideal marker is the one that is readily visible on kV radiographs, produces minimal artifacts on the CT images, and causes no dose shadow in the underlying tissue (81). However, in order to provide good the visibility on kV radiographs, the markers have to be made either of high density material (high atomic number) or physically thick. Both of these have potential to cause substantial dose attenuation behind the marker. For proton therapy, the presence of the marker in the beam path not only causes changes to the

depth-dose but also changes to the proton beam range, resulting in under-dosing of target that lies distal to the marker. However, fiducial marker based alignment is very common in proton therapy for prostate (81-83), liver (84,85), and ocular treatments (86-89). Much effort from vendors has gone in developing markers that are as close to ideal marker as possible. Fiducial markers come in different configurations and some of the most common materials are gold, stainless steel, tantalum, and carbon coated with ceramic core (zirconium oxide). The most common shapes are wire-coil, rod, spherical, star-shaped, and dumbbell (90).

Tantalum markers (Mira Inc., Uxbridge MA) have been used extensively (89-91) for alignment of ocular melanomas for more than 25 years. These markers form a circular disc measuring 2.5 mm wide and 0.17 mm thick and are made of tantalum (atomic number 73, and density 16.4 g/cc). In addition to the extensive CT image artifacts, these markers have also shown to cause substantial dose shadows. Newhauser *et al* (89) performed Monte Carlo simulations and film measurements to conclude that dose attenuation is a function of orientation and depth of the marker in the proton beam. For the clinically relevant case, where the marker is aligned perpendicular to the beam, dose attenuation of up to 26% was seen. Ptaszkiewicz (91) performed two dimensional dose measurements using the thermoluminesecent dosimetric system and showed under-dosing behind the marker from 4 to 32%. Both investigations recommended comprehensive considerations in marker placement and treatment planning by the ophthalmologist, medical physicist and radiation oncologist. However, due to the requirement of 3-4 markers near ocular target volumes for

accurate image alignment, there is often a compromise in the selection of less dosimetrically ideal beam angles in order to avoid delivery through markers.

Recently, a new fiducial marker developed by Carbon Medical Technologies has been introduced in the market with potential usage for ocular target alignment. The marker is made of relatively low atomic number ceramic substrate (zirconium oxide-density 5.68 g/cc) and has promise to reduce the CT imaging artifact as well as the dose shadow while still maintaining the x-ray visibility. The objective of this study is to estimate the dosimetric impact and present a management strategy when the fiducial marker is placed in the field for ocular melanoma treatments. The performance of the marker for daily IGRT is also evaluated. The measurements and MC simulations were done based on the framework derived from a similar study done by Newhauser (89) for the tantalum marker. A comparison between tantalum and this new fiducial marker is also discussed.

4.2. Methods and Materials

4.2.1. Measurements

The BioMarc Secure^{TM} fiducial marker (Carbon Medical Technologies, St Paul, MN) is a newly available marker that is composed of a ceramic core (zirconium oxide) and pyrolytic carbon coating. According to the manufacturer, the carbon coating provides enhanced biocompatibility for the permanent placement of markers. The combination of core material and carbon coating makes the marker compatible for all forms of radiation therapy and imaging (CT, MRI and Portal). The marker dimensions as well as composition information were obtained from the manufacturer. The marker is a dumbbell shaped (Figure 39) with a length of 4.62 mm, width of 1.65 mm (at the

widest part), and thickness of 0.66 mm. The dumbbell shape makes the marker easier to visualize in x-ray images and prevents the migration of the marker in the tissue. It also allows the holes at the ends to be used for suturing purposes.

Figure 39. Enlarged view of BioMarc Secure fiducial marker.

The marker was placed inside an Alderson Rando head phantom (Radiology Support Devices, California, US) roughly near the orbit region. The head phantom was positioned at isocenter and kV x-ray images were taken in one of the treatment rooms at SCCA-PT center. Both the flat x-ray panel and x-ray tube are installed and maintained by the IBA (Ion Beam Applications, Louvain-Neuve, Belgium). The images were obtained using the pre-programmed head anterior-posterior (AP, peak kV= 85, mA= 400, and mS=320, SID= 200 cm) and head right-left lateral (LAT, peak kV= 85, mA= 320, and mS=250, SID = 200 cm) protocols in the Verisuite (MedCom GMBH, Darmstadt, Germany) imaging software. The images were qualitatively analyzed to see if the markers are clearly distinguishable from the normal anatomy. In addition to the planar x-ray images, computed tomography (CT) images were also obtained using the GE Optima CT580 scanner (GE Healthcare, Waukesha, WI). The protocol was typical

of adult ocular images (peak kV= 120, Slice thickness= 0.625 mm). Qualitative evaluation of CT images was performed to see presence or absence of any artifacts.

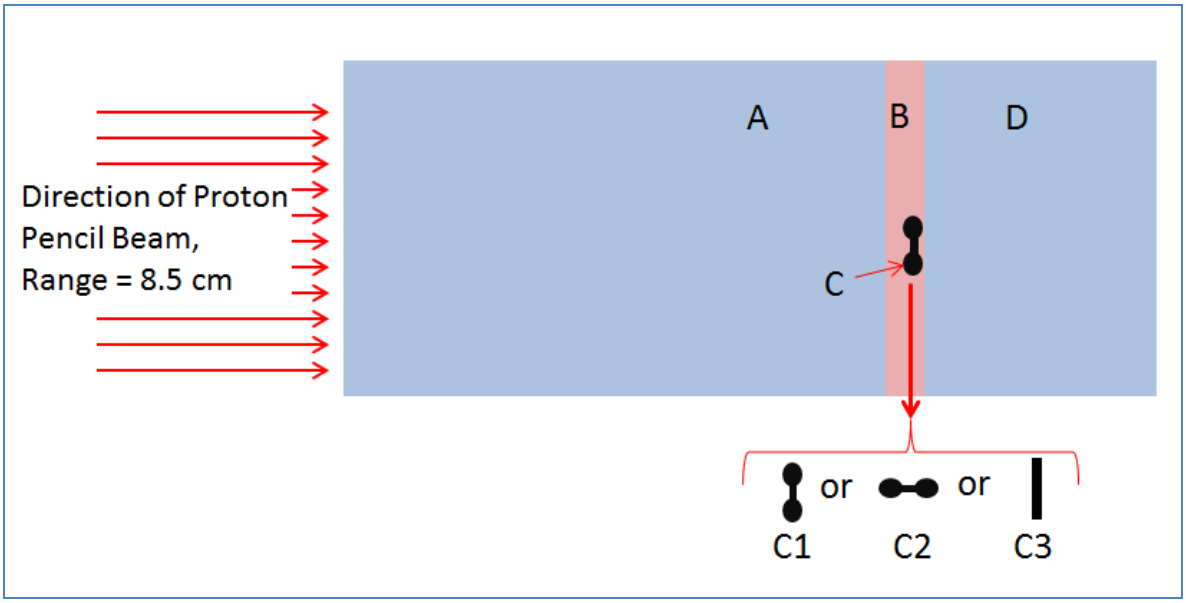

Figure 40. Experimental set up for marker dose shadow measurements. The marker (C) was embedded into a 0.5 cm thick Styrofoam slab (B) that was sandwiched in solid water phantom (A and D). The upstream solid water (A) was 7 cm thick. The marker was placed in three different orientations: perpendicular (C1), parallel (C2), and transverse (C3).

For dose shadow measurements, an in house phantom consisting of slabs of solid water and Styrofoam (density= 0.021 g/cc, Owens Corning Foam Insulation, Toledo, OH) was created (Figure 40). The marker was inserted into the Styrofoam slab in three cardinal orientations with respect to proton beam: (i) parallel, (ii) perpendicular, and (iii) transverse. Gafchromic EBT3 film (Ashland Inc., NJ) was placed at many depths after the marker to measure the dose shadow. In order to ensure the consistency of geometry, the films were always placed at the same depths for measurement with different orientations of the marker and un-perturbed measurement without marker.

The dose shadow measurements were carried out in a proton beam gantry at the SCCA-PT center. The beam line is an IBA PBS system with available energies of 98.5-226 MeV and corresponding ranges in water 7.5-32 cm. For shallow targets encountered for ocular lesions, a proton range of 2- 5 cm in water is required. In order to use our current pencil beam system for ocular treatments, a range shifter device (Shen *et al*., 2015) needs to be used. A range shifter is a material of uniform thickness that when placed in the proton beam has the impact of pulling the range back thus enabling the treatment of shallow depth targets. A single layer proton beam corresponding to range 8.5 cm and field size 3 x 3 cm^2 was used for measurements. A proton beam of 8.5 cm range with a 4 cm water equivalent thickness (WET) range shifter effectively provides a 4.5 cm range typical of what is used for ocular treatments. The single layer beam has spots placed in rectilinear fashion with 2.5 mm spot spacing thus resulting in total of 169 spots.

EBT3 film was exposed to approximately 28.5 Gy at the depth of maximum dose using the single layer beam. Four measurements corresponding to three marker orientations and one measurement without a marker were made. The films were scanned 48 hours after the exposure on a flatbed scanner (Epson Expression 11000XL, Epson America Inc., California, USA) using 300 pixels per inch of resolution and landscape orientation. The digitized films were analyzed using the commercially available DoseLab software (Mobius Medical Systems, TX, US). A control film that was similarly handled but not exposed was also scanned to obtain net optical density. Gafchromic film has been shown to be highly energy dependent (92-96) with increasing under-response as the point of measurement moves closer to the Bragg peak. This is

also called the quenching effect and needs to be taken into account for accurate dosimetry. Reinhardt *et al* (94), found under-response of as much as 20% for the lowest measured residual energy of 4 MeV corresponding to a 200 MeV incident proton beam. Fiorini *et al* (92), showed for proton energies encountered in eye treatments, under-response can be expected to reach as much as 50% in the low energy region (distal edge). Therefore, energy response correction is critical for using EBT3 films for proton therapy. We corrected for the energy response by making diamond detector (described below) and EBT3 film measurements in the unperturbed (without marker) beam. These measurements were made using the same single layer beam (range=8.5 cm) that is used for marker evaluation. The optical density from EBT3 films was correlated to the known doses measured by the diamond detector to derive correction factors as a function of depth in the proton beam.

The depth-dose was also measured without the marker using the commercially available microDiamond detector (Type 60019, PTW-Freiburg, Germany). Goma *et al* (67) have shown that the microDiamond detector's response is independent of the dose-rate and proton beam energy. Due to its small size and tissue equivalency, the microDiamond detector introduces a minimal amount of perturbation and is ideal for making proton depth-dose measurement (97). The microDiamond detector was mounted inside a homemade one dimensional water tank and connected to a PC electrometer (Sun Nuclear Corp., Melbourne, FL). Integrating charge measurements for the whole beam delivery were made at many points along the depth-dose with finer resolution in the high gradient region.

4.2.2. MC Simulations

MC simulations for the marker shadow were performed using the open source package Geant4 Application for Tomographic Emission (GATE) (40). GATE encapsulates the Geant4 libraries to provide a script based environment to run particle simulations. Grevillot *et al* (63) provided investigations of the different GEANT4 settings for proton particle therapy energy range. As recommended, the range cut (production threshold for secondary particles after EM interactions) and maximum allowable step size value (distance to next interaction) were set to 0.1 mm. The pre-calculated EM tables for mean free path, restricted stopping power, and range were set to 20 bins per decade to accurately describe the EM interactions. The physics models were implemented using the pre-defined physics builder mechanism and included binary cascade along with option 4 for electromagnetic interactions. The ionization potential for water, important for accurate range modeling, was set to 75 electron volts based on the recommendations of ICRU reports 37 (64) and 49 (8). The voxel size was set to 0.2 mm in -x, -y, and -z directions.

The first simulation was performed of the unperturbed single layer pristine Bragg peak in water for a range of 8.5 cm, and field size of 3 X 3 cm^2. The geometry was set up to be similar to the microDiamond depth-dose measurement. The dose was tallied in the x-z direction along the beam central axis. A beam model corresponding to the gantry delivery system at SCCA-PT was implemented based on the recommendation by Grevillot *et al* (62). The PBS beam model is entirely based on the measurements after the nozzle exit with source simulated at 40 cm upstream from the isocenter. Lateral spot profile measurements at 5 different planes along with integrated depth-

dose measurements at the isocenter plane were made to fit the GATE/GEANT4 model. The full validation of the model is presented in Chapter 3. For the purpose of this exercise, the agreement between pristine Bragg peak measurements versus simulation has been shown (Figure 42).

The second set of simulations was done to evaluate the shadow due to the marker in all three cardinal orientations. The simulation geometry was the same as the measurement geometry (Figure 40). For the simulation with the marker in the parallel orientation, a rotation of 8.5 degrees was applied to the marker to match the measurement geometry.

A final simulation was performed with beam conditions identical to realistic clinical plans. A typical clinical beam is range 3 cm and SOBP width 1.5 cm. In our PBS system, this beam can be created using the range 9 cm, SOBP width 1.5 cm in conjunction with a range shifter of 6 cm WET. For the purpose of this simulation, the air gap between the range shifter and water phantom was assumed to be zero, and Styrofoam slab was removed from geometry. The effect of marker depth as well as orientation with the SOBP region was evaluated.

All the simulations were performed on commercial a MacBook Pro (Apple Inc., Cupertino, CA) laptop computer with 2.2 GHz quad-core Intel Core i7 processor, 16 GB of 1600 MHz DDR3L onboard RAM running the OS X Yosemite version 10.10.4 operating system.

4.3. Results

The marker showed excellent visibility on the planar x-ray images for both AP and LAT views (Figure 41). These images suggest that these markers are suitable for

ocular target localizations. The CT images of the phantom showed the presence of black and white streaks that are typical of high atomic number materials (Figure 41).

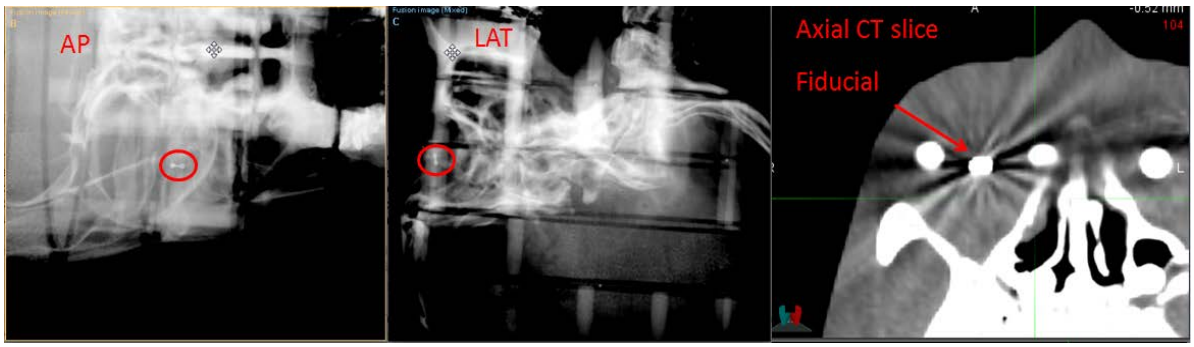

Figure 41. Planar x-ray images and an axial CT slice with BioMarc secure marker. The marker could easily be seen on the x-ray images. Streak artifacts due to marker were seen on the CT images.

The unperturbed depth-dose measured with the microDiamond detector and the MC generated curves are shown in Figure 42. The maximum difference was found to be 3.8% at 8.5 cm depth. The relative good agreement between MC and measurement confirmed that the gantry beam was accurately modeled in GATE/GEANT4.

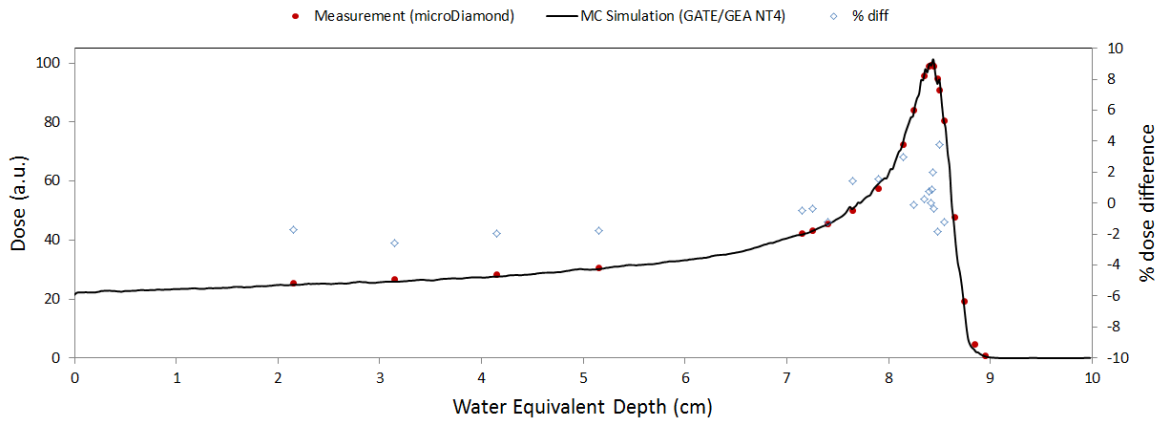

Figure 42. A single layer unperturbed (solid black line) beam with 8.5 cm range was simulated in GATE/GEANT4. The measurement (red filled circles) of the same beam was performed in water tank using the microDiamond detector. The point-by-point difference (blue open diamonds) between the simulated and measured depth-doses is shown on right axis.

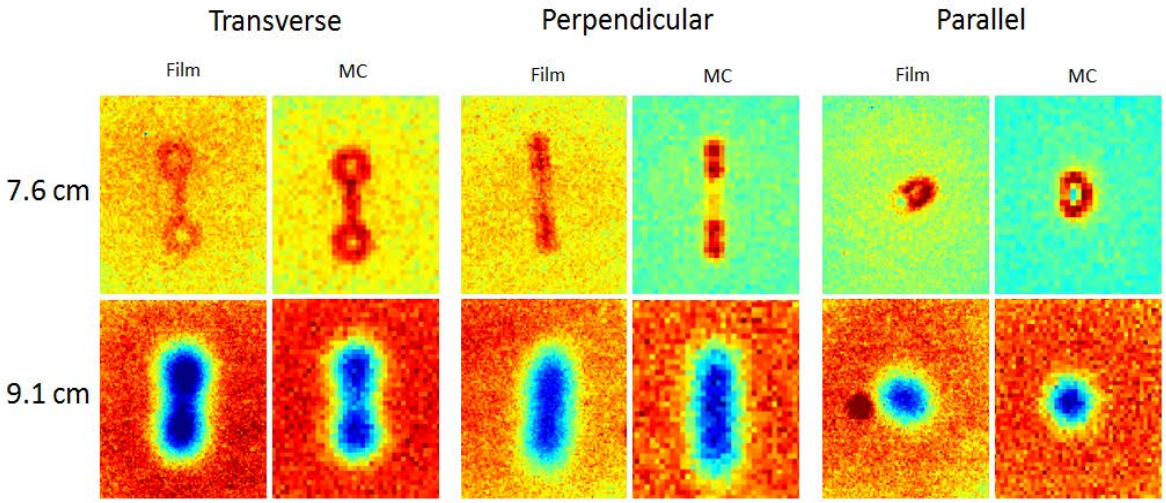

Figure 43.: Qualitative results of the dose shadows for three marker orientations. The marker is placed at 7 cm depth with dose shadows shown for 7.6 and 9.1 cm depths. All depths are given in water equivalent thicknesses. The images were enhanced for contrast for better visualization. The pixel size is 0.2 X 0.2 mm^2 for MC images, and 300 dots per inch for film images.

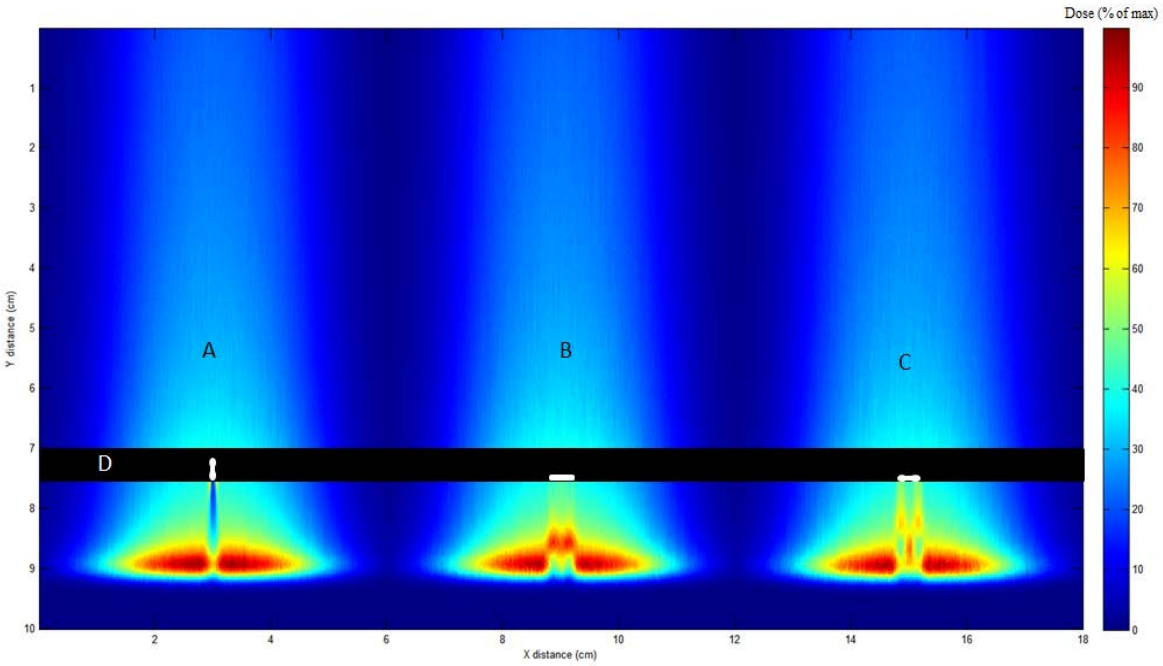

Figure 44. GATE/GEANT MC generated two dimensional depth-dose maps with marker oriented in perpendicular (A), transverse (B), and parallel (C) directions. The markers are placed inside the 0.5 cm Styrofoam (D) block placed at the 7 cm water equivalent depth.

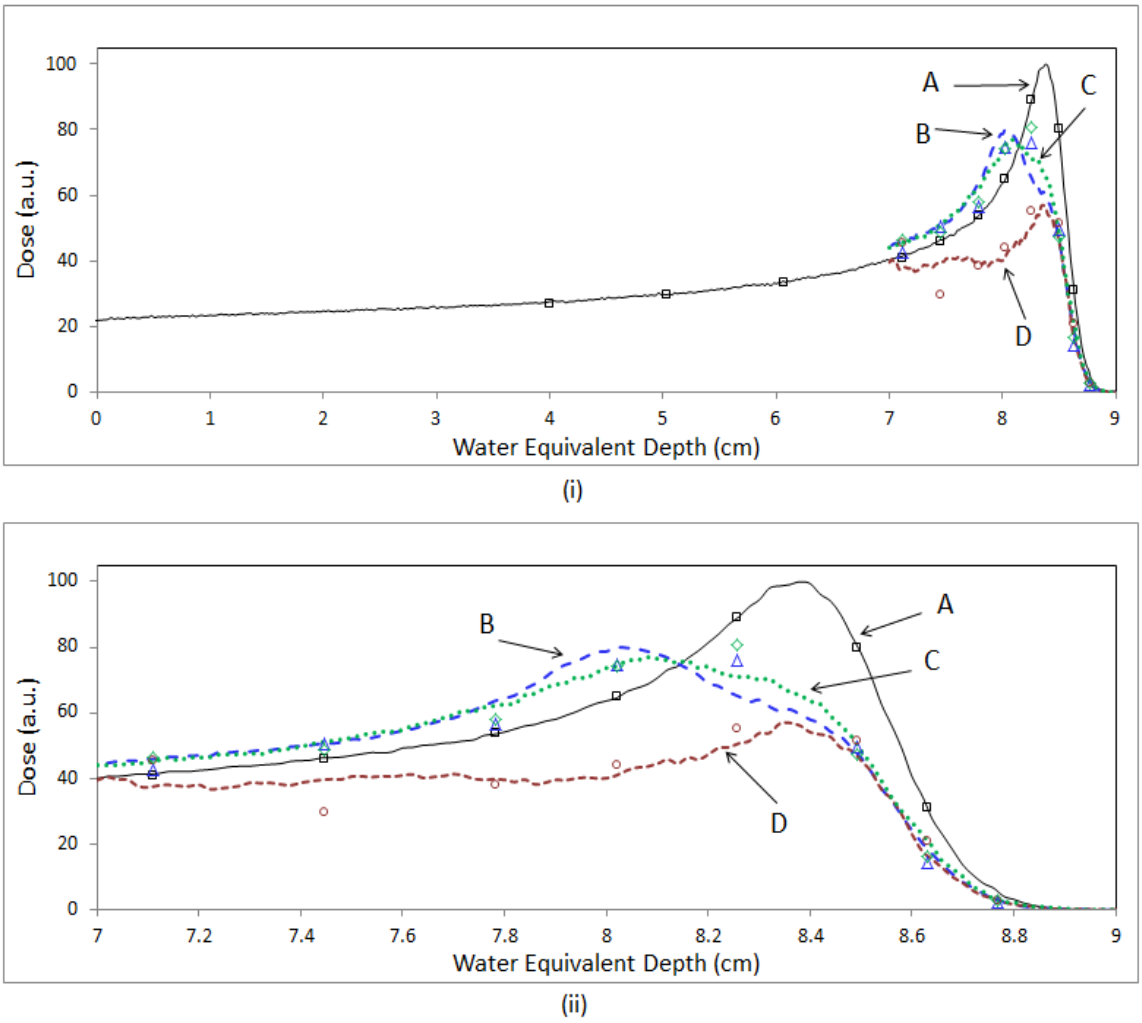

Figure 45. Comparison of MC simulated depth-dose distributions and EBT3 Gafchromic film measurements. MC simulations are shown for (A) unperturbed depth dose without any marker, (B) marker oriented in transverse direction, (C) marker oriented in perpendicular direction, and (D) marker oriented in parallel direction. Top Panel (i) shows depth dose in entirety. Bottom panel (ii) shows depth dose between 7 to 9 cm for better clarity. The measurement using the EBT3 Gafchromic film are shown for clip orientations: transverse (open triangles), perpendicular (open diamonds), and parallel (open circles). Also shown is the measurement of the unperturbed depth-dose using the EBT3 film (open squares).

The single layer marker shadow measurements using the EBT3 film and simulations using MC showed substantial dose shadows at the central axis of the marker. The qualitative characteristics of the dose shadows produced by the MC and EBT3 film at water equivalent depths of 7.6 and 9.1 cm are shown in Figure 43. Figure

44-45 shows the depth-dose characteristics for all three marker orientations. The dose shadows produced due to the markers were substantially worse for the parallel orientation compared to the other two orientations. In the high dose region from 8 to 8.3 cm, the dose attenuation of up to 29 to 38% was seen for the marker in the parallel orientation. Since the active length of the marker is ~4.6 mm, the approximate water equivalent thickness in worst case of parallel orientation is a product of active length and physical density (5.68 g/cc) ~26 mm. Therefore for the 8.5 cm range beam, the marker is able to block the primary protons completely when positioned at the 7 cm WET depth. For perpendicular and transverse orientations, there is enhancement of dose immediately after the marker, as the proton beam is pulled back due to the higher density of the marker. A dose enhancement of up to 18 to 23% was seen for transverse orientation within 4 mm past the marker. In the distal edge region from 8.5 to 8.8 cm, dose attenuation from -11 to -45% was found for all three configurations. In addition to the dose attenuation, proton beam penetration, measured by the distal 50% of the unperturbed beam, was also reduced by 1.1, 0.7, and 0.9 mm for parallel, perpendicular, and transverse orientations respectively. The agreement between the EBT3 film and MC is shown in Table 13. Differences of up to ~10% were noted. The differences were attributed to the small amount of misalignment in positioning of the marker in the beam path and up to ~4% differences that were seen between pristine peak measurement using microdiamond detector and MC simulation.

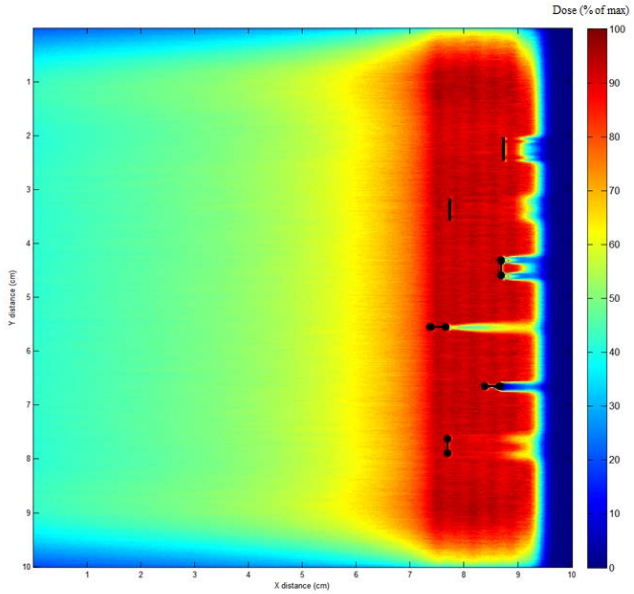

Figure 46. Monte-Carlo simulated dose shadows behind the marker for a typical clinical SOBP beam. Three orientations of the marker were simulated. Impact on dose shadow due to depth of marker within the SOBP was studied by placing marker at either proximal or distal side of the SOBP.

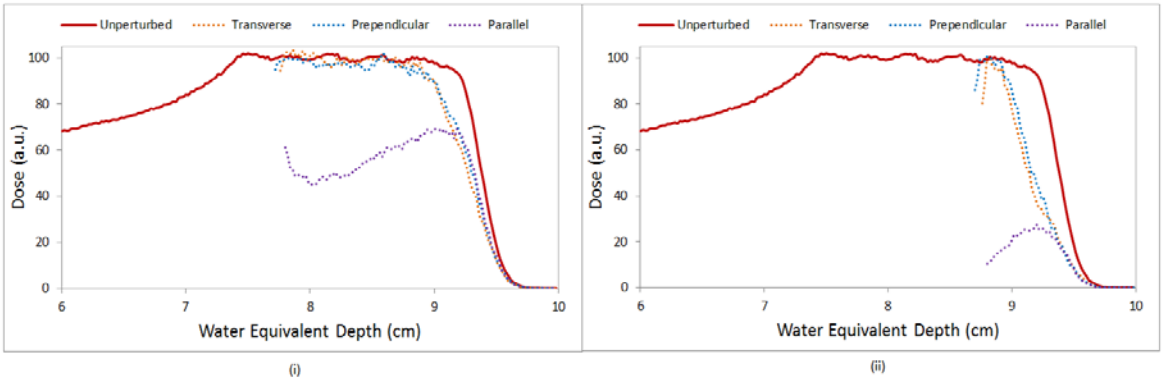

Figure 47. One dimensional depth-dose through the central axis of the marker corresponding to the 2-D dose map shown in figure 46 for the marker placed at the (i) proximal and (ii) distal side of the SOBP. Shown are depth-dose without marker i.e. unperturbed (solid red line), and marker in transverse (orange dotted line), perpendicular (blue dotted line), and parallel (purple dotted line) orientations.

Table 13. Depth dose differences between MC simulations and EBT3 film measurements. Results are shown for all three fiducial orientations.

	Transverse			Prependicular			Parallel		
WET	Film (%)	MC (%)	MC-Film (%)	Film (%)	MC (%)	MC-Film (%)	Film (%)	MC (%)	MC-Film (%)
7.1	42.9	46.0	3.1	46.2	45.0	-1.3	45.6	38.1	-7.5
7.4	50.5	50.4	-0.1	48.6	51.3	2.7	29.5	40.1	10.6
7.8	56.4	62.7	6.3	58.0	62.2	4.2	38.2	40.3	2.1
8.0	74.5	78.0	3.5	74.3	74.2	-0.1	44.2	41.5	-2.7
8.3	76.0	69.4	-6.6	80.9	71.0	-9.9	55.0	51.3	-3.7
8.5	49.6	51.5	1.9	47.4	49.8	2.3	51.6	46.0	-5.6
8.6	14.3	19.7	5.4	16.4	21.3	4.9	20.9	16.8	-4.1
8.8	2.2	3.0	0.8	2.6	2.9	0.3	2.7	1.6	-1.0
		Average	1.60		Average	0.63		Average	-0.66

Lastly, the results of the dose shadows due to the marker in the clinically relevant SOBP beam are shown (Figures 46 and 47). A total of six combinations were simulated: 3 cardinal orientations at two depths. The two depths corresponded to the possibility of marker placed in the SOBP after the proximal rise and just before the distal drop. As expected the dose shadows are larger when the marker is placed towards the distal part of the SOBP as the residual range of the proton beam is smaller. In addition, the dose shadows are worse for the parallel orientation as it presents the longest path for proton beam to travel inside the marker. However, the parallel orientation is also the least likely to occur clinically. In addition, parallel orientation also shields a smaller volume of tissue underneath the marker. The amount of dose attenuation for parallel orientation ranged from 23 to 56% when the marker is placed near proximal side of the SOBP. Here, the percentage attenuation is expressed with respect to unperturbed dose at the same location. For parallel orientation at distal part of the SOBP, the maximum dose attenuation was 89% immediately behind the marker. In this case, the low energy protons are completely stopping in the marker and the dose is entirely made up of scattered protons not interacting in the marker. For perpendicular and transverse orientations near the distal edge, the proton beam still has residual

range that is larger than the path length encountered in the marker. Therefore, the end result is that of pulling back the proton range that could result in the loss of coverage at the distal side of the target; the dose attenuation of up to 61% were seen towards the distal side of the SOBP for both cases. The D50% (depth of 50% dose level) ranges were pulled back by 2 and 2.4 mm for perpendicular and transverse orientations respectively. The size of dose shadows behind the marker was also found to be a function of orientation. Immediately behind the marker, the size of the dose shadow was as large as the effective area presented by the marker in the incident beam direction. While the amount of dose attenuation was largest for the marker oriented in parallel direction, the volume shielded was smallest. There is further reduction in volume shielded downstream as dose from scattered protons starts to build up.

4.4. Discussion

As the number of proton centers increases, more and more institutions will implement ocular therapy programs. One of the considerations for ocular therapy is the selection of a suitable marker for daily IGRT. Tantalum markers have been used for >25 years but introduce substantial streak artifacts on CT and large dose shadows (89). During our search for a suitable marker that could alleviate some of the issues of the tantalum marker, the carbon coated ceramic core BioMarc Secure was offered as an alternative by the manufacturer for ocular IGRT. In terms of size, the tantalum marker is a circular disc shaped that is 2.5 mm wide and only 0.17 mm thick. In contrast the Biomarc Secure is a dumbbell shaped and roughly 4.6 mm long and 0.66 mm thick. Therefore, the tantalum marker provides a markedly smaller footprint that may be easier for both ophthalmologist to suture and patients to tolerate. In terms of the

visibility on kV x-rays, operator was able to localize both markers on orthogonal images. Both markers produced streak artifacts in the CT images. Both markers produced significant dose attenuation in the underlying media. In the transverse orientation, the BioMarc Secure produced up to 40% dose shadows. Similarly, the parallel orientation of tantalum maker produced up to 26% dose reduction (89). One would theoretically expect reduced dose shadows from the BioMarc Secure marker due to low atomic number and density. However, the dosimetric benefits from lower density are offset by the increase in the thickness of the marker. If we assume that the most probable orientation for tantalum marker in the beam path is parallel and BioMarc Secure is transverse, the effective area as seen by the incident proton beam is roughly 3.8 and 4.9 mm^2 for tantalum and Biomarc markers respectively. Therefore, the new Biomarc marker shields a greater volume underneath the marker. Due to its bigger physical size, greater dose shadows and effective shielded volume, the BioMarc Secure marker does not present any improvements over tantalum marker.

In radiation therapy, ionization chambers are considered the gold standard for accurate dose measurements. However, using ionization chambers for measuring the dose shadow behind the marker is not feasible due to the small size of the marker and the resolution of the ion chamber. Film measurements provide greater resolution but suffer from linear energy dependent (LET) response (92, 95, 96) that introduces additional uncertainty. In our study, the measurement using the diamond detector was used to correct the film response, and agreement within ~10% was achieved between film and MC simulations. MC simulations provide a flexible platform to investigate the dose attenuation due to markers. MC methods enable users to simulate accurate

geometries and beam configurations that cannot be reproduced in the measurements. Furthermore, the doses can be calculated in sub-millimeter resolution, something that cannot be achieved in commercial treatment planning systems.

At SCCA-PT, ocular melanoma treatments are given most frequently in 5 fractions using 1-2 beams. By using multiple fractions, some averaging of the dose shadow should occur due to random errors introduced in the daily IGRT. This has the potential to reduce the severity of dose attenuation. Furthermore, having more beams should also alleviate the clinical impact of dose shadows. Based on our study, we do not recommend treating with a single beam and Biomarc marker in the beam path, as this scenario could result in severe under-dosing of a very small volume behind the marker. In the event that the marker must be present in the beam path, it is preferable for the marker to reside on the proximal side of the SOBP with added range to compensate for the pull back.

Several assumptions and limitations of our investigation should be noted. The marker is a zirconium oxide substrate with a 0.05 mm pyrolytic carbon coating. For our MC simulations, we ignored the coating and assumed the whole marker to be one material. In addition, all of the sharp edges have been removed by the process of chamfering. This was also ignored and not implemented for simulations. We believe these assumptions to be minor and do not expect any changes to our conclusions.

4.5. Conclusions

Evaluation of the recently available carbon coated BioMarc Secure^{TM} marker was reported for application to IGRT of ocular melanoma. The marker was readily visible on the planar kV x-rays. On CT scans, metal artifacts in the form of black and white

streaks were visible. The dose attenuation behind the marker was assessed using the MC methods and gafchromic dosimetry. As expected, the dose attenuation was found to be a function of marker orientation and position within the SOBP. For clinically relevant beams, dose attenuation of up to 89% was found for the worst case position of the marker within the beam. There is also a range pull-back effect for protons passing through the marker leading to severe under-dosing of the target at the distal end of the SOBP. It is recommended that all these factors be duly considered if BioMarc Secure marker is used for ocular treatments.

In addition, a comparison of BioMarc Secure with tantalum marker was presented. It was found that due to its larger physical size, greater dose shadows, and larger effective shielded volume, BioMarc Secure marker may be less attractive for ocular melanoma compared to widely used tantalum marker.

Chapter 5 Summary of Findings

Information provided by the TPS plays a pivotal role in radiation therapy by directly impacting patient care. Clinicians evaluate the dose distributions provided by the TPS to balance the risk of side effects against the treatment of a tumor. It is therefore imperative that a TPS provides accurate information to the planner. The quality of the output dose distributions generated by the TPS is dependent mainly on two factors: (i) quality of beam data obtained through measurements that is used an input for beam modeling, and (ii) inherent dose calculation accuracy of TPS. The commissioning of the TPS is a major undertaking that involves beam data measurement, beam modeling, and beam validation. Uncertainties and errors in any of the commissioning steps can lead to inaccuracies in the output dose distributions and have a potential to impact patient treatment outcomes. Generally, the input measurements are performed based on the recommendation by the TPS vendor. In addition, there are references in the form of AAPM or IAEA reports that can act as a resource for facilities to benchmark their TPS performance. However, unlike photon therapy, there are very limited literature and resources available for commissioning of proton therapy. To our knowledge, there are no AAPM reports with standards or tolerances that can be accessed to benchmark one's beam data and evaluate the overall accuracy of the planning systems.

The inherent accuracy of a TPS is dependent on whether the calculations are performed based on analytical methods or MC methods. Most of the current treatment planning is performed through pencil beam analytical methods in proton therapy. Until recently, there was no commercial MC dose calculation algorithm available that could

be used clinically. However, calculations using the MC have been performed for proton therapy for more than 20 years, albeit only for research purposes using one of the multi-purpose MC codes such as MCNPx and Geant4. However, these codes are not suitable for clinical use. With the recent introduction of commercial MC for dose proton spot scanning, one has the choice to calculate doses using either the analytical algorithm or MC. This brings up a couple of considerations: what kind of validation should be performed on MC before implementing it clinically, and what are the dosimetric differences in the performance of MC and analytical algorithms for clinically relevant conditions?

This dissertation presents solutions to many of the issues highlighted above. The first objective of this research was to provide a framework of commissioning an analytical planning system based on manufacturer's recommendations. The overall process of commissioning a planning system can be very daunting with limited time due to pressure of treating patients and non-familiarity with a new system. Chapter 2 provides the reader with details of the commissioning and validation of a commercial analytical dose algorithm for proton spot scanning delivery. In order to reduce the number of measurements, the beam data was measured for 18 proton energies. The depth doses were measured with the largest pancake detector available at that time, i.e. an 8 cm Bragg peak chamber. The spot profiles were measured with a 2-D scintillator detector at many planes and off-axis distances. Several limitations of the planning system were found such as inability to accurately determine doses for larger field sizes (>15 cm) and larger energies (>218 MeV). As a part of final validation, test cases from AAPM TG-119 were planned and delivered. The gamma index for all the

planes tested using the 3% dose and 3 mm DTA tolerance ranged from 92.8 to 100%. The results of our commissioning and validation can serve as a guide and benchmark for many upcoming proton centers.

The second goal of the study was to validate and benchmark a commercial MC dose calculation algorithm against measurements and simulations (chapter 3). A tertiary goal was to compare and contrast the performance of a pencil beam analytical algorithm against the MC algorithm. A beam model for the spot scanning gantry at the SCCA proton center was implemented in the GATE software package. The model was validated against measurements in a water phantom and was used for benchmarking the commercial MC algorithm. Validation was performed in a water phantom by measuring depth doses and profiles for three SOBP beams with normal incidence, a SOBP with oblique incidence, and a SOBP with a range shifter and large air gap. Further validation was performed against measurements and simulations in heterogeneous phantoms created by placing lung or bone slabs in a water phantom. Finally, MC and pencil beam analytical algorithms were compared to measured dose distributions in an Alderson-Rando phantom. As seen from the results, the MC algorithm showed highly accurate doses for most of the scenarios. In comparison, the pencil beam analytical algorithm was found to be insufficient when calculating doses with a large air gap, oblique beams, and anatomic sites with inhomogeneity. The pencil beam analytical algorithm showed up to a 10% difference in dose at the entrance for beams with range shifter and >30cm air gap while MC was always within 3% of the measurement. For an oblique beam incident at 45 degree, the analytical algorithm showed up to 6% local dose differences and broadening of the distal penumbra by 5

mm. In an anthropomorphic phantom, it was found that the pencil beam analytical algorithm showed uniform doses and failed to show the impact of lateral inhomogeneities and fine features such as sinus cavities, bone, and soft tissue interfaces. The Monte Carlo algorithm demonstrated improved dosimetric accuracy over the analytical algorithm in the presence of homogenous, heterogeneous and anthropomorphic phantoms. The computational performance of RS-MC was similar to RS-PBA algorithm. For complex disease sites like breast, head and neck, and lung cancer, the RS-MC algorithm will provide significantly more accurate treatment planning.

Finally, in Chapter 4, BioMarc Secure^{TM}, a fiducial marker with ceramic core (zirconium oxide) and carbon coating, was evaluated for use in the localization and alignment of ocular melanoma targets using proton pencil beam scanning. An anthropomorphic phantom with implanted fiducial marker was scanned to obtain kV x-ray and CT images. For dose shadow measurements, an in-house phantom was constructed using solid water, Styrofoam and EBT3 Gafchromic film. Dose attenuation behind the marker was measured at multiple depths and for three cardinal orientations: parallel, perpendicular, and transverse. MC simulations were set up to mimic the measurement geometry and dose attenuation behind the marker was studied for a single layer PBS beam. Qualitative analysis of the planar kV images showed excellent visibility of marker. Reconstruction artifacts in the form of light and dark streaks were present on the CT images. The film and MC simulations showed significant dose attenuation behind the marker that worsened when the marker was placed close to the distal edge. Dose shadows of up to 45% and range loss of up to 1.1 mm were seen

behind the marker. The transverse marker orientation in the clinical SOBP beam showed dose reduction of up to 61% and range pull-back of 2.4 mm. The dose attenuation was found to be a function of marker orientation and location within the SOBP. The analysis showed that small volumes behind the marker can receive severe under-dosing. This effect should be taken into account during the planning of treatment.

Proton Therapy, owing to its superior dose distributions, is emerging as a modality of choice for many radiation therapy treatments. It is anticipated that number of proton centers in the US and rest of the world will continue to grow at a fast pace for next few years. As new centers are opened, one of the most important considerations is the selection of a TPS. In this dissertation, we have provided methodology to commission a widely available TPS, RayStation, for proton spot scanning. The validation of both algorithms (pencil beam analytic and Monte Carlo) offered by RayStation is presented. We noted that pencil beam analytical algorithm has several shortcomings such as, inability to account for large air-gaps when range shifters are employed, inability to model oblique beams correctly, inability to account for heterogeneous anatomic features, and inability to correctly predict doses for large fields (>15cm) at greater depths (>20 cm). Our investigation concluded that RayStation's Monte Carlo algorithm is able to predict doses accurately for all these scenarios and is computationally efficient to be used on routine basis.

In this dissertation, a variety of phantom cases were used to demonstrate the improved accuracy of MC algorithm over analytical pencil beam algorithm. It is important to translate those improvements to actual patient cases and show the differences in dose distributions that are expected from using an improved dose

calculation algorithm. A number of abstracts (98-100) were recently submitted by our group to national and international meetings to highlight the importance of MC dose calculation in proton spot scanning. In a study by Fung *et al.* (98), retrospective analysis for three chest wall cases was performed comparing various dosimetric endpoints (Table 14). The plans were previously optimized using the pencil beam analytical algorithm to meet the target and critical structure dose constraints. The plans were then copied and re-calculated using the RayStation Monte Carlo dose algorithm. As can be seen in Table 14, for the three cases evaluated, there was a reduction in the PTV coverage (V95%: volume receiving 95% of prescription dose) by 11-29%. In addition, there was an increase in V20Gy and V5Gy (VxxGy= percentage of critical structure volume receiving xx Gy dose) for lung volumes. Overall, the MC re-calculated plans showed degradation in dose homogeneity as evident from increase in homogeneity index (HI).

Table 14. Comparison of various dosimetric endpoints for three chest wall cases calculated using the RayStation pencil beam analytic algorithm and RayStation Monte Carlo algorithm.

	Case #1		Case #2		Case #3	
	Pencil Beam	Monte Carlo	Pencil Beam	Monte Carlo	Pencil Beam	Monte Carlo
Air gap (cm)	10.0		14.9		17.9	
PTV V95%	98.8%	87.7%	99.7%	75.1%	98.4%	69.8%
Hotspot Gy (RBE)	52.5	59.2	52.1	59.7	52.8	63.2
Hotspot (%)	104.2%	117.5%	103.4%	118.5%	104.8%	125.3%
Homogeneity Index (D5%/D95%)	1.0	1.2	1.0	1.2	1.1	1.3
Lt Lung						
V20Gy	13.6%	16.9%	16.9%	20.4%	13.3%	19.5%
V5Gy	35.0%	47.30%	33.3%	41.3%	32.9%	43.35%
mean Gy (RBE)	7.1	9.1	7.9	9.4	6.8	9.3
Heart						
V5Gy	11.2%	10.2%	6.8%	6.7%	7.3%	5.0%
mean Gy (RBE)	2.5	2.3	1.6	1.5	1.3	1.0

In an another study by Maes *et al.* (100), a total of 10 lung cancer plans were retrospectively analyzed using the RayStation MC dose calculation algorithm. Evaluation of the V95 and HI of the CTV as well as V20Gy and VRX (Volume receiving prescription dose) for lung volume was performed. As shown in Table 15, there was a reduction in CTV coverage when plans were re-calculated using the RayStation MC dose calculation algorithm. There was also an increase in mean global hotspot from 106% for PBA to 109% for MC. Although the studies outlined here cover only two anatomic sites and have a limited number of cases, these results in conjunction with the phantom analysis provided in this dissertation highlight the need to incorporate MC dose planning for proton spot scanning.

Table 15. Comparison of various dosimetric endpoints for ten lung cancer cases calculated using the RayStation pencil beam analytic algorithm and RayStation Monte Carlo algorithm.

	Pencil Beam		Monte Carlo	
	Median	**Range**	**Median**	**Range**
CTV V95	100%	99% - 100%	90%	77% - 94%
CTV HI	0.98	0.95 - 1.00	0.91	0.87-0.94
Lung V20	25%	15% - 35%	25%	16% - 34%
Lung VRX	7%	2% - 11%	1%	0% - 6%
Max Dose	106%	101% - 113%	109%	104% - 122%

REFERENCES

1. Wilson RR. (1946). “Radiological use of fast protons”, Radiology, 47:487–491
2. Levy RP, et al. (1991). "Heavy-charged-particle radiosurgery of the pituitary gland: clinical results of 840 patients", Stereotact Funct Neurosurg 57(1-2): 22-35.
3. Graffman S, et al. (1985). "Proton radiotherapy with the Uppsala cyclotron. Experience and plans", Strahlentherapie 161(12): 764-770.
4. Tatter SB, et al. “Proton Beam Radiosurgery History”, https://neurosurgery.mgh.harvard.edu/ProtonBeam/hist-pb.htm
5. Slater, JD. (2007). "Development and operation of the Loma Linda University Medical Center proton facility", Technol Cancer Res Treat 6(4 Suppl): 67-72.
6. www.proton-therapy.org
7. https://www.ptcog.ch/index.php/facilities-in-operation
8. ICRU (International Commission on Radiation Units and Measurements). (1993). “Stopping Powers and Ranges for Protons and Alpha Particles”, ICRU Report 49 (Bethesda, MD: ICRU)
9. Koehler AM, Schneider RJ, Sisterspm JM. (1975). “Range modulators for proton and heavy ions”, Nuc. Instr. and Meth. 131 (3):437-440
10. Kooy HM, Trofimov A, Engelsman M. (2008). “Principals of systems and optimization”, edited by DeLaney T, Kooy HM. Proton and Charged Particle Radiotherapy. Lippincott Williams & Wilkins, Philadelphia, pp 73
11. Gottschalk B. (2008). “Treatment Delivery”, edited by DeLaney T, Kooy HM. Proton and Charged Particle Radiotherapy. Lippincott Williams & Wilkins, Philadelphia, pp 73

12. Koehler AM, Schneider RJ, Sisterspm JM. (1977). “Flattening of proton dose distributions for large –field radiotherapy”, Med. Phys. 4 (4):297-301
13. Charlie Ma CM. (2013). “Future Prospects of Particle Therapy”, edited by Charlie Ma CM, Lomax T. Proton and Carbon Ion Therapy, CRC Press, Florida, 2013, pp 213
14. Newhauser WD, Zhang R. (2015). "The physics of proton therapy", Phys Med Biol 60(8): R155-209.
15. Moliere G. (1947). “ Theorie der Streuung schneller geladenen Teilchen I Einzelstreuung am abgeschirmenten Coulomb –Fields”, Z Natureforschg: 2a;133-45
16. Gottschalk B. (2012). “Physics of Proton Interactions in Matter”, edited by Paganetti H. CRC Press, Florida, pp 49.
17. Berger MJ. (1993). “Penetration of proton beams through water I. Depth-dose distribution, spectra and LET distribution”, Report NISTIR 5226, National Institute of Standards and Technology. Gaithersburg, MD.
18. Bortfeld T. (1997). "An analytical approximation of the Bragg curve for therapeutic proton beams", Med Phys 24(12): 2024-2033.
19. Pedroni E, et al. (2005). "Experimental characterization and physical modelling of the dose distribution of scanned proton pencil beams", Phys Med Biol 50(3): 541-561.
20. Gottschalk B, et al. (2015). "On the nuclear halo of a proton pencil beam stopping in water", Phys Med Biol 60(14): 5627-5654.

21. Clasie B, Paganetti H, Kooy H. (2012). “Dose Calculation Algortihms”, edited by Paganetti H. CRC Press, Florida, pp 381.

22. Schaffner B, Pedroni E, Lomax A. (1999). “Dose calculation models for proton treatment planning using a dynamic beam delivery system: an attempt to include density heterogeneity effects in the analytical dose calculation”, Physics in Medicine and Biology. 44:27–41.

23. Soukup M, Fippel M, Alber M. (2005). “A pencil beam algorithm for intensity modulated proton therapy derived from Monte Carlo simulations”, Phys Med Biol. 50:5089–104

24. Hong L, Goitein M, Bucciolini M, Comiskey R, Gottschalk B, Rosenthal S, et al. (1996). “A pencil beam algorithm for proton dose calculations”, Phys Med Biol. 41:1305–30.

25. Smith, AR. (2009). “Present Status and Future Developments in Proton Therapy”, AIP Conf. Proc. 1153, 426

26. Gottschalk B, Pedroni E. (2008). “Treatment Delivery Systems in Proton and Charged Particle Radiotherapy”, edited by DeLaney TF and Kooy HM. Lippincott Williams & Wilkins, Philadelphia, pp. 33-49

27. Farr JB, Mascia AE, Hsi WC, et al. (2008). “Clinical characterization of a proton beam continuous uniform scanning system with dose layer stacking”, Med. Phys. 35, 4945–4954

28. Zheng Y, Ramirez E, Mascia A, et al. (2011). “Commissioning of output factors for uniform scanning proton beams”, Med. Phys. 38, 2299 –2306

29. Engelsman M, Lu HM, Herrup D, Bussiere M, Kooy HM. (2009). “Commissioning a passive-scattering proton therapy nozzle for accurate SOBP delivery”, Med. Phys. 36, 2172-2180

30. Pedroni E, Meer D, Bula C, Safai S, Zenklusen S. (2011). “Pencil beam characteristics of the next-generation proton scanning gantry of PSI: design issues and initial commissioning results”, Eur. Phys, 126:66

31. Kooy HM, Clasie BM, Lu HM, et al. (2010). “A case study in proton pencil-beam scanning delivery”, Int. J. Radiat. Oncol., Biol., Phys. 76, 624-630

32. Gillin MT, Sahoo N, Bues M, et al. (2010). “Commissioning of the discrete spot scanning proton beam delivery system at the University of Texas M. D. Anderson Cancer Center, Proton Therapy Center, Houston”, Med. Phys. 37, 154–163

33. Zhu XR, Poenisch F, Lii M, et al. (2013). “Commissioning dose computation models for spot scanning proton beams in water for a commercially available treatment planning system”, Med. Phys. 40, 041723 (1-15)

34. Cameron J, Schreuder N. (2012). “Smaller-Lighter-Cheaper: New Technological Concepts in Proton Therapy”, edited by Linz U. Ion Beam Therapy, Fundamentals, Technology, Clinical Applications. Springer, New York, pp. 673-685

35. Ezzell GA, Galvin JM, Low D, et al. (2003). “Guidance document on delivery, treatment planning, and clinical implementation of IMRT: report of the IMRT subcommittee of the AAPM Radiation Therapy Committee”, Med Phys. 30(8):2089–115. 10.

36. Ezzell GA, Burmeister JW, Dogan N, et al. (2009). “IMRT commissioning: multiple institution planning and dosimetry comparisons”, a report from AAPM task group 119. Med Phys. 36(11):5359–73

37. Li Y, Zhu RX, Sahoo N, Anand A, Zhang X. (2013). “Beyond Gaussians: a study of single spot modeling for scanning proton dose calculation”, Phys. Med. Biol. 57(4), 983-997

38. Lin L, Kang M, Solberg TD, Ainsley CG, McDonough JE. (2014). “Experimentally validated pencil beam scanning source model in TOPAS”, Phys Med Biol. 59(22):6859-73

39. Schwaab J, Brons S, Fieres J, Parodi K. (2011). “Experimental characterization of lateral profiles of scanned proton and carbon ion pencil beams for improved beam models in ion therapy treatment planning”, Phys. Med. Biol. 56, 7813-7827

40. Jan S, Santin G, Strul D, et al. (2004). “GATE a simulation toolkit for PET and SPECT”, Phys Med Biol. 49(19):4543-4561

41. Fracchiolla F, Lorentini S, Widesott L, et al. (2015). “Characterization and validation of a Monte Carlo code for independent dose calculation in proton therapy treatments with pencil beam scanning”, Phys Med Biol. 60(21):8601-8619

42. Russell KR, Isacsson U, Saxner M, et al. (2000). “Implementation of pencil kernel and depth penetration algorithms for treatment planning of proton beams”, Phys Med Biol. 45(1):9-27

43. Paganetti H. (2014). “Monte Carlo simulations will change the way we treat patients with proton beams today”, Br J Radiol. 87(1040):20140293

44. Fippel M, Soukup M. (2004). “A Monte Carlo dose calculation algorithm for proton therapy”, Med Phys. 31(8):2263-73.

45. Fiorini F, Hackett S, Van den Heuvel F. (2015). “Proton breast treatments: eclipse vs Monte Carlo Fluka dose comparison study”, Radiotherapy & Oncology. 115(1): S790

46. Bueno M, Paganetti H, Duch MA, Schuemann J. (2013). “An algorithm to assess the need for clinical Monte Carlo dose calculation for small proton therapy fields based on quantification of tissue heterogeneity”, Med Phys. 40(8):081704

47. Tourovsky A, Lomax AJ, Schneider U, Pedroni E. (2007). “Monte Carlo dose calculations for spot scanned proton therapy”, Phys Med Biol. 50(5):971-81.

48. Schuemann J, Giantsoudi D, Grassberger C, Moteabbed M, Min CH, Paganetti H. (2015). “Assessing the Clinical Impact of Approximations in Analytical Dose Calculations for Proton Therapy”, Int J Radiat Oncol Biol Phys. 92(5):1157-64

49. Grassberger C, Daartz J, Dowdell S, Ruggieri T, Sharp G, Paganetti H. (2014). “Quantification of proton dose calculation accuracy in the lung”, Int J Radiat Oncol Biol Phys. 89(2):424-30.

50. Paganetti H. (2012). “Range uncertainties in proton therapy and the role of Monte Carlo simulations”, Phys Med Biol. 57(11):R99-117.

51. Hotta K, Kohno R, Takada Y, et al. (2010). ”Improved dose-calculation accuracy in proton treatment planning using a simplified Monte Carlo method verified with three-dimensional measurements in an anthropomorphic phantom”, Phys Med Biol. 55(12):3545-56.

52. Yamashita T, Akagi T, Aso T, Kimura A, Sasaki T. (2012). “Effect of inhomogeneity in a patient's body on the accuracy of the pencil beam algorithm in comparison to Monte Carlo”, Phys Med Biol. 57(22):7673-88.

53. Agostinelli S, Allison J, Amako K, et al. (2003). “GEANT4-a simulation toolkit”, Nuclear Instruments and Methods. A(506):250-303

54. Allison J, Amako K, Apostolakis J, et al. (2016). ”Recent developments in GEANT4”, Nuclear Instruments and Methods. A835:186-225

55. Waters LS, Hendricks J, McKinney G. (2002). “MCNPX, Monte Carlo N-particle transport code system for multiparticle and high energy applications”, Los Alamos National Laboratory, Los Alamos (NM).

56. Fasso A, Ferrari A, Roesler S, et al. (2003). “The physics models of FLUKA: status and recent developments”, Computing in High Energy and Nuclear Physics. (paper MOMT005).

57. Sato T, Niita K, Matsuda N, et al. (2015). ”Overview of particle and heavy transport code system PHITS”, Annals of Nuclear Energy. 82:110-115

58. Perl J, Shin J, Schumann J, Faddegon B, Paganetti H. (2012). “TOPAS: An innovative proton Monte Carlo platform for research and clinical applications”, Med Phys. 39(11):6818-37.

59. Jabbari K, Seuntjens J. (2014). “A fast Monte Carlo code for proton transport in radiation therapy based on MCNPX”, J Med Phys. 39(3):156-63

60. Mairani A, Bohlen TT, Schiavi A, et al. (2013). “A Monte Carlo-based treatment planning tool for proton therapy”, Phys Med Biol. 58(8):2471-90

61. Saini J, Cao N, Bowen SR, et al. (2016). “Clinical Commissioning of a Pencil Beam Scanning Treatment Planning System for Proton Therapy”, International Journal of Particle Therapy. 3(1):51-60

62. Grevillot L, Bertrand D, Dessy F, Freud N, Sarrut D. (2011). “A Monte Carlo pencil beam scanning model for proton treatment plan simulation using GATE/GEANT4”, Phys Med Biol. 56(16):5203-19.

63. Grevillot L, Frisson T, Zahra N, et al. (2010). ”Optimization of GEANT4 settings for Proton Pencil Beam Scanning simulations using GATE”, Nuclear Instruments and Methods in Physics Research Section B: Beam Interactions with Materials and Atoms. 268(20):3295-3305

64. ICRU (International Commission on Radiation Units and Measurements). (1984). “Stopping Powers for Electrons and Positrons”, ICRU Report 37 (Bethesda, MD: ICRU)

65. Low DA, Harms WB, Mutic S, Purdy JA. (1998). “A technique for the quantitative evaluation of dose distributions”, Med Phys. 25(5):656-61.

66. RayStation Manual: RSL-D-RS-6.0-REF-EN-1.0-2016-12-22

67. Goma C, Marinelli M, Safai S, Verona-Rinati G, Wurfel J. (2016). “The role of a microDiamond detector in the dosimetry of proton pencil beams”, Med Phys. 26(1):88-94.

68. ICRU (International Commission on Radiation Units and Measurements. (1976). “Determination of Absorbed Dose in a Patient Irradiated by Beams of X or Gamma Rays in Radiotherapy Procedure”, ICRU Report 24 (Bethesda, MD: ICRU).

69. ClinicalTrials.gov. “Comparing Photon Therapy to Proton Therapy To Treat Patients With Lung Cancer” (NCT01993810)

70. ClinicalTrials.gov. “Pragmatic Randomized Trial of Proton vs. Photon Therapy for Patients With Non-Metastatic Breast Cancer: A Radiotherapy Comparative Effectiveness (RADCOMP) Consortium Trial” (NCT02603341)

71. ClinicalTrails.gov. “Randomized Trial of Intensity-Modulated Proton Therapy (IMPT) Versus Intensity-Modulated Photon Therapy (IMRT) for the Treatment of Oropharyngeal Cancer of the head and Neck” (NCT01893307)

72. ClinicalTrials.gov. “Intensity-Modulated Scanning Beam Proton Therapy (IMPT) With Simultaneous Integrated Boost (SIB)” (NCT01629498)

73. McLaughlin CC, Wu XC, Jemal A, Martin HJ, Roche LM, Chen VW. (2005). “Incidence of noncutaneous melanomas in the U.S.”, Cancer, 103: 1000-7

74. Lingam, G. (2015). “Options for management of intra ocular tumors”, Indian J Ophthalmol, 63, 204-10.

75. Gragoudas ES, Goitein M, Verhey l, Munzenreider J, Suit HD, Koehler A. (1980). “Proton beam irradiation. An alternative to enucleation for intraocular melanomas”, Ophthalmology, 87, 571-81.

76. Courdi A, at al. (1999). “Results of proton therapy of uveal melanomas treated in Nice”, Int J Radiat Oncol Biol Phys, 45, 5-11.

77. Desjardins L, et al. (1997). “Initial results of proton therapy in choroidal melanoma at the d'orsey center for proton therapy; The First 464 Cases”, Cancer Radiother, 1, 222-6.

78. Egger E, Schalenbourg A, Zografos L, Bercher L, Boehringer T, Chamot L, Goitein M. (2001). “Maximizing local tumor control and survival after proton beam radiotherapy of uveal melanoma”, Int J Radiat Oncol Biol Phys, 51, 138-47.

79. Gragoudas ES. (2006). “Proton beam irradiation of uveal melanomas: the first 30 years. the weisenfeld lecture”, Invest Ophthalmol Vis Sci, 47, 4666-73.

80. Singh AD, Turell ME, Topham AK. (2011). “Uveal melanoma: trends in incidence, treatment, and survival”, Ophthalmology, 118, 1881-5.

81. Huang JY, Newhauser WD, Zhu XR, Lee AK, Kudchadker RJ. (2011). “Investigation of dose perturbations and the radiographic visibility of potential fiducials for proton radiation therapy of the prostate”, Phys Med Biol, 56, 5287-302.

82. Giebeler A, Fontenot J, Balter P, Ciangaru G, Zhu R, Newhauser W. (2009). “Dose perturbations from implanted helical gold markers in proton therapy for prostate cancer”, J Appl Clin Med Phys, 10, 2875.

83. Lim YK, et al. (2009). “Microscopic gold particle-based fiducial markers for proton therapy of prostate cancer”, Int J Radiat Oncol Biol Phys, 74, 1609-16.

84. Kulkarni NM, Hong TS, Kambadakone A, Arellano RS. (2015). “CT-guided implantation of intrahepatic fiducial markers for proton beam therapy of liver lesions: assessment of success rate and complications”, AJR AM J Roentgenol, 204, W207-13.

85. Ohta K, Shimohira M, Sasaki S, Iwata H, Nishikawa H, Ogino H, Hara M, Hashizume T, Shibamoto Y. (2015). “Transarterial fiducial marker placement for image-guided proton therapy for malignant liver tumors”, Cardiovasc Intervent Radiol, 38, 1288-93.

86. Amstutz CA, Bechrakis NE, Foerster MH, Heufelder J, Kowal JH. (2012). “Intraoperative localization of tantalum markers for proton beam radiation of choroidal melanoma by an opto-electronic navigation system: a novel technique”, Int J Radiat Oncol Biol Phys, 82, 1361-6.

87. Damato B, Kacperek A, Errington D, Heimann H. (2013). “Proton beam radiotherapy of uveal melanoma”, Saudi J Ophthalmol, 27, 151-7.

88. Daftaria IK, Essert T, Phillips TL. (2009). “Application of flat panel digital imaging for improvement of ocular melanoma patient set-up in proton beam therapy”, Nuclear Instruments and Methods in Physics Research Section A: Accelerators, Spectrometers, Detectors And Associated Equipment, 598, 628-634.

89. Newhauser WD, Koch NC, Fontenot JD, Rosenthal SJ, S Gombos D, Fitzek MM, Mohan R. (2007). “Dosimetric impact of tantalum markers used in the treatment of uveal melanoma with proton beam therapy”, Phys Med Biol, 52, 3979-90.

90. Habermehl D, Henkner K, Ecker S, Jakel O, Debus J, Combs SE. (2013). “Evaluation of different fiducial markers for image-guided radiotherapy and particle therapy”, J Radiat Res, 54 Suppl 1, I61-8.

91. Ptaszkiewicz M. (2010). “Dose perturbation behind tantalum clips in ocular proton therapy”, Radiation Measurements, 45, 694-697.

92. Fiorini F, Kirby D, Thompson J, Green S, Parker DJ, Jones B, Hill MA. (2014). “Under-response correction for EBT3 films in the presence of proton spread out Bragg peaks”, Phys Med, 30, 454-61.

93. Gambarini G, Regazzoni V, Artuso E, Giove D, Mirandola A, Ciocca M. (2015). “Measurements of 2D distributions of absorbed dose in protontherapy with Gafchromic EBT3 films”, Appl Radiat Isot, 104, 192-6.

94. Reinhardt S, Hillbrand M, Wilkens JJ, Assmann W. (2012). “Comparison of gafchromic EBT2 and EBT3 films for clinical photon and proton beams”, Med Phys, 39, 5257-62.

95. Sorriaux J, Kacperek A, Rossomme S, Lee JA, Bertrand D, Vynckier S, Sterpin E. (2013). “Evaluation of Gafchromic(r) EBT3 films characteristics in therapy photon, electron and proton beams”, Phys Med, 29, 599-606.

96. Zhao L, Das IJ. (2010). “Gafchromic EBT Film dosimetry in proton beams”, Phys Med Biol, 55, N291-301.

97. Mandapaka AK, Ghebremedhin A, Patyal B, Marinelli M, Prestopino G, Verona C, Verona-rinati G. (2013). “Evaluation of the dosimetric properties of a synthetic single crystal diamond detector in high energy clinical proton beams”, Med Phys, 40**,** 121702.

98. Fung A, Saini J, Maes, D, Fang LC, Wong T. (2017). “Dose comparison between pencil beam and monte Carlo calculation algortihm in left chest wall patients”, Abstract presented at PTCOG 56, Japan.

99. Maes D, Bowen S, Fung A, Saini J, Bloch C, Eagen A, Zeng J, Rengan R, Wong T. (2017). “Dose comparison between proton pencil beam and Monte Carlo dose calculation algorithm for lung lesions”, Abstract presented at PTCOG 56, Japan.

100. Maes D, Bowen S, Fung A, Saini J, Bloch C, Eagen A, Zeng J, Rengan R, Wong T. (2017). “Dose comparison between proton pencil beam and Monte Carlo dose calculation algorithm for lung cancer patients”, Abstract accepted at ASTRO 2017.

ABSTRACT

COMMISSIONING AND VALIDATION OF ANALYTICAL AND MONTE CARLO BASED DOSE CALCULATION ALGORITHMS FOR PROTON SPOT SCANNING

by

JATINDER SAINI

December 2017

Co-Advisor: Dr. Charles Bloch

Co-Advisor: Dr. Jacob Burmeister

Major: Medical Physics

Degree: Doctor of Philosophy

Purpose: Accurate dose calculation is one of the necessary components of radiation therapy. While the commercially available photon dose calculation algorithm offerings have improved considerably in the last decade, proton dose calculations are still performed using analytical dose calculation algorithms. The goal of this work is to validate a newly available commercial Monte Carlo (MC) dose calculation algorithm using measurements and simulations in Geant4 Applications for Emission Tomography (GATE) software. A secondary goal is to compare and contrast the performance of the pencil beam analytical algorithm against the MC algorithm. Finally, GATE simulations are used to evaluate a newly available ceramic marker for ocular melanoma proton therapy.

Methods: Analytical and MC beam models of a full 360 degree gantry at the Seattle Cancer Care Alliance proton therapy center were commissioned in the RayStation treatment planning system. Measurements were performed using a variety of detectors

such as parallel plate ion chambers, 2D ion chamber arrays, a Bragg peak chamber, a 2D high resolution scintillation imager, and radiographic film. The analytical beam model was put through a series of tests that involved verification of point doses, PDDs, profiles, and doses in patient specific plans. The comparison of the analytical and RayStation MC (RS-MC) algorithms was carried out by measurements in homogenous, heterogeneous, and anthropomorphic phantoms. For comparisons against simulations, a beam model was developed in the GATE MC Toolkit using the measured beam data. For evaluation of the ceramic marker, a custom phantom with styrofoam insert with an embedded marker was created. Simulations and measurements were made for the marker in parallel, perpendicular and transverse orientations relative to the beam.

Results: For the analytical algorithm, evaluation of point doses in water showed dose differences>3% for proton ranges>30 cm, field sizes>15 x15 cm^2, and depths>25 cm. When a range shifter was employed, the analytical algorithm showed dose discrepancies of up to 10% in the entrance region for air gaps>30 cm. In oblique beam conditions, the analytical algorithm showed broadening in the distal penumbra by up to 5 mm. The RS-MC algorithm matched measurements and GATE simulations to within 3% at all points for SOBP depth doses, beams with a range shifter, and oblique incidence. The RS-MC also predicted accurate doses in an inhomogeneous phantom, where the simulations of the dose profile created at the interface matched measurements with 100% gamma index (GI) pass rate at 3% dose and 3 mm distance-to-agreement (DTA). In an anthropomorphic phantom, 6/7 planes had GI> 90% using 3% dose and 3 mm DTA for RS-MC. Corresponding numbers for the analytical algorithm showed only 3/7 planes with GI >90%. The ceramic marker showed

considerable dose attenuation behind the marker that worsened when the marker was placed close to the distal edge. The transverse marker orientation in the clinical SOBP beam showed dose reduction of up to 61% and range pull-back of 2.4 mm.

Conclusions: The RS-MC algorithm demonstrated improved dosimetric accuracy over the analytical algorithm in the homogenous, heterogeneous and anthropomorphic phantoms. The computational performance of RS-MC was similar to the RS-PBA algorithm. For complex disease sites like breast, head and neck, and lung cancer, the RS-MC algorithm will provide significantly more accurate treatment planning. The dose attenuation behind the ceramic marker was found to be a function of marker orientation and location within the SOBP. The analysis showed that small volumes behind the marker can receive severe under-dosing. This effect should be taken into account during the treatment planning.

AUTOBIOGRAPHICAL STATEMENT

JATINDER SAINI

EDUCATION

2014-2017	Ph.D.	Medical Physics	WSU, Detroit, MI
2010-2012	Residency	Medical Physics	CARTI, Little Rock, AR
2008-2010	M.S.	Radiological Physics	WSU, Detroit, MI
2003-2005	M.S.	Electrical Engg.	NMSU, Las Cruces, NM
1999-2003	B.Tech.	Electronics & Comm.	GNDU, India

CERTIFICATION

2013 Medical Physics American Board of Radiology

PROFESSIONAL ASSOCIATIONS

2008 - , Member, American Association of Physicists in Medicine

AWARDS & COMMITTEE APPOINTMENTS

2016 PT-COG Travel Fellowship
2009 WSU Graduate Professional Scholarship

PUBLICATIONS

1. Saini, J., Maes, D., Egan, A., Bowen SR., ……Bloch, C., (2017). Dosimetric Evaluation of a Commercial Proton Spot Scanning Monte Carlo Dose Algorithm: Comparisons against Measurements and Simulations. Physics in Medicine and Biology, In press.
2. Lee, E., Zeng, J., Miyaoka, R.S., Saini, J., Kinahan, P.E.,...Bowen, S.R. (2017). Functional lung avoidance and response-adaptive escalation (FLARE) RT: Multimodality plan dosimetry of a precision radiation oncology strategy. Med. Phys.
3. Saini, J., Bowen, S.R., St James, S., Wong, T., Bloch, C., (2017). Evaluation of ceramic marker for the treatment of ocular melanoma with proton therapy. Biomedical Physics & Engineering Express, 3 (2017) 027003.
4. Saini, J., Cao, N., Bowen, S.R., Herrera, M., Nicewonger, D., Wong, T., Bloch, C. (2016). Clinical Commissioning of a Pencil Beam Scanning Treatment Planning System for Proton Therapy. International Journal of Particle Therapy. 3(1), 51-60
5. Bowen, S.R., Saini, J., Chapman, T.R., Miyaoka, R.S,... Apisarnthanarax, S. (2015). Differential hepatic avoidance radiation therapy: Proof of concept in hepatocellular carcinoma patients. Radiother. Oncol., 115(2):203-10